Dielectric-loaded guiding of surface plasmon polaritons

Stær, Tobias Holmgaard

Publication date:
2009

Document Version
Publisher's PDF, also known as Version of record

Tobias Holmgaard

Dielectric-loaded guiding of surface plasmon polaritons

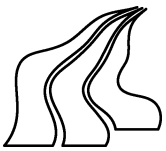

Department of Physics and Nanotechnology
Aalborg University, Denmark

Dielectric-loaded guiding of surface plasmon polaritons

Dielektrisk guidning af overflade plasmon polaritoner

Published and distributed by
Department of Physics and Nanotechnology, Aalborg University
Skjernvej 4A, DK–9220 Aalborg Øst.
Phone +45 99 40 92 15. Fax +45 99 40 92 35.

Typeset in LaTeX2$_\varepsilon$ by the author.

Printed in Denmark by Print Nord, Hjørring.

ISBN 978-87-89195-22-3

Abstract

This thesis concerns modeling, design, and characterization of dielectric-loaded surface plasmon-polariton waveguides (DLSPPWs) at telecommunication wavelengths. The work is aimed at establishing a new technology platform for integratable nanophotonic components by combining photonics and electronics on the same chip. The DLSPPWs consist of dielectric ridges with rectangular nano-meter-sized ($\sim 600 \times 500$ nm^2) cross-sections, deposited on smooth metal films. The surface plasmon polaritons (SPPs), being electromagnetic surface waves bound to, and propagating along, a metal-dielectric interface, are strongly confined to the ridges due to the large index contrast between the dielectric ridge region and the surrounding air. Theoretical studies of the DLSPPW structure performed with the effective index method (EIM) show that single mode propagation with sub-wavelength confinement, and propagation lengths on the order of ~ 50 μm at telecommunication wavelengths ($\lambda \sim 1500$ nm) can be achieved by proper design of the waveguide dimensions. Near-field optical imaging of fabricated DLSPPWs, performed with a scanning near-field optical microscope (SNOM), operating in collection mode, confirms that dielectric ridges of the designed dimensions do indeed support strongly confined modes with propagation lengths as predicted by the EIM calculations. In the near-field characterization, the DLSPPW modes are excited by focusing a laser beam from the opposite interface of the metal film using the Kretschmann-Raether configuration. It is found that by exciting surface plasmon polaritons in a dielectric funnel, extending the ridge waveguide, efficient excitation with low background noise can be achieved. The effects of bending and splitting the waveguides on losses are investigated with the SNOM, and the results show that when bending the waveguide with a radius of curvature $R \gtrsim 4$ μm, the radiation losses are almost un-noticeable, due to the strong mode confinement. In the case of the fabricated Y-splitters a 50/50 splitting of the mode is observed, however, a slight curvature right at the splitting region (due to the resolution of the mask used in the fabrication) causes undesired scattering losses, slightly deteriorating the overall transmission performance. 3D finite element simulations do, however, show that this can be remedied by increasing the resolution of the mask.

In addition to the near-field optical characterization of simple waveguiding components such as S-bends and Y-splitters, the performance of several different passive

wavelength selective components is investigated with the SNOM. Periodic modulation of the transmission is achieved by realizing waveguide-ring resonators (WRRs), where a ring resonator is placed in close proximity of a straight waveguide, which is excited at different wavelengths. The fabricated WRR, with the best tuned coupling to the ring, features an insertion loss of $\sim$ 2 dB, a narrow tunable bandwidth ($\sim$ 20 nm), and high contrast ($\sim$ 13 dB) features in the transmission spectrum. The performance of the components is found in good agreement with results obtained with the EIM. Wavelength filtering is also obtained by realizing Bragg gratings (BGs). 600-nm-period step-in-width (from 500 nm to 2 μm) BGs with 300-nm-long intervals between wide BG sections and containing different number of periods: N=10, 20, 30, and 50 are fabricated and characterized with a SNOM. The best performance is found for the 30-period BG, which exhibits well-defined Bragg reflection and extinction in transmission within the wavelength interval 1540 nm $-$ 1600 nm. Finally the coupling between two parallel DLSPPWs is investigated by fabricating and characterizing directional couplers (DCs), where the two waveguides are brought into close proximity of one another by means of S-bends. The influence of the distance between the waveguides and the wavelength on the coupling is established, and excellent agreement is found to EIM results. On the basis of EIM calculations, approaches for designing DCs capable of physically separating two signals of different wavelengths and for designing ultra-compact waveguide crossings with low cross-talk are introduced.

Preface

This thesis entitled "Dielectric-loaded guiding of surface plasmon polaritons" summarizes my work done at the Department of Physics and Nanotechnology at Aalborg University during my three years as a PhD student, which commenced in September 2006. The work has primarily consisted of modeling, design, and characterization of dielectric-loaded surface plasmon-polariton waveguides, and is part of a larger European research project denoted "Polymer-based nanoplasmonic components and devices" (PLASMOCOM) financed under the sixth framework programme for specific targeted research or innovation projects (IST 034754). The project is a collaboration between five European universities and a commercial partner which each have specified work packages and tasks to fulfill. The institutions and project coordinators are: Aalborg University, Denmark (Prof. S. I. Bozhevolnyi), Université de Bourgogne, France (Prof. A. Dereux), Queens University of Belfast, United Kingdom (Prof. A. V. Zayats), Laser Zentrum Hannover, Germany (Prof. B. N. Chichkov), ICFO Barcelona, Spain (Prof. R. Quidant), and Silios Technologies, France (Dr. T. Berthou).

This thesis is based on already published articles which are stated in the list of publications and enclosed as appendixes. In order to set the work in context to other related research areas, an introduction to SPPs in general and SPP waveguides in particular, are given in the first chapter. In the second chapter the effective index method, which has been used extensively throughout the work for modeling and design, is introduced. At the end of this chapter the main results achieved with the EIM are summarized, and references to the relevant publications are given. In the third chapter scanning near-field microscopy is introduced as a method for characterizing the fabricated waveguide samples. This chapter is concluded with a summary of the main results and references to the relevant publications. In the final chapter of the thesis I present my conclusions and offer an outlook of the DLSPPW technology.

Acknowledgments

There are several people that I would like to acknowledge, without whom I would not have succeeded in preparing this work. Firstly I would like to thank my supervisor Sergey I. Bozhevolnyi, whose enthusiasm and drive for progress has been a great motivation during my work. Ilya P. Radko, Valentyn S. Volkov, and Jonas Beermann for welcoming me in the research group, and for being very helpful when working in the laboratory as they all have great experience with near-field microscopy and are eager to share their knowledge. Especially during my first months of experiments, I benefitted a lot from their experience and knowhow. Jens Rafaelsen has always been very helpful when encountering problems in the laboratories, and I am very grateful for his guidance in the performance of scanning electron microscope images of the DLSPPW samples. I would also like to thank Thomas Søndergaard for developing the multilayer waveguide program used in the EIM calculations performed within this work.

I have also benefitted a lot from a very good collaboration inside the PLASMOCOM network here in Aalborg and in between the other institutions involved. Particularly Herman Högström and Zhuo Chen who had Post. Doc. positions at Aalborg University with whom I have collaborated in the laboratory. Among the PLASMOCOM collaborators I would particularly like to thank Laurent Markey who has fabricated the excellent samples, which are the basis of all the experimental work presented in this thesis. Alexey V. Krasavin, who has done 3D finite element modeling of the DLSPPW structures, and Pádraig Bolger, who is doing near-field microscopy in Belfast, for a very good collaboration and for some good laughs at the PLASMOCOM meetings.

I would furthermore like to thank my colleagues at the department, in particular Jesper Jung, Jakob Bork, and Thomas B. Lynge for their friendship and for some good talks during lunch- and coffee breaks. It has been great to discuss professional and general issues in an informal environment. From the department, I would also like to thank the secretaries Ulla Ponsaing and Jette L. Christensen and the technical staff Hans Nielsson and Kim H. Jensen for always being friendly and helpful.

I would also like to thank my friends outside the department for being there when I needed to have fun and relax. This has given me some important breaks from the work, where I could unconsciously reflect on problems and return prepared and motivated.

Last but not least, I would like to thank my wife and family for their genuine interest in my work and for their patience and support in stressful times. You have been a great support and motivation.

Aalborg, Denmark, July 2009 **Tobias Holmgaard**

Contents

Appendix

List of used acronyms

AFM:	Atomic force microscope
ATR:	Attenuated total reflection
BG:	Bragg grating
CPP:	Channel plasmon polariton
DC:	Directional coupler
DLSPP:	Dielectric-loaded surface plasmon polariton
DLSPPW:	Dielectric-loaded surface plasmon-polariton waveguide
EIM:	Effective index method
FEM:	Finite element method
FWHM:	Full width at half maximum
MZI:	Mach-Zehnder interferometer
PLASMOCOM:	Polymer-based nanoplasmonic components and devices
PMMA:	Poly-methyl-methacrylate
SEM:	Scanning electron microscope
SNOM:	Scanning near-field optical microscope
SP:	Surface plasmon
SPP:	Surface plasmon polariton
SPPBG:	Surface plasmon-polariton band gap
TE:	Transverse electric
TIR:	Total internal reflection
TM:	Transverse magnetic
UV:	Ultra-violet
WRR:	Waveguide-ring resonator
2D:	Two-dimensional
3D:	Three-dimensional

Chapter 1

Introduction

The remarkable increase in operational speed and component integration of chip-scale electronics observed in the last decades are pushing the data transport capabilities of conventional circuits to the limit. As the electronic components become increasingly small, so does the metal electrodes that connect them, thereby increasing the RC-delay, which limits the operational speed of the circuit. This limited bandwidth will become a severe limitation in the ever increasing demand for faster, smaller, and more efficient computer chips. One of the potential solutions to circumvent this problem is to utilize photonic circuits based on plasmonics, i.e., on SPPs. SPPs are electromagnetic surface waves which propagate along a metal-dielectric interface, with field maximum in the interface, and exponential field decay perpendicular to the interface. Their hybrid character (which is reflected by denoting them plasmon polaritons) arises as the waves essentially are light waves coupled to collective oscillations in the electron plasma in the surface of a metal. Photonic interconnects (waveguides) offer an almost unimaginable large bandwidth as compared to electronic interconnects, however, due to the diffraction limit of light a sizing mismatch exists between conventional photonic waveguides and electronic circuits which complicates the implementation. Plasmonic waveguides are not, in general, restricted in size by the diffraction limit, and thus offer the potential of becoming the next chip-scale technology [Fig. 1.1]. [1–8]

The promise of realizing ultra-compact integrated circuits by using plasmonic waveguides, along with other applications of plasmonics in, e.g., sensing of biomolecules, has motivated recent advances in the plasmonic research. However, the existence of surface waves in general has been known since the predictions a century ago by J. Zenneck [9] and A. Sommerfeld [10], and the existence SPPs in particular since the pathbreaking work of R. H. Ritchie in 1957 [11]. The occurrence of SPPs was demonstrated experimentally shortly thereafter by C. J. Powell and J. B. Swan in 1960 [12]. In these early demonstrations surface scientists utilized electrons for excitation of SPPs, as they were involved in electron energy-loss experiments. In the following years the research in SPPs slowly evolved as a separate branch of optics. Among the early important works can be mentioned the investigations of excitation of SPPs with light by A. Otto [13] and E. Kretschmann [14] and the investigation of SPPs in thin films by E. N. Economou [15]. In these early works the interest in SPPs was

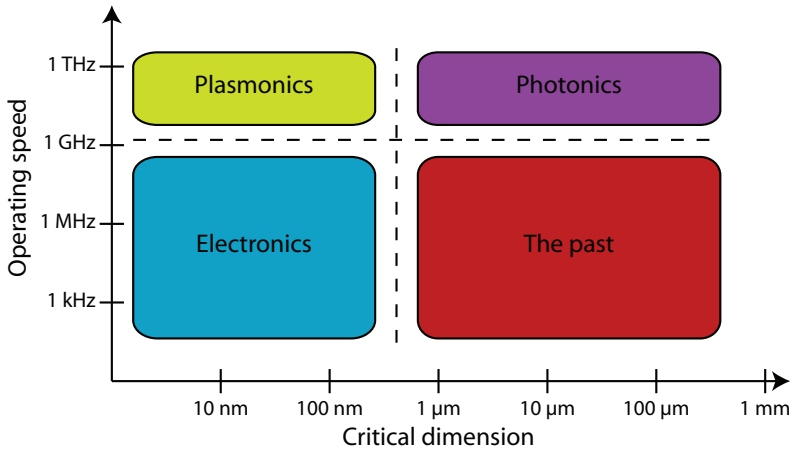

Figure 1.1: Critical dimensions and operating speeds of different technologies, illustrating the strengths and drawbacks of each technology [3].

mostly academical, but by the 1980s the potential of SPPs, particularly due to the strong field at the surface of a metal, was realized, and the research intensity started to increase [16–18]. It was not, however, until the fabrication and characterization methods evolved to enable structuring of surfaces on the nanoscale, and near-field imaging with nanometer resolution, that the research in plasmonic really started to gain momentum [1].

1.1 Fundamentals of SPPs

Surface plasmon polaritons differ from other types of surface polaritons as they are electromagnetic surface waves coupled to collective oscillations in the surface plasma of a conductor (usually a metal) [19]. This implies that the charge fluctuations are accompanied by a mixed transversal and longitudinal electromagnetic field, which disappears for $|z| \to \infty$ [Fig. 1.2]. The SPP fields are transverse magnetic in character (p-polarized waves), considered to propagate along the x-axis, and with the transverse component of the electric field E_z described by

$$E_z = E_{0z}^{\pm} \exp\left[i(\beta x - \omega t)\right] \exp(\pm i\gamma z), \tag{1.1}$$

with $+$ for $z \geq 0$ and $-$ for $z \leq 0$, and complex γ with a positive imaginary part. A similar relation accounts for the longitudinal component of the electric field. From this, it can be observed that the electric fields have a maximum at the interface and decays exponentially in the direction perpendicular to the metal-dielectric interface [Fig. 1.2(b)]. The complex wave vector along the direction of propagation $\beta = \beta' + i\beta''$, often denoted the propagation constant, is determined by the dispersion relation

$$\beta = k_0 \sqrt{\frac{\varepsilon_d \varepsilon_m}{\varepsilon_d + \varepsilon_m}}, \tag{1.2}$$

where $k_0 = {}^{2\pi}/_{\lambda}$ is the wave vector in free space, i.e., λ is the free-space wavelength, ε_d the relative permittivity characterizing the dielectric half space and ε_m the rel-

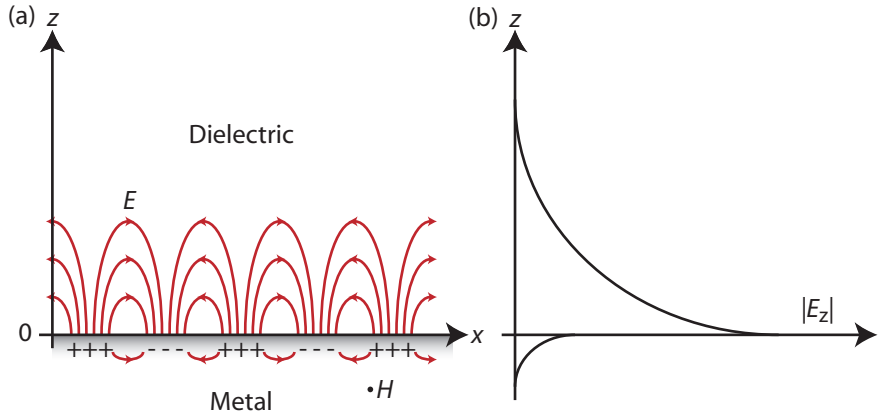

Figure 1.2: (a) Electromagnetic fields and charge distributions due to propagation of a SPP along a metal-dielectric interface in the x direction. The magnetic field is in the y direction only, illustrating the transverse magnetic character of SPPs. (b) Schematic drawing illustrating the exponential decay of the electric field in both dielectric and metal half space.

ative permittivity of the metal half space [18]. By plotting the dispersion relation one observes that it lies to the right of the light line ($k = \sqrt{\varepsilon_\mathrm{d}}\omega/c$), illustrating the non-radiative nature of SPPs [Fig. 1.3]. The momentum mismatch between light propagating in the dielectric and SPPs is illustrated by contemplating the light line and the SPP dispersion curve at a certain frequency ω_0. In order to couple light into SPP modes one must gain momentum, e.g., by employing gratings on the metal surface or by introducing another dielectric with a larger relative permittivity than the one at the SPP interface [18].

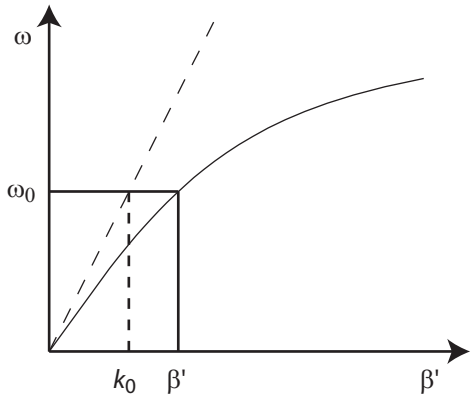

Figure 1.3: Illustration of the dispersion relation of SPPs at a planer metal-dielectric interface

The propagation length, i.e., the length SPPs propagate before the power has decayed to $1/e$ of its original value can be obtained as

$$L = \frac{1}{2\beta''}. \tag{1.3}$$

For silver, which is the metal with the lowest propagation loss in the visible spectrum, the propagation distances, along a planer silver-air interface, are typically in the range of 10 μm $-$ 100 μm, reaching as much as 1 mm at telecommunication wavelengths [1]. The attenuation of the SPP signal inherits from damping of electron oscillations, and this loss channel is one of the critical parameters when trying to realize plasmonic circuits. Another critical parameter is the mode confinement. As can be observed from the field profiles in the cross section [Fig. 1.2(b)], SPPs feature a strong inherent confinement in the direction perpendicular to the interface due to the exponential decay. At unstructured surfaces, however, there exists no lateral confinement of the SPP modes, which is essential in order to obtain guiding of SPPs, as small mode widths enable large bend angles with acceptable losses and increases the integration of plasmonic components on a chip. In order to realize plasmonic circuits one must thus design waveguides with a strong lateral (and vertical) confinement, with sufficiently long propagation lengths which, in general, are needed to support single mode propagation only.

1.2 SPP waveguiding

Waveguiding of SPP modes can be achieved in countless ways, and during the last decade several approaches have been successful in demonstrating confinement of SPPs. In the following a few of the most significant SPP waveguides will be briefly discussed in order to accentuate the assets of each approach. This will enable comparison to the performance of the DLSPPWs, which is the subject of this work.

One of the first approaches to demonstrate strong confinement of SPP modes has been to utilize nanometer-sized metal rods as waveguides. Numerical simulations showed that a beam diameter of only 33 nm at the wavelength $\lambda = 633$ nm can be achieved by using 20-nm-diameter silver rods embedded in a dielectric [20]. This extreme confinement is, however, achieved at the expense of propagation losses, and for such a structure the transmission loss is calculated to 3 dB/410 nm. In related work, where the plasmon excitation of metallic nanowires was investigated, it was observed that if the incident beam is polarized parallel to the long axis of the particle and illuminates one of the end of the nanowire, the local excitation can be guided along the nanowire by means of localized surface plasmon over distances larger than the incident wavelength [21]. The realization of metallic nanowires for guiding SPPs has recently been demonstrated with wire diameters of about 100 nm [22, 23].

Similar waveguiding properties were expected for the electromagnetic excitations supported by chains of nanospheres [24]. In this work silver particles of 50 nm in diameter has been considered, and the optimum guiding conditions have been found for an inter-particle spacing of 25 nm with a corresponding $1/e$ signal-damping length of 900 nm. It was suggested that in the case of the nanospheres the reduced metal content should lower the losses, but the higher scattering probability should increase them. The guiding of SPPs by closely spaced metallic nanoparticles has been confirmed, first by analysis of a macroscopic analogues operating in the microwave regime, consisting of closely spaced metal rods, by experiments and full field electrodynamic simulations [25]. Later the same group could present observations of electromagnetic energy transport from a localized sub-wavelength source to a localized detector over distances of about 0.5 μm in plasmon waveguides consisting of closely spaced silver

rods [26].

Another solution to achieving lateral confinement of SPPs has been to utilize the SPP band gap (SPPBG) effect, achieved by periodic texturing of a metal surface. The first demonstration of this effect, which has been reported, was observed (though indirectly) by performing angular and wavelength resolved measurements of the reflectivity of a periodically corrugated silver film [27]. In later reports SPP guiding has been directly demonstrated (at $\lambda = 782$ nm) along line defects in SPPBG structures using near-field microscopy [28]. In this work unhindered propagation of SPP fields in 3.2-μm-wide and 18-μm-long channels in the SPPBG structure has been observed.

One of the most extensively investigated approaches for guiding of SPPs is perhaps the most intuitive one, as lateral confinement of SPPs is achieved by shrinking the lateral dimension of the metal, thus obtaining a thin metal stripe waveguide embedded in a dielectric [29]. The metal stripe waveguide is characterized by a height and a width along with the dielectric constants of the enclosing dielectrics and the dielectric function of the metal [Fig. 1.4(a)]. The main component of the SPP electric field is oriented perpendicular to the metal surfaces and the modes supported by the structure can be divided into four families depending on the symmetry of their mode fields. In addition to the four fundamental modes that exist, numerous higher order modes are supported as well [29]. Depending on the symmetry of the main transverse electric field component the mode is either strongly confined to the stripe, with a resulting large propagation loss (short-range SPPs) or weakly confined with a small propagation loss (long-range SPPs). Several theoretical [29–31] and experimental [32–35] studies have been performed on this type of plasmonic with different aspect ratios of the height and width and different surrounding dielectrics, illustrating the diversity of this waveguiding approach.

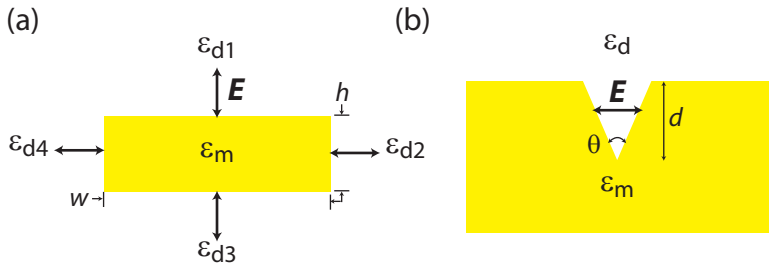

Figure 1.4: Schematic illustration of two types of SPP waveguides with direction of propagation out of the plane. (a) Stripe waveguide, which offer various polarization combinations. The stripe waveguide usually supports both long-range SPPs and short-range SPPs. (b) V-groove waveguide, where the CPP mode (primarily) is horizontally polarized. For deep enough grooves and small enough opening angles θ the CPP is strongly confined to the bottom of the V-groove.

The last approach to achieve SPP waveguiding to be mentioned here is the use of channels milled in an otherwise smooth metal film. This type of plasmonic waveguide modes have been denoted channel SPPs or CPPs for short [36]. It has been demonstrated that single-mode operation of a sub-wavelength plasmonic waveguide in the form of a V-groove on a metal surface can be achieved by adjusting the depth and opening angle of the groove. Strongly confined CPPs are shown to propagate in such waveguides with most of the mode power confined at or near the bottom of the groove

with the electric field (primarily) parallel to the sample surface plane [37]. V-groove waveguides has been fabricated using focused ion-beam milling and characterized using a near-field microscope. In addition to realizing sub-wavelength confinement and propagation length in the order of hundreds of micrometers in straight waveguides, several wavelength selective components such as Mach-Zehnder interferometers (MZIs) and WRRs have been realized using CPPs [38, 39].

1.3 Dielectric-loaded SPP waveguides

Lateral confinement of SPPs can also be achieved by utilizing an approach similar to conventional integrated optics, where one drastically reduces a waveguide mode size by employing high-index-contrast waveguides, i.e., waveguides having a core refractive index significantly different from that of the surrounding media [40]. A configuration which can be used for SPP waveguiding consists of a dielectric ridge placed on a metal surface [Fig. 1.5], where the lateral SPP confinement is achieved due to the fact that the SPP effective index is larger for the SPP mode supported by the metal-dielectric interface (even for thin dielectric layers) than for that supported by the metal-air interface [41–43]. Borrowing an analogous term from integrated op-

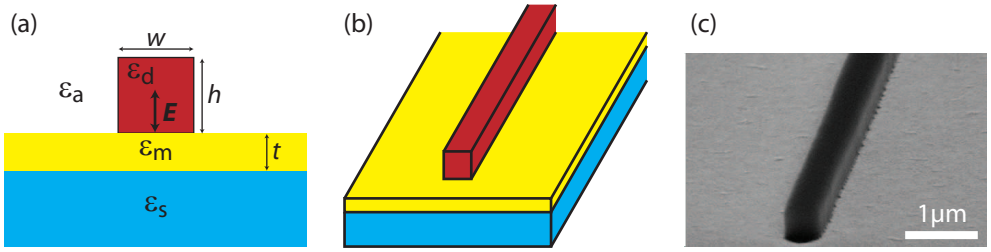

Figure 1.5: (a) Illustration of a DLSPPW in the cross-section. The rectangular dielectric ridge of height h, width w, and with dielectric constant ε_{d} is placed on top of a smooth gold film with thickness t and dielectric function ε_{m}. The gold film is supported by a glass substrate with dielectric constant ε_{s} and the electric field is p-polarized. (b) Schematic illustration of a straight DLSPPW and (c) Scanning electron microscope (SEM) image of a DLSPPW fabricated using deep-UV lithography.

tics [44, 45] this waveguide configuration has been denoted the dielectric-loaded SPP waveguide (DLSPPW) configuration. Preliminary experimental investigations of this waveguide structure have already indicated that the DLSPPWs can indeed be used for efficient guiding of SPP modes [42, 43]. The SPP mode is mostly confined to the dielectric ridge, and by properly designing the dimensions of the ridge, one can achieve single-mode guiding of sub-wavelength confined modes with propagation lengths comparable those of CPPs. One of the great assets of this technology in regard to the aforementioned SPP waveguides is that it is technologically simple, and that it can be adapted to large scale industrial fabrication using photolithography. It is furthermore a very versatile technology, as one can choose different types of dielectrics with a desired property, e.g., non-linearity or electro-optically active, and as one still have the possibility of structuring the underlying electrodes. Several theoretical and experimental studies of the DLSPPW structure have been performed by other groups, most of who are involved in the PLASMOCOM project, in parallel with what is presented

in this work [46–51].

The subject of this thesis is modeling, design, and characterization of passive DLSPPW components, and in the following an introduction to the theoretical and experimental methods used in the analysis of DLSPPWs will be given. In addition, the main results achieved in this work will be presented, and references to the relevant publications will be given.

Chapter 2

Effective index method calculations

The effective index method is one of the standard approaches for mode analysis of photonic waveguides, known to yield accurate mode effective indexes and field profiles for linearly polarized waveguide modes being far from cutoff [44, 52, 53]. The EIM is attractive due to the simplicity of the approach and the low complexity of the calculations, which keeps the computational time low, even for detailed analysis of, e.g., wavelength dependency of the mode effective index and propagation loss. In the consideration of dielectric rib waveguides, known from integrated optical circuits, the EIM provides accurate solutions under the conditions that; the aspect ratio h/w is small, i.e., the ridge is much wider that it is high, and that the effective indexes for the ridge region and the regions outside the ridge are close to each other [45]. The plasmonic dielectric ridge waveguide structure, considered in this work, does not obey these conditions as it is more or less rectangular, and as the difference in refractive index between the dielectric ridge and the surrounding air is large. The EIM has, however, proven to be accurate in the mode analysis of other types of plasmonic waveguides such as metal stripes embedded in a dielectric [54] and rectangular and V-shaped grooves in a smooth metal film [55], and is thus expected to be applicable in the analysis of DLSPPWs. In order to establish whether the EIM can provide accurate results in the analysis of DLSPPWs, a study of the accuracy has been performed by comparing with results obtained with the finite element method (FEM) for different dimensions of the dielectric ridge [56]. Here it was established that for tightly bound DLSPPW modes, far from cutoff, the deviation in calculated mode index and propagation loss is insignificant, and thus the EIM is applicable for modeling of the DLSPPW structures considered in this work. In the following section an introduction to the EIM is given, and it is demonstrated how it can be applied in the calculation of the mode effective index and propagation loss of a straight DLSPPW. In Sec. 2.2 the calculation of coupling between two DLSPPWs by means of the EIM is described. Finally in Sec. 2.3 a discussion of the results obtained with the EIM as part of this project is presented, and references to the relevant publications is given.

2.1 Calculation of mode index and propagation loss

The DLSPPW structure in its simples form, i.e., ignoring sample substrate, is a three layer geometry, with a bottom metallic substrate layer, a top ambient layer and a composite middle layer where the dielectric ridge is enclosed by the ambient layer [Fig. 2.1(a)]. In the following calculations the metal substrate layer is considered

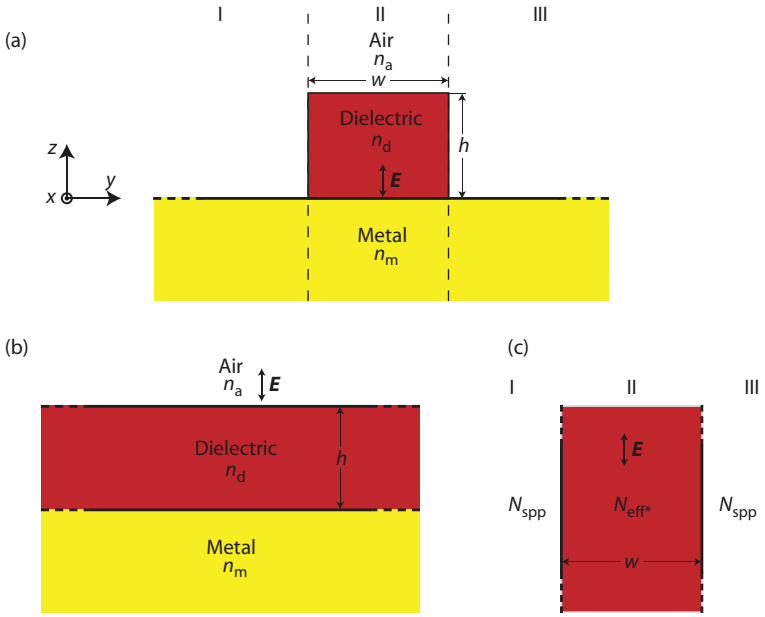

Figure 2.1: (a) Cross-sectional view of the DLSPPW structure. (b) The three-layer slab waveguide structure considered in the first step of the EIM, with finite height h of the dielectric layer. (c) The three-layer structure considered in the second step of the EIM, where the effective index found in the first step represents the middle layer of width w. The coordinate system used is also shown along with the orientation of the main component of the electric field in the case of TM (SPP) modes.

optically thick, and is thus regarded semi-infinite in extension. The surrounding ambient layer is considered being air with refractive index set to $n_a = 1$, and semi-infinite in extension. The rectangular dielectric ridge with refractive index n_d has the height h and width w.

In the effective index approximation the problem of calculating guided modes in the two-dimensional DLSPPW structure described above [Fig. 2.1(a)] is reduced to consecutively solving two one-dimensional multilayer slab waveguide geometries, which can be done by means of a standard multilayer waveguide mode solver. The essential assumption made in the effective index approximation is that the modes are linearly polarized and well above cutoff with most of the mode power concentrated in the ridge subregion, so that the field magnitude in the four corner regions are small enough to be neglected. In the first step of the EIM, mode effective indexes are found for each of three subregions I, II, and III shown in Fig. 2.1(a), by considering them infinite in lateral extension, thus solving three multilayer waveguide geometries. Subregion I and II are essentially a metal-dielectric interface, and thus the complex

mode effective index N_{spp} can be found by applying the SPP dispersion relation

$$N_{\mathrm{spp}} = \sqrt{\frac{\varepsilon_{\mathrm{a}}\varepsilon_{\mathrm{m}}}{\varepsilon_{\mathrm{a}} + \varepsilon_{\mathrm{m}}}}. \tag{2.1}$$

The complex mode effective index in the waveguide subregion II ($N_{\mathrm{eff}*}$) can be found, as a function of frequency and waveguide height, by contemplating the three layer air-dielectric-metal slab geometry [Fig. 2.1(b)]. In the second step of the EIM the finite width of the dielectric ridge is taken into account by solving the three layer slab geometry with effective indexes taken from the first calculation [Fig. 2.1(c)]. Thus the dependence of the complex mode effective index of the entire DLSPPW structure (N_{eff}) on wavelength, ridge height, and ridge width can be found.

A thorough investigation of the waveguiding properties, i.e., mode effective index, propagation loss, mode confinement, and single-mode requirement, has been performed for wavelengths in the telecommunication range as part of this project [56] (see App. A). In regard to the mode confinement it is advantageous to keep the height of the waveguide as large as possible, as allowed by the requirement of single-mode propagation, as most of the mode power in this case will be concentrated in the high-index ridge region. The choice of width, however, is slightly more complicated and is subject to a tradeoff between confinement and propagation loss. Although the mode effective index increases monotonously with increase in ridge width, the mode width has a distinct minimum. This can be envisaged as the field is squeezed into the ridge subregion when the width is decreased until a certain point, where the field no longer can be confined to the ridge. It then starts to spread out in the surrounding air, where the decay length is larger, thereby increasing the mode width. Considering the propagation loss, it is advantageous to keep the width of the waveguide as small as possible as an increasing part of the mode power will be carried outside the dielectric ridge, where the propagation loss is smaller. These considerations have led to a determination of the optimum waveguide parameters $h = 600$ nm and $w = 500$ nm, which ensures single-mode propagation, propagation lengths of ~ 50 μm, and sub-wavelength lateral confinement. It should be noted, that the DLSPPW, with these dimensions supports a TE mode, however, by controlling the polarization when exciting DLSPPW modes, this can be ignored as it is not coupled to. A wavelength analysis of the guiding properties has furthermore been performed with the EIM as part of this project in order to verify measurements performed on fabricated samples with dimensions close to the optimum as described above [57] (see App. C). These results show that the confinement and mode effective index decreases with wavelength, whereas the propagation length increases as expected.

2.2 Calculation of coupling between waveguides

Having established a method for calculation of mode effective index and propagation loss in isolated straight DLSPPWs with the EIM is indeed important and applicable in the analysis of many types of integrated optical components, however, it is also essential to be able to analyze the coupling between two adjacent waveguides. This is important, not only to determine the maximum level of integration, but also in order to enable modeling of various types of DLSPPW based components such as directional

couplers and waveguide crossings. In guided-wave photonics there are generally two approaches which can be applied in the analysis of coupling between two parallel waveguides. The coupled-mode approach, where the presence of an additional identical waveguide is included by considering it a perturbation to the unperturbed field profiles associated with a mode incident in an isolated waveguide, and the super-mode approach, where the phase difference between the two modes supported by the entire two-waveguide structure is considered. The coupled-mode approach has the advantage of being computationally simple, however, since the field profiles used in the calculation of the coupling are those of two waveguides in isolation, they are approximations valid for weak coupling only, i.e., large separation between the waveguides [45]. This is not the case for the plasmonic DCs considered in this work, and as the super-mode approach is straightforwardly implemented with the EIM in the case of DLSPPWs, this approach has been applied in the project.

When considering two parallel, and otherwise identical, DLSPPWs with the EIM, the first step is the same as for a single waveguide as one still needs to find two mode effective indexes only [Fig. 2.2]. The mode effective indexes of SPP modes propa-

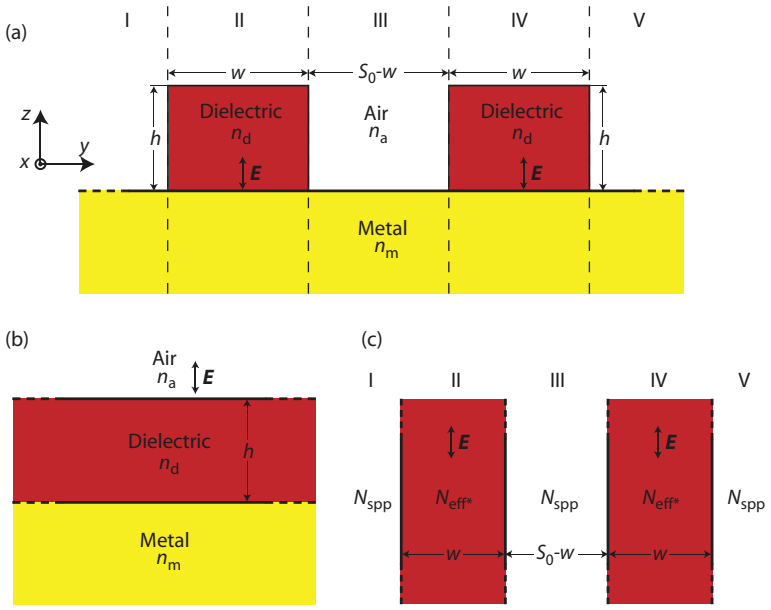

Figure 2.2: (a) Schematic showing two parallel DLSPPWs in the cross section, offset by the center-to-center separation S_0. (b) The three layer slab waveguide structure representing region II and IV in (a). (c) The five layer slab structure approximating the DC structure shown in (a). The mode effective index N_{spp} is calculated using Eq. 2.1 and represents regions I, III, and V, whereas the mode effective index N_{eff*}, which represents regions II and IV, is found by solving (b) for eigenmodes.

gating along a metal-air interface and of a three layer metal-dielectric-air structure [Fig. 2.2(b)] are found as described above. In the second step of the EIM, the appearance of a second parallel waveguide is included in the calculations, as it is no longer a three layer structure, but a five layer structure which must be contemplated [Fig. 2.2(c)]. Solving this geometry for eigenmodes by means of a multilayer waveguide solver, with the polarization shown in Fig. 2.2, one finds a symmetric N_{eff+}

and an anti-symmetric $N_{\text{eff-}}$ mode [Fig. 2.3]. The coupling between the two parallel

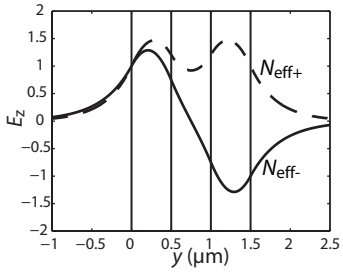

Figure 2.3: Cross-sectional profile of the EIM calculated symmetric ($N_{\text{eff+}}$) and anti-symmetric ($N_{\text{eff-}}$) DLSPPW modes supported by the parallel double waveguide structure.

waveguides can be contemplated as beating between these orthogonal and uncoupled modes, and thus the coupling constant can be found from the two mode effective indexes. The phase shift of each mode due to propagation over a distance L is given as

$$\phi_{\pm} = k_0 N_{\text{eff}\pm} L = \frac{2\pi}{\lambda} N_{\text{eff}\pm} L, \tag{2.2}$$

where λ is the vacuum wavelength. Ignoring the propagation losses the only effect on the modes due to propagation is this phase shift. Due to the beating between the two modes, when the accumulated phase difference between the two modes reaches a value of π, i.e., $\Delta\phi = \phi_+ - \phi_- = \pi$ the mode power has shifted completely from one waveguide to the other. This situation can envisioned by flipping the $N_{\text{eff-}}$ field profile around the horizontal axis in Fig. 2.3. The mode power will then have shifted from the left to the right waveguide. The length corresponding to this shift is denoted the coupling length L_{c} and can be found as

$$\Delta\phi = \frac{2\pi}{\lambda} \Delta N_{\text{eff}} L_{\text{c}} = \pi \Rightarrow L_{\text{c}} = \frac{\lambda}{2\Delta N_{\text{eff}}}, \tag{2.3}$$

from which the coupling constant can be found as

$$\kappa = \frac{\pi}{2L_{\text{c}}} = \frac{\pi \Delta N_{\text{eff}}}{\lambda}. \tag{2.4}$$

The task of determining the coupling between two parallel DLSPPWs, thus becomes a task of determining the dependency of the mode effective indexes $N_{\text{eff+}}$ and $N_{\text{eff-}}$ on the waveguide dimensions, the waveguide separation, and the wavelength, which can be done straightforwardly with the EIM as described above. When contemplating coupling between DLSPPWs with non-uniform separation between the waveguides, the analysis becomes slightly more complicated, as a dependence of the coupling constant on the separation must be established by means of the EIM [58] (see App. H).

2.3 Discussion and summary of modeling results

The EIM has successfully been applied in the analysis of DLSPPWs as part of this project, by using it to determine the guiding properties of straight waveguides and

the performance of various DLSPPW based components such as waveguide-ring resonators, directional couplers, and waveguide crossings. The validity of the EIM in this analysis has been verified by comparing obtained results with 2D and 3D FEM calculations and SNOM measurements. As mentioned above the EIM provides accurate results when the modes are linearly polarized and tightly bound to the dielectric ridge. 2D eigenmode analysis performed with the FEM confirmed that this is the case for the optimum ridge dimensions $h = 600$ nm and $w = 500$ nm at telecommunication wavelengths [Fig. 2.4] and [56]. The FEM calculated mode power distribution shows

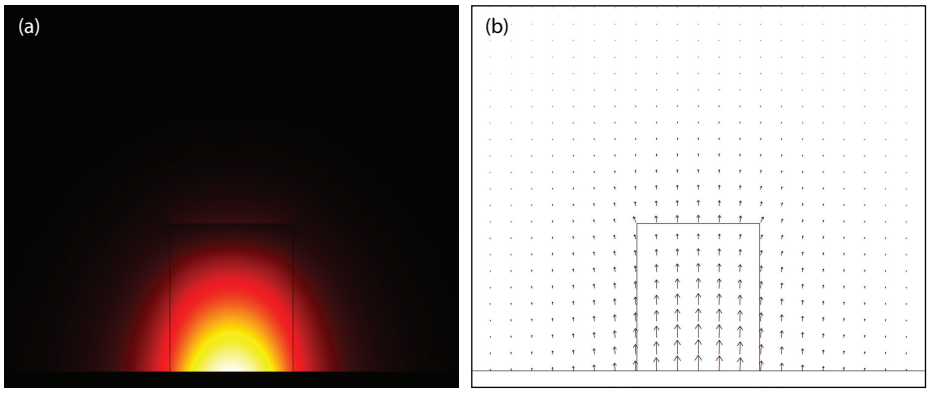

Figure 2.4: Mode power and field vector plots in the cross section of a DLSPPW with $h = 600$ nm and $w = 500$ nm at the telecommunication wavelength $\lambda = 1550$ nm, calculated using the FEM. (a) Normalized mode power distribution. (b) Normalized field vector plot of the electric field.

that the majority of the mode power is concentrated in the ridge, and that the mode power in the corner regions, which cannot be properly accounted for in the EIM, is insignificant [Fig. 2.4(a)]. Furthermore the FEM calculated field vector plot shows that, except for the corner regions, the electric field is very close to being linearly polarized, as assumed in the EIM [Fig. 2.4(b)]. A comparison of the FEM and EIM calculated mode effective index and propagation length of a DLSPPW with these dimensions, shows that the deviation in mode effective index is $\sim 1.5\%$ and the deviation in propagation length is $\sim 3\%$, which confirms the validity of the EIM in the analysis of the DLSPPWs [56]. In addition, near-field measurements performed with a SNOM on fabricated samples show a good correspondence to the EIM calculated mode effective indexes and propagation lengths [57, 59].

One of the major applications of the EIM in this work, has been to determine the optimum waveguide dimensions, i.e., height and width of the waveguide, when considering mode confinement, propagation loss, and single-mode propagation restraints. A thorough analysis performed at the telecommunication wavelength $\lambda = 1550$ nm, revealed that the optimum waveguide parameters are $h = 600$ nm and $w = 500$ nm [56] (see App. A). The wavelength dependency of the mode effective index and propagation loss has been determined, and found in good correspondence to the values determined experimentally with a SNOM [57] (see App. C). The wavelength dependency of the mode effective index is essential in the EIM modeling of WRRs, and it has been found that the EIM predicts the WRR performance well, when comparing to results obtained with a SNOM on fabricated WRRs [60] (see App. F). Finally the

EIM has been found very effective in the modeling of DLSPPW based DCs, where accurate knowledge of the dependency of the coupling constant on wavelength, waveguide dimensions, and waveguide separation is essential when designing DCs capable of physically separating two signals of different wavelengths [58] (see App. H). This knowledge has also been applied in the design of compact, low cross-talk, waveguide crossings [58].

In conclusion the EIM has been found extremely versatile and efficient in the modeling of various DLSPPW based components, due to the good correspondence with obtained experimental results, and the low computational time, which enables detailed modeling of various dependencies on, e.g., wavelength.

Chapter 3

Scanning near-field microscopy characterization

The experimental investigations conducted in this work have primarily been related to near-field optical imaging of samples containing various DLSPPW components. As described above SPPs are strongly confined to a metal-dielectric interface with exponentially decreasing (evanescent) fields extending only in the order of hundreds of nanometers into the dielectric, which makes investigation with conventional far-field imaging systems impossible. With the further confinement due to the nanostructured high-index dielectric ridges, a high-resolution near-field imaging technique is necessary in the characterization of DLSPPWs.

Near-field imaging systems, with optical resolution beyond the diffraction limit of light, were first proposed by E. H. Synge in 1928 [61] and later by J. A. O'Keefe in 1956 [62]. In 1972 E. A. Ash and G. Nicholls [63] described the realization of sub-wavelength resolution by utilizing a small pinhole in an opaque screen. With the development of the scanning tunneling microscope in 1982 [64], where tip-sample distance control to within a few Ångströms was achieved by implementation of a feedback loop, the road was paved for the realization of scanning near-field microscopes. In the mid-eighties the first near-field microscopes were realized almost simultaneously by two research groups in Switzerland and the United States [65,66]. Following these early demonstrations of near-field microscopes, the techniques were refined and extended to more applications [67–70] which allow simultaneous imaging of a sample topography and the optical near-field. This type of microscopes are generally denoted scanning near-field optical microscopes, and operate by adjusting the tip-sample distance by measuring the shear force between the two. In this work a collection mode SNOM, operating in the telecommunication range, has been applied in the characterization of DLSPPW components. [71,72]

3.1 Sample configuration and fabrication method

The DLSPPW samples investigated in this work consist of poly-methyl-methacrylate (PMMA) ridges ($n = 1.493$) deposited on ~ 60 nm thin gold films, thermally evaporated on 170 μm thick glass substrates. The thickness of the gold film is chosen in order to enable excitation of SPPs from the glass substrate side using the Kretschmann-

Raether configuration [18], while keeping the radiation losses back into the glass substrate as low as possible. After the initial substrate cleaning and gold deposition, a PMMA film was spin coated from 950K molecular weight PMMA resist (Allresist Gmbh, ref. AR-P 671.04) and soft-baked. Photolithography was performed with home made and commercially fabricated chromium masks on a Süss Microtech MJB4 mask aligner, equipped with UV250 optics, using the vacuum mode, and the resist was finally developed in methyl-isobutyl-ketone. The process of fabricating the DL-SPPW samples were performed at one of the PLASMOCOM partner institutions at the Institut Carnot de Bourgogne, Université de Bourgogne in France by Dr. Laurent Markey.

Due to in coupling considerations the DLSPPWs are extended by funnel shaped tapering structures [Fig. 3.1(a)]. In the initial sample investigations four different

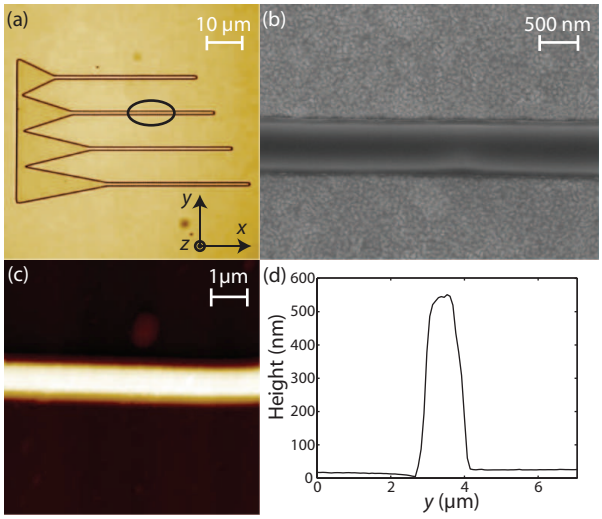

Figure 3.1: (a) Microscope image of a DLSPPW block with four different tapering structures. (b) SEM image of a straight section of a waveguide, revealing a waveguide width of $w \simeq 500$ nm. (c) AFM image of a straight section of a waveguide, and (d) cross sectional profile of the AFM image revealing a waveguide height of $h \simeq 550$ nm.

dimensions of the in coupling funnels were characterized, with a fixed width of 10 μm and a length varying from 10 μm to 25 μm in steps of 5 μm. This was done to determine the optimum funnel dimensions for efficiently exciting DLSPPW modes [59, 57] (see App. B and App. C). The width of the fabricated PMMA ridge waveguides has been investigated using a scanning electron microscope (SEM) [Fig. 3.1(b)], and is found to be $w \simeq 500$ nm in accordance with the optimum waveguide parameters found with the EIM. The height of the waveguides has been investigated with an atomic force microscope (AFM) [Fig. 3.1(c) and (d)], and is determined to be $h \simeq 550$ nm, which is only slightly lower than the desired optimum height of $h = 600$ nm. In addition to the straight waveguides several different DLSPPW components have been fabricated, such as waveguide S-bends, Y-splitters, waveguide-ring resonators, directional couplers, Mach-Zehnder interferometers, and Bragg gratings. The results of the near-field characterization of these components are summarized and discussed

in Sec. 3.3.

3.2 Near-field imaging of DLSPPW components

The fabricated DLSPPW samples are investigated using a SNOM operating in collection mode at telecommunication wavelengths. In order to excite DLSPPW modes, the samples are placed on an equilateral prism using index matching immersion oil between the sample substrate and the prism. A pigtail style fiber focuser is used to focus a p-polarized Gaussian laser beam at the gold surface, opposite to the DLSPPW structures, to a spot size of $\sim$ 15 μm [Fig. 3.2]. Using two tunable lasers

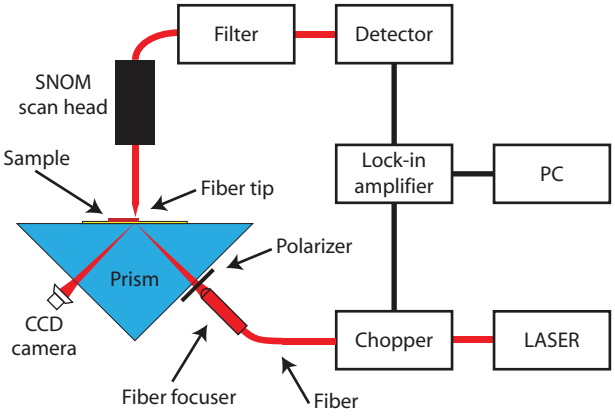

Figure 3.2: The experimental setup of the collection mode SNOM imaging system used to obtain near-field optical- and topographical images of the DLSPPW structures.

the telecommunication wavelength range from 1425 nm to 1625 nm can be covered. In the project two different excitation schemes have been utilized. In one scheme the lateral component of the incident wavevector can be matched to that of SPPs propagating along the gold-air interface by adjustment of the incident angle. In this scheme a regular glass prism is used, and the spot is positioned $\sim$ 20 μm before the in coupling funnel. In this configuration the funnels have the effect of coupling the SPPs into DLSPPW modes by total internal reflection (TIR) in the dielectric funnel. In addition the funnels will screen the propagation of SPPs at the gold-air interface close to the waveguides. In the other excitation scheme, which has been utilized in this project, SPPs are excited directly in the dielectric funnel, by employing a high-index prism and focusing the spot, under a different angle, directly below the funnel. In this configuration dielectric-loaded SPPs (DLSPPs) are excited by matching the lateral component of the incident wavevector to that of SPPs at the gold-PMMA interface.

Near-field optical and topographical images of the DLSPPW components are recorded simultaneously by raster scanning an uncoated tapered fiber tip across the sample surface. The fiber tip is etched to a tip diameter of a few hundred nanometers using hydrofluoric acid. When scanning the etched fiber across the sample surface, the tip scatters the optical near-field at an effective detection point $\sim$ 100 nm from its extremity point inside the fiber [73]. A part of this scattered field is coupled into

fiber modes, and is thus directed to the detector, where the intensity is recorded by a femtowatt InGaAs photoreceiver. As the optical signal incident on the detector is very weak a lock-in amplifier is used in conjunction with a chopper (inserted just after the laser before coupling into SPPs) in order to amplify the signal and reduce the disturbances from ambient radiation. In addition to this, a filter is inserted before the detector in order to minimize the disturbance from ambient illumination. The movement of the fiber tip in the xy-plane and the tip-sample distance is controlled by a SNOM scan head. The SNOM scan head is a commercial scan head fabricated by Danish Micro Engineering A/S, and it operates according to the shear force principle, where the tip oscillates in the plane parallel with the sample surface. Excitation and detection of the tip oscillations are made by means of piezo crystals. Coarse adjustment of the scan area can be performed as the SNOM scan head is fixed on a 3D scan stage which can be controlled by micrometer screws.

3.3 Discussion and summary of near-field microscopy results

By application of the SNOM, near-field optical and topographical imaging of DLSPPW components have been successfully performed at wavelengths in the telecommunication range. In the initial demonstration of excitation and propagation of DL-

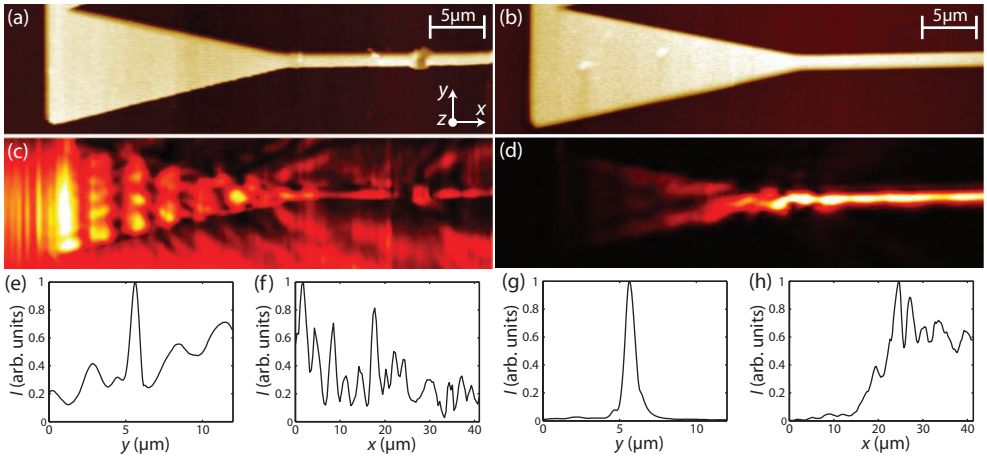

Figure 3.3: SNOM images of a 10×25 μm funnel in coupling for the free space excitation wavelength $\lambda = 1550$ nm. [(a) and (c)] Topographical and near-field optical images, respectively, when SPPs are excited at the gold-air interface outside the tapering region. [(b) and (d)] Topographical and near-field optical images, respectively, when DLSPPs are excited at the gold-PMMA interface inside the tapering region. [(e) and (g)] Averaged cross sectional profiles of the near-field optical image taken at the straight waveguide section just after the end of the funnel. [(f) and (h)] Averaged profiles of the near-field optical image taken parallel with the waveguide, through the funnel and waveguide regions.

SPPW modes, the excitation scheme where SPPs are excited at the gold-air interface, and subsequently coupled into the dielectric waveguides by means of a funnel was applied [Fig. 3.3(a) and (c)], and it proved successful with strong excitation of DLSPPW

modes [59] (see App. B). However, when characterizing S-bends, where the waveguides are displaced, it is apparent that this excitation technique has its limitations, as SPPs propagating at the gold-air interface parallel with the waveguide scatters off the dielectric ridges, when these are displaced. Thus another excitation technique has been proposed and realized, where SPPs are excited directly in the dielectric funnel by matching the mode effective index in this region [Fig. 3.3(b) and (d)]. Hence co-propagating SPPs at the gold-air interface are avoided as the excitation condition is not fulfilled for these [57] (see App. C). This excitation scheme also results in strong excitation of DLSPPW modes and as no SPPs are excited at the gold-air interface, the resulting near-field optical images are of much better contrast [Fig. 3.3]. Cross sectional profiles of the near-field optical signal taken at the straight waveguide right after the termination of the tapering region [Fig. 3.3(e) and (g)] shows that a strongly confined DLSPPW mode is excited in both cases, but that exciting DLSPPs directly in the funnel is preferable due to the very low background signal from SPPs propagating the gold-air interface. In addition to the investigation of different excitation schemes, an analysis of the effect of the funnel opening angle has been performed, both by means of near-field measurements with the SNOM and by applying the FEM (this work has been performed by A. V. Krasavin at the Queens University of Belfast, UK). These investigations show that in order to avoid a large degree of scattering out of the funnel at the transition between tapering region and waveguide, an opening angle smaller than $\sim 30°$ is desired. For a funnel width of 10 μm this implies funnel lengths larger than ~ 20 μm, which is still small enough to limit the losses due to propagation through the funnel [57].

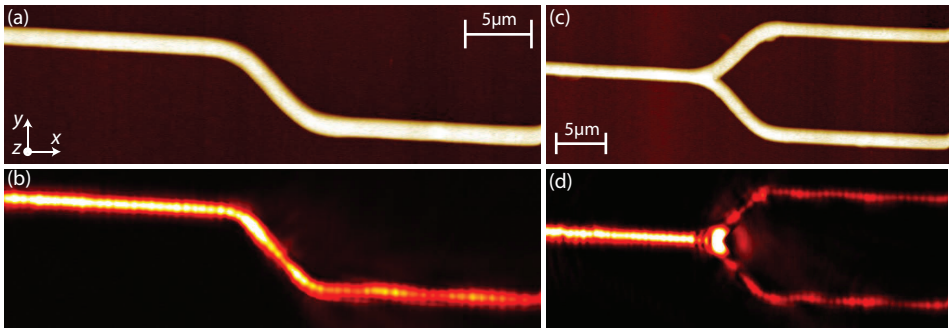

Figure 3.4: (a) Topographical and (b) near-field optical images recorded with the SNOM of an S-bend which displaces the waveguide by 5 μm over a distance of 10 μm, recorded for the free-space excitation wavelength $\lambda = 1550$ nm. (c) Topographical and (d) near-field optical images of a 50/50 Y-splitter with a final separation of 10 μm achieved over a distance of 10 μm, recorded for the free-space excitation wavelength $\lambda = 1550$ nm.

In addition to establishing an efficient method for exciting strongly confined (full width at half maximum of $\sim$ 700 nm) DLSPPW modes, with propagation lengths of $\sim$ 50 μm [59,57], one needs to realize waveguide bends and splitters along with various wavelength selective components in order to achieve compact integrated components based on DLSPPWs. The bending of DLSPPW modes has been investigated by fabrication of S-bends, where the waveguide is displaced with respect to its original, by utilizing a design based on sine curves [74], which implies continuous bend

curvature and thereby adiabatic modification of the DLSPPW mode through the bend [Fig. 3.4(a) and (b)]. S-bends with offsets ranging from 2 μm up to 15 μm, which implies radii of curvature down 1.95 μm, have been characterized with the SNOM, and it was found that the pure bend loss of the fabricated S-bends is very small for displacements ($d \leq 5$ μm), i.e., radius of curvature larger than ~ 4 μm, but that it dominates the loss contribution for large displacements [75] (See App. D). Near-field characterization of fabricated Y-splitters consisting of two mirrored S-bends, demonstrates the realization of a 50/50 splitting of the DLSPPW mode [Fig. 3.4(c) and (d)]. The dependency of the Y-splitter transmission on final arm separation has been investigated over a wide range from 4 μm to 30 μm, and as expected it has been found that the transmission is very similar to the S-bends, although the fabricated Y-splitters exhibit a rounding of the junction area, with a resulting additional radiation loss [75].

Beside the basic manipulation of the DLSPPWs with bends and splitters, several wavelength selective components have been designed, fabricated, and characterized. Wavelength filtering has been realized with waveguide-ring resonators, where a circular ring is placed in close proximity of the excited waveguide [Fig. 3.5(a)-(c)]. The

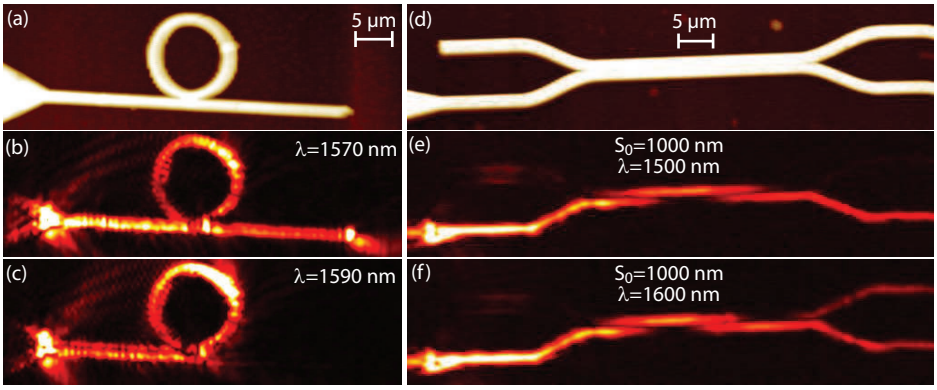

Figure 3.5: (a) Topographical image recorded with the SNOM of a WRR with a ring radius of $R \sim 5$ μm and a waveguide-ring gap of $g \simeq 0.5$ μm. [(b) and (c)] Near-field optical images with free-space excitation wavelengths $\lambda = 1570$ nm and $\lambda = 1590$ nm, respectively. (d) Topographical image of a DC with waveguide center-to-center separation of ($S_0 = 1000$ nm). [(e) and (f)] Near-field optical images of the DC shown in (a) for the wavelengths $\lambda = 1500$ nm $\lambda = 1600$ nm, respectively.

shown WRR feature nearly complete extinction (reaching ~ 13 dB at $\lambda = 1590$ nm) with a bandwidth of ~ 20 nm, and an insertion loss as low as 2 dB. By designing the ring radius, the transmission minima and maxima can be placed as desired, thus enabling suppression of desired wavelength bands [76,60] (See App. E and App. F). Wavelength filtering has also been realized by fabrication of Bragg gratings with 600-nm-period step in width sections, which exhibited well defined Bragg reflection and extinction in transmission within the wavelength interval 1540 nm $-$ 1600 nm [76].

The coupling between two parallel waveguides has been investigated by near-field characterization of fabricated DCs [Fig. 3.5(d)-(f)]. A thorough analysis of the influence of the waveguide separation and wavelength on the coupling length has been carried out with the SNOM. The DCs show strong coupling between the waveguides, with coupling lengths ranging from 6 μm to 20 μm depending on the separation and wavelength [77,58] (See App. G and App. H). Using the knowledge of the coupling

properties enables design of DC based demultiplexers, where physical separation of two signals with different wavelengths is achieved, and design of low cross-talk waveguide crossings [58].

In conclusion the near-field optical characterization of fabricated DLSPPW structures has demonstrated excitation of strongly confined single-mode waveguides with propagation length in the range of 50 μm at telecommunication wavelengths. The DLSPPW components presented here demonstrate only some of the possible application of the DLSPPW technology, and due to the good correspondence with the EIM and FEM modeling, design of specific components is made possible. This implies that a DLSPPW technology platform is established, which can be build upon for further advances in realizing compact integrated nanophotonic components.

Chapter 4

Conclusions and outlook

The primary focus of the work presented in this PhD thesis has been modeling, design, and characterization of plasmonic dielectric ridge waveguides and passive components based on these. The target is to establish a new technology platform for integratable nanophotonic components by combining photonics and electronics on the same chip. A thorough analysis of the guiding properties has been performed with the effective index method, and the validity of the method in the analysis of dielectric-loaded surface plasmon-polariton waveguides is verified by comparing to results obtained by 2D and 3D finite element calculations, as well as to near-field measurements. The resulting optimum waveguide parameters with regard to mode confinement, propagation loss, and single-mode constraints are a waveguide height of 600 nm and a width of 500 nm, at telecommunication wavelengths. This ensures a $1/e$ power decay length of ~ 50 μm and sub-wavelength confinement, necessary in order to realize a high degree of integration and sharp bending of the waveguides. Characterization of fabricated structures with a scanning near-field optical microscope reveals efficient excitation of tightly confined modes with negligible bend losses for bend radii larger than ~ 4 μm. Fabricated Y-splitters show a 50/50 splitting of the mode power, however, the resolution of the mask used in the fabrication process results in a rounding of the splitting region which causes undesired scattering losses compared to, e.g., the S-bends which do not suffer from this. 3D finite element modeling of Y-splitters with adiabatic splitting of the waveguide gives promise of minimizing this scattering loss by increasing the resolution of the lithography mask. In addition to the fabrication and characterization of basic bending and splitting components the performance of several different wavelength selective components has been investigated. Waveguide-ring resonators, where a ring resonator is placed in close proximity of a straight waveguide, demonstrate a periodic modulation of the output signal with a bandwidth of ~ 20 nm, an extinction ratio of ~ 13 dB in the transmission spectrum, and with insertion losses as low as 2 dB. Bragg gratings with a 600-nm-period step-in-width show suppression of the transmission signal in the wavelength interval of $1540\text{ nm} - 1600\text{ nm}$, thus demonstrating the realization of band-stop filters. Furthermore the effective index modeling and near-field imaging of directional couplers show the possibility of achieving physical separation of two signals of different wavelengths, which enable the realization of

demultiplexers.

The near-field optical characterization of basic waveguiding and various wavelength selective components presented in this work, demonstrate the achievement of integratable components capable of, e.g., filtering out undesired wavelength intervals and physically separating signals with different wavelengths. These achievements are important steps in the establishment of a DLSPPW technology platform and towards realization of ultra-compact integrated plasmonic circuits operating simultaneously as an electric circuit due to the underlying electrodes.

Outlook

The establishment of a new technological platform for integration of nanophotonic components using dielectric-loaded plasmonic waveguides paves the way for the development of a variety of components with enhanced functionalities for optical signal processing and on-electronic-chip interconnects. Although the transmission losses observed in the DLSPPWs are somewhat larger than in other conventional integrated photonic devices, the DLSPPW technology platform presents some intriguing novel applications due to the diversity in the choice of the dielectric and the presence of the metal electrodes below the dielectric ridges. The metal involved can be turned into an asset of the technology as the DLSPPW mode features a field maximum right at the metal surface, which makes it very sensitive to, e.g., thermo-optical or electro-optical effects induced by the electrodes. This could lead to electronic control of nanophotonic devices such as wavelength selective components, variable optical attenuators, and integrated power monitors. As the DLSPPW technology allows for a choice of the dielectric, one can also envision the usage of the strong electromagnetic field at the metal-dielectric interface by realizing non-linear photonic elements at low light intensities.

References

[1] W. L. Barnes, A. Dereux, and T. W. Ebbesen, "Surface plasmon subwavelength optics," Nature (London) **424**, 824–830 (2003).

[2] S. A. Maier and H. A. Atwater, "Plasmonics: Localization and guiding of electromagnetic energy in metal/dielectric structures," J. Appl. Phys. **98**, 011101 (2005).

[3] R. Zia, J. A. Schuller, A. Chandran, and M. L. Brongersma, "Plasmonics: the next chip-scale technology," Materials Today **9**, 20–27 (2006).

[4] W. L. Barnes, "Surface plasmon-polariton length scales: a route to subwavelength optics," J. Opt. A: Pure Appl. Opt. **8**, S87–S93 (2006).

[5] E. Ozbay, "Plasmonics: Merging photonics and electronics at nanoscale dimensions," Science **311**, 189–193 (2006).

[6] S. Lal, S. Link, and N. J. Halas, "Nano-optics from sensing to waveguiding," Nat. Photonics **1**, 641–648 (2007).

[7] W. A. Murray and W. L. Barnes, "Plasmonic materials," Adv. Mater. **19**, 3771–3782 (2007).

[8] T. W. Ebbesen, C. Genet, and S. I. Bozhevolnyi, "Surface-plasmon circuitry," Physics Today **61**, 44–50 (2008).

[9] J. Zenneck, "Breeding of even electromagnetic waves along an even conducting surface and its relation to radiotelegraphy," Ann. Phys. **23**, 846–866 (1907).

[10] A. Sommerfeld, "The broadening of the waves and the wireless telegraph," Ann. Phys. **28**, 665–736 (1909).

[11] R. H. Ritchie, "Plasma Losses by fast electrons in thin films," Phys. Rev. **106**, 874–881 (1957).

[12] C. J. Powell and J. B. Swan, "Effect of oxidation on the characteristic loss spectra of aluminum and magnesium," Phys. Rev. **118**, 640–643 (1960).

[13] A. Otto, "Excitation of nonradiative surface plasma waves in silver by the method of frustrated total reflection," Z. Phys. **216**, 398–410 (1968).

[14] E. Kretschmann, "Determination of optical constants of metals by excitation of surface plasmons," Z. Phys. **241**, 313 (1971).

[15] E. N. Economou, "Surface plasmons in thin films," Phys. Rev. **182**, 539–554 (1969).

[16] V. M. Agranovich and D. L. Mills, *Surface Polaritons - Electromagnetic Waves at Surfaces and Interfaces*, 1st ed. (North-Holland Publishing Group, Amsterdam, 1982).

[17] J. J. Burke, G. I. Stegeman, and T. Tamir, "Surface-polariton-like waves guided by thin, lossy metal films," Phys. Rev. B **33**, 5186–5201 (1986).

[18] H. Raether, *Surface Plasmons on Smooth and Rough Surfaces and on Gratings*, 1st ed. (Springer-Verlag, Berlin, 1988).

[19] E. Burstein, W. P. Chen, Y. J. Chen, and A. Hartstein, "Surface polaritons - propagating electromagnetic modes at interfaces," J. Vac. Sci. Technol. **11**, 1004–1019 (1974).

[20] J. Takahara, S. Yamagishi, H. Taki, A. Morimoto, and T. Kobayashi, Opt. Lett. **22**, 475 (1997).

[21] J.-C. Weeber, A. Dereux, C. Girard, J. R. Krenn, and J.-P. Goudonnet, "Plasmon polaritons of metallic nanowires for controlling submicron propagation of light," Phys. Rev. B **60**, 9061–9068 (1999).

[22] H. Ditlbacher, A. Hohenau, D. Wagner, U. Kreibig, M. Rogers, F. Hofer, F. R. Aussenegg, and J. R. Krenn, "Silver Nanowires as Surface Plasmon Resonators," Phys. Rev. Lett. **95**, 257403 (2005).

[23] A. W. Sanders, D. A. Routenberg, B. J. Wiley, Y. Xia, E. R. Dufresne, and M. A. Reed, "Silver Nanowires as Surface Plasmon Resonators," Nano Lett. **6**, 1822–1826 (2006).

[24] M. Quinten, A. Leitner, J. R. Krenn, and F. R. Aussenegg, "Electromagnetic energy transport via linear chains of silver nanoparticles," Opt. Lett. **23**, 1331 (1998).

[25] S. A. Maier, M. L. Brongersma, P. G. Kik, S. Meltzer, A. A. G. Requicha, and H. A. Atwater, "Plasmonics - A route to nanoscale optical devices," Adv. Mater. **13**, 1501–1505 (2001).

[26] S. A. Maier, P. G. Kik, H. A. Atwater, S. Meltzer, E. Harel, B. E. Koel, and A. A. G. Requicha, "Local detection of electromagnetic energy transport below the diffraction limit in metal nanoparticle plasmon waveguides," Nat. Mat. **2**, 229–232 (2003).

[27] S. C. Kitson, W. L. Barnes, and J. R. Sambles, "Full Photonic Band Gap for Surface Modes in the Visible," Phys. Rev. Lett. **77**, 2670–2673 (1996).

[28] S. I. Bozhevolnyi, J. Erland, K. Leosson, P. M. W. Skovgaard, and J. M. Hvam, "Waveguiding in Surface Plasmon Polariton Band Gap Structures," Phys. Rev. Lett. **86**, 3008–3011 (2001).

[29] P. Berini, "Plasmon-polariton waves guided by thin lossy metal films of finite width: Bound modes of symmetric structures," Phys. Rev. B **61**, 10484 (2000).

[30] R. Zia, M. D. Selker, and M. L. Brongersma, "Leaky and bound modes of surface plasmon waveguides," Phys. Rev. B **71**, 165431 (2005).

[31] J. Jung, T. Søndergaard, and S. I. Bozhevolnyi, "Theoretical analysis of square surface plasmon-polariton waveguides for long-range polarization-independent waveguiding," Phys. Rev. B **76**, 035434 (2007).

[32] J.-C. Weeber, J. R. Krenn, A. Dereux, B. Lamprecht, Y. Lacroute, and J. P. Goudonnet, "Near-field observation of surface plasmon polariton propagation on thin metal stripes," Phys. Rev. B **64**, 045411 (2001).

[33] T. Nikolajsen, K. Leosson, I. Salakhutdinov, and S. I. Bozhevolnyi, "Polymer-based surface-plasmon-polariton stripe waveguides at telecommunication wavelengths," Appl. Phys. Lett. **82**, 668–670 (2003).

[34] J.-C. Weeber, Y. Lacroute, A. Dereux, E. Devaux, T. Ebbesen, C. Girard, M. U. González, and A.-L. Baudrion, "Near-field characterization of Bragg mirrors engraved in surface plasmon waveguides," Phys. Rev. B **70**, 235406 (2004).

[35] P. Berini, R. Charbonneau, and N. Lahoud, "Long-Range Surface Plasmons on Ultrathin Membranes," Nano Lett. **7**, 1376 (2007).

[36] I. V. Novikov and A. A. Maradudin, "Channel polaritons," Phys. Rev. B **66**, 035403 (2002).

[37] D. K. Gramotnev and D. F. P. Pile, "Single-mode subwavelength waveguide with channel plasmon-polaritons in triangular grooves on a metal surface," Appl. Phys. Lett. **85**, 6323 (2004).

[38] S. I. Bozhevolnyi, V. S. Volkov, E. Devaux, J.-Y. Laluet, and T. W. Ebbesen, "Channel plasmon subwavelength waveguide components including interferometers and ring resonators," Nature (London) **440**, 508–511 (2006).

[39] V. S. Volkov, S. I. Bozhevolnyi, E. Devaux, J.-Y. Laluet, and T. W. Ebbesen, "Wavelength selective nanophotonic components utilizing channel plasmon polaritons," Nano Lett. **7**, 880–884 (2007).

[40] C. Manolatou, S. G. Johnson, S. Fan, P. R. Villeneuve, H. A. Haus, and J. D. Joannopoulos, "Hign-density integrated optics," J. Lightwave Technol. **17**, 1682 (1999).

[41] A. Hohenau, J. R. Krenn, A. L. Stepanov, A. Drezet, H. Ditlbacher, B. Steinberger, A. Leitner, and F. R. Aussenegg, "Dielectric optical elements for surface plasmons," Opt. Lett. **30**, 893 (2005).

[42] B. Steinberger, A. Hohenau, H. Ditlbacher, A. L. Stepanov, A. Drezet, F. R. Aussenegg, A. Leitner, and J. R. Krenn, "Dielectric stripes on gold as surface plasmon waveguides," Appl. Phys. Lett. **88**, 094104 (2006).

[43] C. Reinhardt, S. Passinger, B. N. Chichkov, C. Marquart, I. P. Radko, and S. I. Bozhevolnyi, "Laser-fabricated dielectric optical components for surface plasmon polaritons," Opt. Lett. **31**, 1307–1309 (2006).

[44] H. Kogelnik, *Theory of Dielectric Waveguides - In Integrated Optics* (Springer-Verlag, Berlin, 1979). Edited by T. Tamir.

[45] A. B. Buckman, *Guided-Wave Photonics*, 1st ed. (Saunders College Publishing, 1992).

[46] B. Steinberger, A. Hohenau, H. Ditlbacher, F. R. Aussenegg, A. Leitner, and J. R. Krenn, "Dielectric stripes on gold as surface plasmon waveguides: Bends and directional couplers," Appl. Phys. Lett. **91**, 081111 (2007).

[47] A. V. Krasavin and A. V. Zayats, "Passive photonic elements based on dielectric-loaded surface plasmon polariton waveguides," Appl. Phys. Lett. **90**, 211101 (2007).

[48] S. Massenot, J. Grandidier, A. Bouhelier, G. C. des Francs, L. Markey, J.-C. Weeber, A. Dereux, J. Renger, M. U. Gonzàlez, and R. Quidant, "Polymer-metal waveguides characterization by Fourier plane leakage radiation microscopy," Appl. Phys. Lett. **91**, 243102 (2007).

[49] A. V. Krasavin and A. V. Zayats, "Three-dimensional numerical modeling of photonic integration with dielectric-loaded SPP waveguides," Phys. Rev. B **78**, 045425 (2008).

[50] S. Massenot, J.-C. Weeber, A. Bouhelier, G. C. des Francs, J. Grandidier, L. Markey, and A. Dereux, "Differential method for modelling dielectric-loaded surface plasmon polariton waveguides," Opt. Express **16**, 17599–17608 (2008).

[51] A. Seidel, C. Ohrt, S. Passinger, C. Reinhardt, R. Kiyan, and B. N. Chichkov, "Nanoimprinting of dielectric loaded surface-plasmon-polariton waveguides using masters fabricated by 2-photon polymerization technique," J. Opt. Soc. Am. B **26**, 810–812 (2009).

[52] A. Kumar, D. F. Clark, and B. Culshaw, "Explanation of errors inherent in the effective-index method for analyzing rectangular-core waveguides," Opt. Lett. **13**, 1129 (1988).

[53] K. S. Chiang, "Performance of the effective-index method for the analysis of dielectric waveguides," Opt. Lett. **16**, 714 (1991).

[54] A. Boltasseva, T. Nikolajsen, K. Leosson, K. Kjaer, M. S. Larsen, and S. I. Bozhevolnyi, "Integrated Optical Components Utilizing Long-Range Surface Plasmon Polaritons," J. Lightwave Technol. **23**, 413 (2005).

[55] S. I. Bozhevolnyi, "Effective-index modeling of channel plasmon polaritons," Opt. Express **14**, 9467–9476 (2006).

[56] T. Holmgaard and S. I. Bozhevolnyi, "Theoretical analysis of dielectric-loaded surface plasmon-polariton waveguides," Phys. Rev. B **75**, 245405 (2007).

[57] T. Holmgaard, S. I. Bozhevolnyi, L. Markey, A. Dereux, A. V. Krasavin, P. Bolger, and A. V. Zayats, "Efficient excitation of dielectric-loaded surface plasmon-polariton waveguide modes at telecommunication wavelengths," Phys. Rev. B **78**, 165431 (2008).

[58] T. Holmgaard, Z. Chen, S. I. Bozhevolnyi, L. Markey, and A. Dereux, "Design and characterization of dielectric-loaded plasmonic directional couplers," J. Lightwave Technol. (2009). (Submitted).

[59] T. Holmgaard, S. I. Bozhevolnyi, L. Markey, and A. Dereux, "Dielectric-loaded surface plasmon-polariton waveguides at telecommunication wavelengths: Excitation and characterization," Appl. Phys. Lett. **92**, 011124 (2008).

[60] T. Holmgaard, Z. Chen, S. I. Bozhevolnyi, L. Markey, and A. Dereux, "Dielectric-loaded plasmonic waveguide-ring resonators," Opt. Express **17**, 2968–2975 (2009).

[61] E. H. Synge, "A suggested model for extending microscopic resolution into the ultra-microscopic region," Philos. Mag. **6**, 356–362 (1928).

[62] J. A. O'Keefe, "Resolving Power of Visible Light," J. Opt. Soc. Am. **46**, 359 (1956).

[63] E. A. Ash and G. Nicholls, "Super-resolution Aperture Scanning Microscope," Nature **237**, 510–512 (1972).

[64] G. Binnig and H. Rohrer, "Scanning tunneling microscopy," Helv. Phys. Acta **55**, 726–735 (1982).

[65] D. W. Pohl, W. Denk, and M. Lanz, "Optical stethoscopy: Image recording with resolution $\lambda/20$," Appl. Phys. Lett. **44**, 651–653 (1984).

[66] A. Lewis, M. Isaacson, A. Harootunian, and A. Muray, "Development of a 500 Å spatial resolution ligth microscope," Ultramicroscopy. **13**, 227–232 (1984).

[67] U. Dürig, D. W. Pohl, and F. Rohner, "Near-field optical-scanning microscopy," J. Appl. Phys. **59**, 3318–3327 (1986).

[68] E. Betzig, M. Isaacson, and A. Lewis, "Collection mode near-field scanning optical microscopy," Appl. Phys. Lett. **51**, 2088–2090 (1987).

[69] E. Betzig, P. L. Finn, and J. S. Weiner, "Combined shear force and near-field scanning optical microscopy," Appl. Phys. Lett. **60**, 2484–2486 (1992).

[70] K. Karrai and R. D. Grober, "Piezoelectric tip-sample distance control for near field optical microscopes," Appl. Phys. Lett. **66**, 1842–1844 (1995).

[71] D. Courjon, *Near-Field Microscopy and Near-Field Optics*, 1st ed. (Imperial College Press, London, 2003).

[72] L. Novotny and B. Hecht, *Principles of nano-optics*, 1st ed. (Cambridge University Press, Cambridge, 2006).

[73] I. P. Radko, S. I. Bozhevolnyi, and N. Gregersen, "Transfer function and near-field detection of evanescent waves," Appl. Opt. **45**, 4054–4061 (2006).

[74] A. Kumar and S. Aditya, "Performance of s-bends for integrated-optic waveguides," Microwave Opt. Technol. Lett. **19**, 289–292 (1998).

[75] T. Holmgaard, Z. Chen, S. I. Bozhevolnyi, L. Markey, A. Dereux, A. V. Krasavin, and A. V. Zayats, "Bend- and splitting loss of dielectric-loaded surface plasmon-polariton waveguides," Opt. Express **16**, 13585–13592 (2008).

[76] T. Holmgaard, Z. Chen, S. I. Bozhevolnyi, L. Markey, A. Dereux, A. V. Krasavin, and A. V. Zayats, "Wavelength selection by dielectric-loaded plasmonic components," Appl. Phys. Lett. **94**, 051111 (2009).

[77] Z. Chen, T. Holmgaard, S. I. Bozhevolnyi, A. V. Krasavin, A. V. Zayats, L. Markey, and A. Dereux, "Wavelength-selective directional coupling with dielectric-loaded plasmonic waveguides," Opt. Lett. **34**, 310–312 (2009).

List of publications

Articles in peer-refereed journals (included in appendix)

1. T. Holmgaard and S. I. Bozhevolnyi, *"Theoretical analysis of dielectric-loaded surface plasmon-polariton waveguides"*, Phys. Rev. B **75**, 245405 (2007)

2. T. Holmgaard, S. I. Bozhevolnyi, L. Markey, and A. Dereux, *"Dielectric-loaded surface plasmon-polariton waveguides at telecommunication wavelengths: Excitation and characterization"*, Appl. Phys. Lett. **92**, 011124 (2008)

3. T. Holmgaard, S. I. Bozhevolnyi, L. Markey, A. Dereux, A. V. Krasavin, P. Bolger, and A. V. Zayats, *"Efficient excitation of dielectric-loaded surface plasmon-polariton waveguide modes at telecommunication wavelengths"*, Phys. Rev. B **78**, 165431 (2008)

4. T. Holmgaard, Z. Chen, S. I. Bozhevolnyi, L. Markey, A. Dereux, A. V. Krasavin, and A. V. Zayats, *"Bend- and splitting loss of dielectric-loaded surface plasmon-polariton waveguides"*, Opt. Express **16**, 13585-13592 (2008)

5. T. Holmgaard, Z. Chen, S. I. Bozhevolnyi, L. Markey, A. Dereux, A. V. Krasavin, and A. V. Zayats, *"Wavelength selection by dielectric-loaded plasmonic components"*, Appl. Phys. Lett. **94**, 051111 (2009)

6. T. Holmgaard, Z. Chen, S. I. Bozhevolnyi, L. Markey, and A. Dereux, *"Dielectric-loaded plasmonic waveguide-ring resonators"*, Opt. Express **17**, 2968-2975 (2009)

7. Z. Chen, T. Holmgaard, S. I. Bozhevolnyi, A. V. Krasavin, A. V. Zayats, L. Markey, and A. Dereux, *"Wavelength-selective directional coupling with dielectric-loaded plasmonic waveguides"*, Opt. Lett. **34**, 310-312 (2009)

8. T. Holmgaard, Z. Chen, S. I. Bozhevolnyi, L. Markey, and A. Dereux, *"Design and characterization of dielectric-loaded plasmonic directional couplers"*, J. Lightwave Technol. (submitted) (2009)

Miscellaneous

1. T. Holmgaard, S. I. Bozhevolnyi, L. Markey, A. Dereux, A. V. Krasavin, and A. V. Zayats, *"Excitation and characterization of dielectric-loaded surface plasmon-polariton waveguides at telecommunication wavelengths"*, SPIE Proceedings **6988**, T9880 (2008)

2. *"Practical Y-splitter steers plasmons"*, Optics and laser Europe, November, 12 (2008)

3. *"Building better optical components using plasmonics"*, Photonics Spectra, May, 19-20 (2009)

Presentations

1. Poster presentation at the Third International Conference on Surface Plasmon Photonics, June 2007, Dijon, France

2. Poster presentation at the Danish optical society (DOPS) annual meeting, December 2007, Risø National Laboratory, Denmark

3. Oral presentation at the SPIE Photonics Europe Conference, April 2008, Strasbourg, France

4. Poster presentation at the Final Research Workshop and Network Council Meeting of Plasmo-nano-devices Network of Excellence, May 2008, Göteborg, Sweden

5. Poster presentation at the Danish optical society (DOPS) annual meeting, June 2008, Nyborg, Denmark

6. Poster presentation at the Second European Topical Meeting on Nanophotonics and Metamaterials, January 2009, Seefeld, Austria

7. Oral presentation at the European Concertation Meeting on Nanophotonics (FP7-ICT), February 2009, Florence, Italy

8. Poster presentation at the Fourth International Conference on Surface Plasmon Photonics, June 2009, Amsterdam, The Netherlands

Summary in Danish

Denne afhandling omhandler modellering, design og karakterisering af dielektriske overflade plasmon polariton bølgeledere ved telekommunikationsbølgelængder. Arbejdet er sigtet mod at etablere en ny teknologiplatform for integrerbare nanofotoniske komponenter ved at kombinere fotoniske og elektroniske komponenter på samme chip. De dielektriske overflade plasmon polariton bølgeledere består af dielektriske striber, som i tværsnittet er rektangulære og i nanometer størrelse ($\sim 600 \times 500$ nm^2), som er deponeret på en jævn metal film. Overflade plasmon polaritonerne, der er elektromagnetiske overflade bølger som er bundet til, og udbreder sig langs, en metal-dielektrisk grænseflade, er stærkt begrænset til striben grundet den store forskel i brydningsindeks mellem den dielektriske stribe og den omgrænsende luft. Teoretiske undersøgelser af bølgelederstrukturen, udført med effektiv indeks metoden (EIM), viser at understøttelse af én bølgetilstand med sub-bølgelængde begrænsning og en udbredelseslængde på ~ 50 μm kan opnås ved telekommunikationsbølgelængder ($\lambda \sim 1500$ nm), ved omhyggeligt design af bølgeleder dimensionerne. Nærfelts optisk afbildning af fremstillede bølgeledere, udført ved hjælp af et skannende nærfelts optisk mikroskop (SNOM) opererende i opsamlingstilstand, bekræfter, at de dielektriske striber, med de designede dimensioner, understøtter stærkt bundne bølger med udbredelseslængder som forudset af EIM beregningerne. De dielektriske overflade plasmon polariton tilstande bliver eksiteret ved anvendelse af Kretschmann-Raether konfigurationen, hvor en laser stråle fokuseres på bagsiden af metal filmen under en bestem vinkel. Det viser sig, at effektiv eksitering med lav baggrundsstøj kan opnås ved at eksitere overflade plasmon polaritoner direkte i en dielektrisk tragt, som ligger i forlængelse af stribe bølgelederne. Effekten af at bøje og splitte bølgelederne på tabet undersøges ved brug af et SNOM, og resultaterne viser, at for bøjninger med en bøjningsradius på $R \gtrsim 4$ μm er der ikke nævneværdige bøjningstab. For fremstillede Y-splittere findes det, at en lille bøjning lige i split regionen (grundet opløsningen på den maske som anvendes i prøve fremstillingen) giver årsag til spredningstab, hvilket forværrer de overordnede transmissions egenskaber. 3D finite element simuleringer viser dog, at dette kan afhjælpes ved at øge opløsningen af masken.

Udover den optiske nærfelts karakterisering af simple bølgeleder komponenter som S-bøjninger og Y-splittere undersøges virkningen af flere forskellige passive bølgelæng-

de sensitive komponenter ved hjælp af et SNOM. Periodisk modulering af transmissionen opnås ved at realisere bølgeleder-ring resonatorer, hvor en ring resonator placeres i tæt afstand til en lige bølgeleder som eksiteres ved forskellige bølgelængder. Den fremstillede resonator med den bedst afstemte kobling til ringen udviser et tab på $\sim$ 2 dB, en smal indstillelig båndbredde på $\sim$ 20 nm og stor kontrast ($\sim$ 13 dB) i transmissionsspektret. Komponentens karakteristika findes i god overensstemmelse med resultater opnået ved anvendelse af EIM beregninger. Bølgelængde filtrering er også opnået ved at realisere Bragg gitre. Gitre med 600 nm lange periodiske spring i bredden (fra 500 nm til 2 μm), med 300 nm lange intervaller mellem brede sektioner og et varierende antal perioder: N=10, 20, 30 og 50 fremstilles og karakteriseres med et SNOM. Den bedste virkning findes for et 30-perioder Bragg gitter, hvor en veldefineret Bragg refleksion og dæmpning af transmissionen i bølgelængdeintervallet 1540 nm $-$ 1600 nm observeres. Slutteligt undersøges koblingen mellem to parallelle bølgeledere ved at fremstille og karakterisere retningsbestemte koblere, hvor de to bølgeledere bringes i tæt kontakt ved hjælp af S-bøjninger. Betydningen af afstanden mellem bølgelederne samt bølgelængden etableres og der findes en overordentlig god overensstemmelse til EIM resultater. Med udgangspunkt i EIM beregninger introduceres en metode til design af retningsbestemte koblere, som kan separere to signaler med forskellig bølgelænge, samt til design af meget kompakte bølgeleder kryds med en meget lille grad af cross-talk.

Appendix A

Phys. Rev. B **75**, 2007

T. Holmgaard and S. I. Bozhevolnyi, *"Theoretical analysis of dielectric-loaded surface plasmon-polariton waveguides"*, Phys. Rev. B **75**, 245405 (2007).

Theoretical analysis of dielectric-loaded surface plasmon-polariton waveguides

Tobias Holmgaard* and Sergey I. Bozhevolnyi
Department of Physics and Nanotechnology, Aalborg University, Skjernvej 4A, DK-9220 Aalborg Øst, Denmark
(Received 15 December 2006; revised manuscript received 16 March 2007; published 6 June 2007)

Waveguiding of surface plasmon-polaritons (SPPs) by a dielectric ridge placed on a metal surface is analyzed using the effective-index method (EIM) and the finite element method (FEM). Main characteristics of these dielectric-loaded SPP waveguide (DLSPPW) structures, i.e., the mode effective index, confinement, and propagation length, are calculated at the telecom wavelength $\lambda = 1.55$ μm for different widths and thicknesses of a polymer ridge (with the refractive index of 1.535) placed on a gold film surface. The condition for single-mode guiding is investigated using the EIM, and it is found that single-mode DLSPPW guiding can be realized for ridge thicknesses smaller than ~630 nm and widths below ~655 nm (when decreasing the ridge thickness, the ridge width suitable for single-mode guiding increases). It is also established that, in contrast to the usual trade-off, the DLSPPW mode lateral confinement can be improved simultaneously with the increase in the mode propagation length by choosing the appropriate ridge thickness. The accuracy of the EIM is evaluated by comparing the computed mode characteristics with those obtained with the FEM and found rather good for the modes being far from cutoff.

DOI: 10.1103/PhysRevB.75.245405 PACS number(s): 73.20.Mf, 71.36.+c, 78.20.Bh, 42.79.Gn

I. INTRODUCTION

The recent explosive growth of research into plasmonics has been largely stimulated by the expectation that plasmonic circuits would be able of combining the best sides of electronic (with respect to physical dimensions) and optical (with respect to operation speed) circuits. Plasmonic circuits are perceived as consisting of photonic components utilizing, in one or another form, surface plasmon-polaritons (SPPs), which are quasi-two-dimensional electromagnetic excitations, propagating along a metal-dielectric interface and having the field components decaying exponentially into both neighboring media.[1] The latter feature results in the SPP characteristics being a mixture of those found for waves in dielectric and metal media. Typically, SPPs are tightly bound to the metal surface penetrating ~100 nm in the dielectric and ~10 nm in the metal, a feature that implies the possibility of using SPPs for subwavelength optical interconnects and photonic circuits.[2] The main issue in this context is to strongly confine the SPP field in the cross section perpendicular to the SPP propagation direction (smaller cross sections ensure smaller bend losses and higher densities of components) while keeping relatively low propagation losses.

It has been shown using numerical simulations that nanometer-sized metal rods can support extremely confined SPP modes propagating though only over hundreds of nanometers.[3] Similar properties were expected[4] and indeed found[5] for the electromagnetic excitations supported by chains of metal nanospheres. SPP propagation along metal stripes[6] and channels in periodically corrugated regions[7] has also exhibited propagation losses increasing drastically with the decrease in the stripe or channel width. Recently, SPP gap waveguides based on the SPP propagation between profiled metal surfaces have been suggested[8] and various nanowaveguide configurations have been modeled.[9] Quite recently, channel SPP modes, or channel plasmon-polaritons (CPPs),[10] where the electromagnetic radiation is concentrated at the bottom of V-shaped grooves milled in a metal film, have been first predicted[11] and then experimentally shown[12] to exhibit useful subwavelength confinement and moderate propagation loss. Moreover, various CPP-based subwavelength waveguide components, including Mach-Zehnder interferometers and waveguide-ring resonators, have been successfully realized.[13] It should be noted though that, in general, the SPP confinement is achieved primarily by decreasing the SPP spatial extent into the dielectric, thereby increasing the portion of SPP power being absorbed by the metal, so that the choice of optimum guiding configuration is subject to trade-off with many intricate issues yet to be elucidated.

In conventional integrated optics, one can drastically reduce a waveguide mode size in the lateral cross section by employing high-index-contrast waveguides, i.e., waveguides having a core refractive index significantly different from that in surrounding media.[14] A similar approach involving SPP modes has also been very recently demonstrated.[15,16] The configuration used consists of a dielectric ridge placed on a metal surface, and the lateral SPP confinement is achieved due to the fact that the SPP effective index is larger for the SPP mode supported by the metal-dielectric interface (even for thin dielectric layers) than for that supported by the air-metal interface.[17] Borrowing an analogous term from integrated optics,[18,19] such a waveguide configuration will be hereafter called the dielectric-loaded SPP waveguide (DLSPPW) configuration. The reported experimental results have already indicated that the DLSPPWs can indeed be used for efficient guiding of SPP modes.[15,16] Some of the DLSPPW characteristics have also been modeled with the effective-index approximation,[15] but there are a number of very important issues, e.g., the aforementioned trade-off, that require detailed and careful theoretical consideration using accurate modeling tools.

The effective-index method (EIM) is one of the standard methods for analysis of photonic and SPP waveguides, which is known to yield reasonably accurate results for weakly guided (linearly polarized) modes being far from cutoff.[18–20] It has also been found useful when considering channel SPP

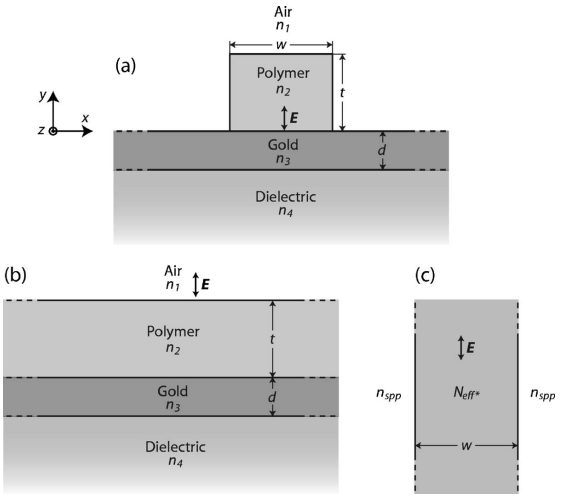

FIG. 1. (a) Cross-sectional view of the DLSPPW structure under investigation. (b) The four-layer and (c) three-layer structures considered correspondingly in the first and second steps of the EIM-1. The coordinate system used is also shown along with the orientation of the main component of the electric field in the case of TM modes.

modes.[21] Combined with the simplicity of the EIM, this makes it attractive for consideration of DLSPPW mode characteristics provided that its accuracy and validity domain are established. Various numerical methods such as the finite difference method,[22] the method of lines,[23] the finite difference time-domain algorithm,[11] and the finite element method[24] have previously been successfully utilized in the analysis of optical waveguides. In this paper, the DLSPPW mode effective index, confinement, and propagation lengths are investigated in detail using the EIM, and the results are compared to and complemented with those obtained by making use of the finite element method (FEM).

This paper is organized as follows. In Sec. II, the EIM is presented and used in calculations of the DLSPPW mode effective index, propagation length, and confinement for different system parameters. After this, the FEM is introduced and employed in Sec. III for calculations of field distributions and vector plots in the DLSPPW cross section. The accuracy of the EIM is evaluated in Sec. IV by comparing the mode effective index, propagation length, and vertical and lateral field profiles calculated with the EIM and FEM. Finally, in Sec. V, we discuss the results obtained and offer our conclusions.

II. EFFECTIVE-INDEX CALCULATION

The analyzed straight waveguide structure is similar to that investigated experimentally[16] and represents a dielectric (e.g., polymer) ridge with refractive index n_2, thickness t, and width w placed on a metal (e.g., gold) film with thickness d and wavelength dependent refractive index n_3 [Fig. 1(a)]. The gold-polymer structure is enclosed by air with refractive index n_1 above and a semi-infinite dielectric layer with refractive index n_4 below, which represents a thick glass substrate usually used in experiments to support the gold film with polymer ridge structures.[16]

In the EIM, the two-dimensional (2D) cross section of the DLSPPW is considered and solved for guided modes by dealing consecutively with two one-dimensional (1D) waveguide geometries, which can be solved individually in a manner similar to that used for analyzing multilayer waveguide structures.[25–27] The key assumption made in the reduction of the problem is that the modes are linearly polarized and well above cutoff, i.e., with most of the power concentrated in the ridge subregion so that the field magnitudes in the four corner regions are small enough to be neglected. Whereas the EIM previously has been used to analyze dielectric ridge waveguides,[25–27] which does not differ geometrically from DLSPPWs, the very large and complex refractive index of the gold film at telecom wavelengths potentially changes the validity of the EIM. The conclusions made on the performance of the EIM in contemplation of dielectric ridge waveguides can thus not be directly adapted to EIM calculations of DLSPPW modes.

One can view the 2D waveguide structure [Fig. 1(a)] as being obtained by decreasing the width of the top polymer layer [Fig. 1(b)] to match that of the ridge. The first step in such an EIM approach (here denoted EIM-1 to distinguish it from another EIM approach introduced later) is thus to calculate the effective index N_{eff}^{*} of guided modes in a planar four-layer waveguide structure [Fig. 1(b)]. Each of the four layers is considered of infinite lateral extension in the x direction. Furthermore, the top (air) and bottom (dielectric) layers abutting the polymer and gold films are considered semi-infinite in the (depth) y direction, which implies that there are no reflections from external boundaries, only from the gold and polymer interfaces.

In the second step of the EIM-1 (when shrinking the polymer layer in width), N_{eff}^{*} is used in the calculation of the final mode effective index N_{eff} by contemplation of a three-layer waveguide structure with vertical interfaces [Fig. 1(c)]. As the modes of interest in this work are bound to the gold-

polymer interface, the effective index of a SPP propagating along the gold-air interface (n_{SPP}) is used outside the ridge subregion.

In the simulation results presented hereafter, an excitation wavelength $\lambda=1.55$ μm, a gold layer thickness $d=100$ nm, and refractive indexes $n_1=1$, $n_2=1.535$, $n_3=0.55+i11.5$,[28] and $n_4=1.6$ are used when calculating DLSPPW mode characteristics unless noted otherwise.

A. SPP guiding in the four-layer structure

The direction of SPP propagation is considered along the z axis (Fig. 1) and the electric field can then be written in the form

$$\mathbf{E} = \mathbf{E}_p(y)\exp[i(\omega t - \beta z)], \tag{1}$$

where $\mathbf{E}_p$ denotes the components of the electric field, e.g., being in the case of TM modes in the (y,z) plane. β is the complex propagation constant $\beta=\beta'-i\beta''$ which is related to the mode effective index according to $\beta'=k_0N_{eff}^*$ $=(2\pi/\lambda)N_{eff}^*$ and propagation length as $L^*=1/(2\beta'')$. It is instructive to consider the SPP dispersion relation of a metal-dielectric interface, which can be thought of as a limiting case of the considered configuration with the polymer film thickness t being either very small or very large. The corresponding SPP dispersion relation is given by[1]

$$\beta = k_0\sqrt{\frac{\epsilon_m\epsilon_d}{\epsilon_m+\epsilon_d}}, \tag{2}$$

with ϵ_m being the complex permittivity of the metal and ϵ_d being the permittivity of the dielectric.

When solving the four-layer planar geometry [Fig. 1(b)] for the effective index N_{eff}^* and propagation length L^* for various polymer film thicknesses, it is expected that, for very thin film layers, the fundamental mode becomes progressively close to a SPP propagating along the gold-air interface, i.e., $N_{eff}^*\rightarrow 1.0038$ and $L^*\rightarrow 339$ μm. Correspondingly, for very thick film layers, the results should approach those of a SPP at the gold-polymer interface, i.e., $N_{eff}^*\rightarrow 1.55$ and $L^*\rightarrow 92$ μm. In between these extremes, it is expected that the SPP mode effective index of the four-layer structure is monotonously decreasing with the film thickness, since an increasing part of the SPP field penetrates in the air above the polymer. Decreasing the film thickness, however, also has the effect of squeezing the field inside the polymer region, because optical fields tend to be confined in regions with higher refractive indexes. This implies that the field magnitude at the gold-polymer interface (and inside the gold) increases, resulting in greater absorption loss. One should therefore expect that the propagation length decreases with the film thickness until some point, where the field cannot be squeezed more into the polymer, reaching a minimum. Decreasing the film thickness further would result in a rapid increase in the field outside the polymer, and the propagation length would approach that of the SPP at the gold-air interface.

The results of the calculations performed by utilizing a multilayer waveguide program for solution of the four-layer structure confirm the expected behavior (Fig. 2). It should be mentioned that the accuracy of the multilayer waveguide program used was found to be very good by comparison with FEM calculations (with deviations being less than 0.1%) conducted for the same structure. In addition to the fundamental transverse magnetic (TM_0) mode, the second fundamental (TM_1) and the fundamental transverse electric (TE_0) modes are found. In the notation used, a TM mode refers to a SPP mode with dominating x component of the magnetic field and TE refers to transverse electric mode with dominating x component of the electric field. The fundamental TE_0 mode is included in order to evaluate the single-mode condition for DLSPPWs; however, it is not further analyzed as the second step in the EIM assumes SPP modes due to the use of n_{SPP}, thus making evaluation of TE modes erroneous. The cutoff thickness of the TM_1 mode is $t\sim 631$ nm and the TE_0 mode has cutoff at $t\sim 313$ nm, implying that below these thicknesses the corresponding modes do not exist. By controlling the polarization and limiting the film thickness (by 630 nm in our case), the single-mode guiding in such a four-layered structure is thereby achievable. Single-mode

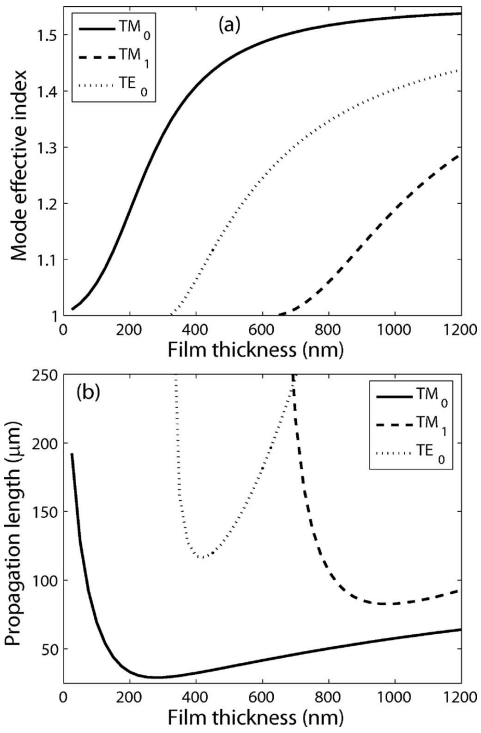

FIG. 2. Characteristics of modes supported by the four-layer structure presented in Fig. 1(b) and analyzed in the first step of the EIM-1. (a) The mode effective index and (b) the propagation length as a function of the film thickness for TM_0, TM_1, and TE_0 modes.

guiding allows one to avoid various mode dispersion and interference effects (usually unwanted) and is therefore preferential in photonic circuits. Conditions for the single-mode guiding in DLSPPWs are further considered in the following section.

B. Single-mode condition

The mode effective index of the DLSPPW [Fig. 1(a)] is found by utilizing the calculated effective index and propagation length of a multilayered structure (N_{eff}^{*} and L^{*}) and by taking into account the finite width of the ridge [Fig. 1(c)]. Although one can avoid the support of multiple modes of the multilayered structure [Fig. 1(b)] by limiting the ridge thickness to $t \lesssim 631$, care must be taken in the second step of the EIM-1 to avoid multimode guiding of the final structure. This is due to the possible appearance of TM_{01} modes, i.e., modes that have two peaks in the lateral profile. A condition for single-mode guiding of the DLSPPW is found by solving for the cutoff width of the TM_{01} mode, i.e., the minimum ridge width w which supports two TM modes. By designing ridges with widths below this cutoff width, single-mode guiding of the final waveguide structure is achievable. It is, however, apparent that the single-mode guiding still requires TM-polarized excitation in order to avoid excitation of TE modes.

It is seen that the waveguide structure is symmetric in the lateral direction [Fig. 1(c)]. The cutoff width for the TM_{01} mode can then be calculated by utilizing normalized waveguide parameters as follows:[29]

$$w = \frac{\pi}{k_0 \sqrt{(N_{eff}^{*})^2 - (n_{SPP})^2}}, \tag{3}$$

where n_{SPP} is the mode effective index of the SPP supported by the gold-air interface. The cutoff ridge width for the TM_{01} mode is thus dependent on the wavelength and ridge thickness t as N_{eff}^{*} depends on the thickness t. For small thicknesses, N_{eff}^{*} approaches n_{SPP} and the cutoff ridge width increases rapidly. For large thicknesses, N_{eff}^{*} approaches the mode effective index of the SPP at the gold-polymer interface, and the cutoff ridge width approaches a constant value of $w \sim 655$ nm.

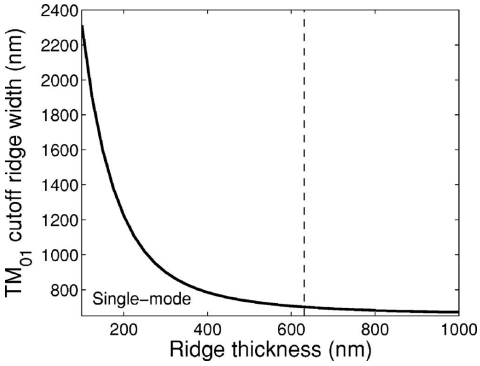

FIG. 3. Cutoff ridge width of the TM_{01} mode as a function of thickness. The vertical dashed line indicates the thickness where the TM_1 mode has cutoff.

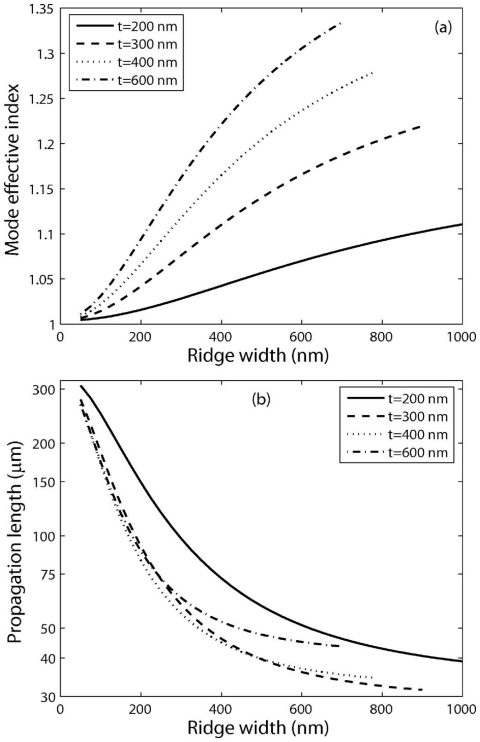

FIG. 4. The mode effective index and propagation length (logarithmic scale) as a function of ridge width for several different thicknesses as calculated with EIM-1. Each curve is ended at the cutoff width of the TM_{01} mode, i.e., where single-mode guiding ceases.

The cutoff ridge width of the TM_{01} mode was determined using Eq. (3) for different thicknesses by utilizing the calculated effective indexes N_{eff}^{*} (Fig. 3). It is apparent that the single-mode guiding in DLSPPWs is achieved in the parameter space below the (TM_{01}) cutoff width curve and to the left of the (TM_1) cutoff thickness line.

C. Fundamental mode characteristics

The mode effective indexes and propagation lengths of TM_{00} modes are found by solution of the three-layer structure [Fig. 1(c)] for different ridge dimensions (Fig. 4). For infinite ridge width, the structure and thus also the modes are identical to those of the four-layer structure [Fig. 1(b)], im-

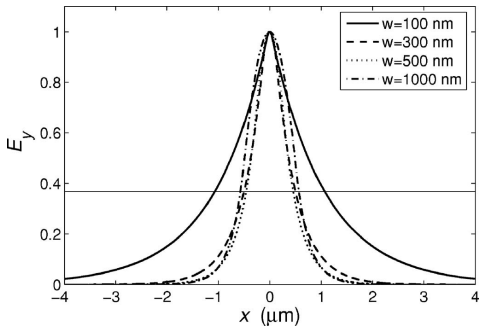

FIG. 5. The lateral field distribution of the main electric-field component for four widths w, all with $t=600$ nm. The thin horizontal line indicates the value $1/e$, and as the field profiles are scaled to a maximum value of 1, the mode width can be read from the intersection with this line. The calculations are performed with the EIM-1. The $w=1000$ nm waveguide is not single mode, but is included to illustrate that the mode width increases for wide ridges.

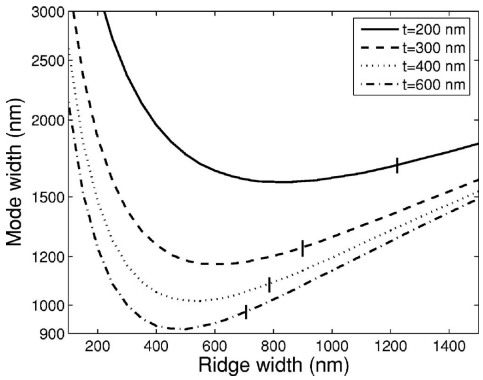

FIG. 6. The mode width (logarithmic scale) depicted versus the ridge width for four different values of ridge thickness t. The vertical lines crossing the curves mark the end of the single-mode regime. The calculations are performed by using the EIM-1.

plying that $N_{eff}\rightarrow N_{eff}^{*}$. As N_{eff}^{*} is increasing monotonously with thickness [Fig. 2(a)] so is N_{eff} [Fig. 4(a)]. A decrease in the ridge width decreases the field portion confined in the ridge region and the mode effective index therefore decreases. For very small ridge widths, the DLSPPW fundamental mode effective index N_{eff} approaches that of the SPP at the gold-air interface. Similar reasoning accounts for the propagation length of the mode, which increases when decreasing the ridge width and approaches the SPP propagation length at the gold-air interface [Fig. 4(b)]. The calculated propagation length dependence shows that a larger mode effective index (associated with a better mode confinement within the ridge) implies a shorter propagation length, in accordance with the general consideration. This, however, is strictly true only for constant-thickness ridge waveguides. For example, when comparing the length dependence for ridges with $t=600$ nm and $t=300$ nm, it is seen that the propagation length (of the DLSPPW fundamental mode) for the 600-nm-thick ridge waveguides is longer than that for 300-nm-thick ones once their widths are larger than 300 nm [Fig. 4(b)]. At the same time, the mode effective index for the 600-nm-thick ridge waveguides is larger than that for 300-nm-thick ones for all widths [Fig. 4(a)]. This feature is a consequence of the nonmonotone dependence of TM_0 propagation length [Fig. 2(b)], indicating also the possibility for optimization with respect to the confinement-loss trade-off.

D. Lateral mode field confinement

In the design of optical waveguides, the lateral mode field confinement is of great importance because a good confinement, i.e., a small mode width W, enables large bend angles $\theta\propto\lambda/W$ with acceptable bend losses, thereby minimizing the length of components $\ell\propto W/\theta$.[21] This trend in turn maximizes density of components $n\propto 1/(\ell W)=\lambda/W^3$ and, in addition, decreases the incurred propagation loss per component due to a decrease in the component length.

Previous results from contemplation of similar DLSPPW structures[15] illustrate that a large ridge curvature gives rise to a complete radiative loss of poorly confined SPP modes. This exemplifies the importance of well confined modes, and to accommodate this design parameter, the mode width of DLSPPWs of different dimensions is investigated in the following.

In order to find the mode width of the fundamental TM_{00} mode for different ridge dimensions, the field profiles of a lateral cross section are considered. The main electric-field component (E_y) of a lateral profile is considered for a 600-nm-thick ridge waveguide at four different widths (Fig. 5). Each profile has been normalized to a maximum value of 1 and the mode width is thus given as the width of the peak at a field value of $1/e$, represented by the thin horizontal line in the figure. The mode width is different for the four different thicknesses. It is very large for the 100-nm-wide ridge and seems to have a minimum around a ridge width of ~500 nm. This clearly illustrates that the field is squeezed into the ridge region when the width is decreased until a certain point, where the field no longer can be confined to the

TABLE I. The optimum ridge width regarding lateral field confinement along with the mode width, propagation length, and mode effective index for four different ridge thicknesses.

	t (nm)			
	200	300	400	600
w_{opt} (nm)	850	600	550	500
Mode width (nm)	1580	1165	1015	915
L (μm)	42	36	38	48
N_{eff}	1.10	1.17	1.22	1.27

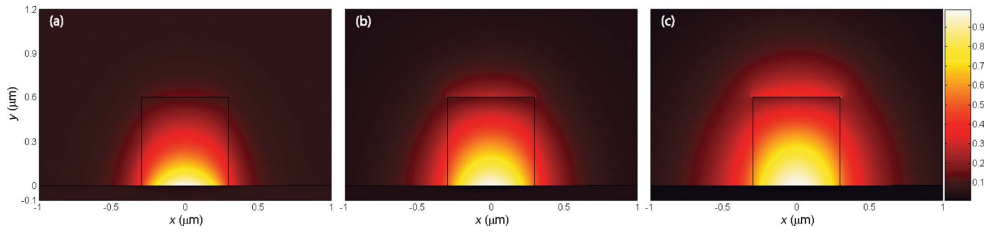

FIG. 7. (Color online) Field distribution plots of the magnitude of the vertical component of the electric field $|E_y|$ for ridge dimension $t=600$ nm, $w=600$ nm, calculated by application of the FEM. In all three plots, the fundamental TM_{00} mode is depicted. (a) shows the field for $\lambda=893$ nm ($n_3=0.21+i5.94$) where $N_{eff}=1.49$ and $L=16.1$ μm, (b) for $\lambda=1.22$ μm ($n_3=0.36+i8.60$) where $N_{eff}=1.39$ and $L=29.8$ μm, and (c) for $\lambda=1.55$ μm ($n_3=0.55+i11.5$) where $N_{eff}=1.29$ and $L=44.4$ μm (Ref. 28).

ridge. Then, it starts to spread out into the surrounding air where the decay length is larger, thereby decreasing the mode confinement. To find the optimum width, regarding the mode width, for different ridge thicknesses, additional calculations have been performed (Fig. 6). The results show the mode width versus the ridge width for several different thicknesses. There is a distinct minimum in all curves, indicating the optimum ridge width w_{opt} regarding the lateral mode field confinement. The results for the five shown thicknesses are summarized in Table I, where w_{opt} along with the mode widths are shown for each of the five t values. The results presented here (Fig. 6 and Table I) show that in order to achieve good lateral mode field confinement, one should construct a DLSPPW of large thickness and width of 400–500 nm, e.g., $t=600$ nm and $w=500$ nm. Larger thicknesses are desirable regarding mode confinement and propagation length; however, since such waveguides are not single mode, they are not considered in this work.

III. FINITE ELEMENT CALCULATIONS

When utilizing the FEM to analyze the DLSPPW structure [Fig. 1(a)], the mode effective index, propagation length, and the magnetic- and electric-field vectors in the cross section of the DLSPPW can be found. In addition to providing numerically determined N_{eff} and L values, this method thus enables evaluation of some of the approximations made in the EIM-1, e.g., regarding strictly vertical polarization in the cross section of the waveguide.

The FEM is a technique for numerical solution of partial differential equations or integral equations. In the method, the region of interest is subdivided into small segments, usually triangles, and the partial differential equation is replaced with a corresponding functional. Subsequently, a variational method is used to minimize the functional in order to obtain variational features in the algorithm.[30–32]

The approach taken in the application of the FEM in this work is solution of the electric-field components and the propagation constant β. By assuming fields on a time-harmonic form, the wave equation for the electric field is given as

$$\nabla \times \left(\frac{1}{\mu_r} \nabla \times \mathbf{E} \right) - k_0^2 \epsilon_r \mathbf{E} = \mathbf{0}, \tag{4}$$

where the relative permittivity ϵ_r in general is a complex position dependent tensor and the relative permeability μ_r in general is a position dependent tensor. The media contemplated in this paper are, however, considered homogeneous, nonmagnetic, and isotropic, implying that ϵ_r has a constant scalar value within each medium and that $\mu_r=1$. With SPP propagation in the z direction, i.e.,

$$\mathbf{E}(x,y,z,t) = \mathbf{E}(x,y)\exp[i(\omega t - \beta z)], \tag{5}$$

the wave equation [Eq. (4)] simplifies to

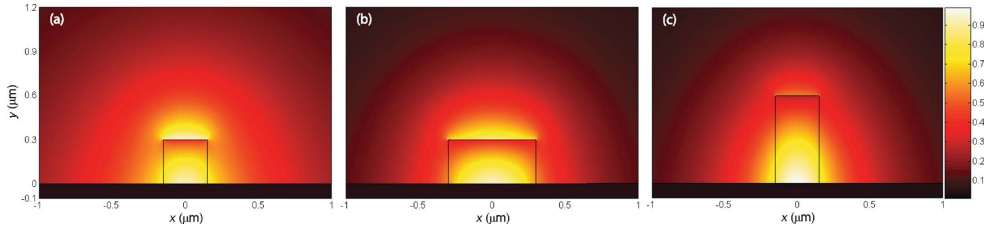

FIG. 8. (Color online) Field distribution plots of the magnitude of the vertical component of the electric field $|E_y|$ for different ridge dimensions. (a) shows $|E_y|$ for a $t=300$ nm, $w=300$ nm ridge where $N_{eff}=1.04$ and $L=68.7$ μm, (b) a $t=300$ nm, $w=600$ nm ridge where $N_{eff}=1.14$ and $L=37.0$ μm, and (c) a $t=600$ nm, $w=300$ nm ridge where $N_{eff}=1.13$ and $L=59.1$ μm.

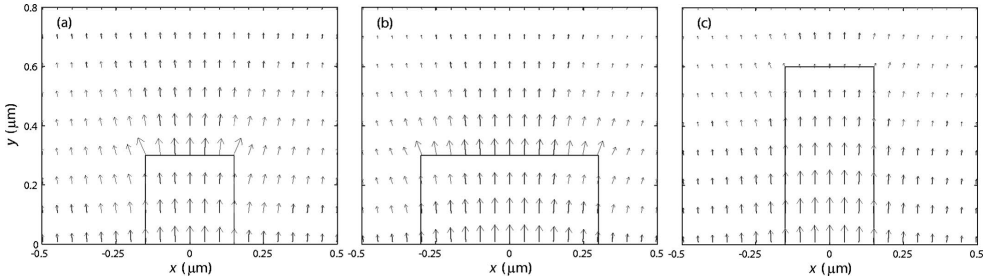

FIG. 9. Field vector plots of the electric field for different ridge dimensions. (a) shows $\mathbf{E}_t$ for a $t=300$ nm, $w=300$ nm ridge, (b) a $t=300$ nm, $w=600$ nm ridge, and (c) a $t=600$ nm, $w=300$ nm ridge. The field vectors are scaled arbitrarily.

$$\nabla_t^2 \mathbf{E} + (\epsilon_r k_0^2 - \beta^2)\mathbf{E} = \mathbf{0}, \tag{6}$$

where ∇_t^2 denotes the part of the Laplacian related to the transverse components (x,y). This is the partial differential equation from which a corresponding functional is constructed and solved for β, E_x, E_y, and E_z.

The boundary condition used at the exterior boundary (edge of computational window) is that of a perfect electric conductor,

$$\hat{\mathbf{n}} \times \mathbf{E} = \mathbf{0}, \tag{7}$$

which implies that the tangential components of the electric field are set to zero at the exterior boundary. The boundary conditions which must be fulfilled at the interior boundaries, i.e., at the interfaces between two media, are the continuity of the tangential components of the electric and magnetic fields and the continuity of the normal components of the electric and magnetic flux densities,

$$\hat{\mathbf{n}} \times (\mathbf{E}_1 - \mathbf{E}_2) = \mathbf{0}, \tag{8}$$

$$\hat{\mathbf{n}} \times (\mathbf{H}_1 - \mathbf{H}_2) = \mathbf{0}, \tag{9}$$

$$\hat{\mathbf{n}} \cdot (\mathbf{D}_1 - \mathbf{D}_2) = 0, \tag{10}$$

$$\hat{\mathbf{n}} \cdot (\mathbf{B}_1 - \mathbf{B}_2) = 0, \tag{11}$$

where it has been assumed that the surface charge density ρ_s and surface current density $\mathbf{J}_s$ are zero.

In the following two sections, field contour plots and field vector plots calculated by application of the FEM are treated, and in Sec. IV the calculated mode effective indexes and propagation lengths are compared to those found by means of the EIM. All FEM calculations in this work are performed by utilizing COMSOL MULTIPHYSICS 3.3.

A. Mode field cross-section distributions

The dependence of the field distribution of the y component of the electric field, the mode effective index, and the propagation length on SPP excitation wavelength and ridge dimensions is investigated. The field distribution of the fundamental TM_{00} mode of a DLSPPW is calculated for three different excitation wavelengths (Fig. 7). The dimension of the considered DLSPPW is $t=600$ nm, $w=600$ nm, and the results are shown for free-space excitation wavelengths of 893 nm, 1.22 μm, and 1.55 μm. As expected from the previous discussion, the field is strongly confined to the gold-polymer interface inside the ridge, indicating that the mode indeed is a DLSPPW mode, which is furthermore confirmed by the exponential decay into both the gold and polymer ridge regions (shown explicitly in the vertical field profiles presented in Sec. IV). The reasons for the nonevident field in the gold film in the field distribution plots are the conservation of the normal component of the electric flux density along with a large change in dielectric constant at the gold-polymer interface and the short penetration depth in the gold film. It is apparent that a shorter wavelength implies better confinement, as the ridge is optically larger for shorter wavelengths. Furthermore, a larger wavelength results in less loss and thus longer propagation lengths, in accordance with the

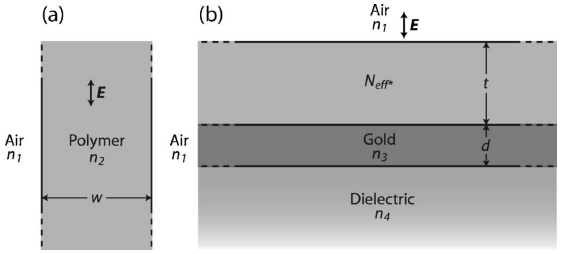

FIG. 10. Cross-sectional view of the waveguide structure considered (a) in the first step of the EIM-2 and (b) in the second step of the EIM-2. In both cases, the polarization is strictly vertical, and the layers are considered of infinite vertical and horizontal extents, respectively.

TABLE II. The mode effective indexes N_{eff} and propagation lengths L of the DLSPPWs calculated by means of the FEM, the EIM-1, and the EIM-2. The ridge thickness is constant at $t=600$ nm and the width varies from $w=200$ nm to $w=800$ nm.

	Ridge width (nm)						
	200	300	400	500	600	700	800
Mode index FEM	1.064	1.133	1.198	1.250	1.291	1.323	1.348
Mode index EIM-1	1.094	1.162	1.221	1.268	1.305	1.334	1.357
Mode index EIM-2	1.075	1.143	1.205	1.255	1.294	1.325	1.349
Prop. length (μm) FEM	81.3	59.1	50.1	46.4	44.4	42.8	42.2
Prop. length (μm) EIM-1	89.2	63.0	52.6	47.8	45.2	43.8	42.9
Prop. length (μm) EIM-2	104	78.6	66.3	59.4	55.1	52.2	50.2

general understanding. Due to the conservation of the normal component of the electric flux density at the interfaces [Eq. (10)], a discontinuous change in the electric field is expected at the lateral boundaries of the ridge. This discontinuity is very evident for the gold-polymer interface, but can also be observed for the air-polymer interface, however, less pronounced due to the smaller difference in permittivity.

The dependence of the field distribution of the vertical component of the electric field on ridge dimensions is calculated for an excitation wavelength of 1.55 μm (Fig. 8). Four different waveguide structures are considered in total [three in Fig. 8 and one in Fig. 7(c)]. The field distributions in a $t=300$ nm, $w=300$ nm ridge [Fig. 8(a)] and a $t=300$ nm, $w=600$ nm ridge [Fig. 8(b)] show that for small ridge thicknesses a large part of the field is distributed on top of the ridge waveguide, which is undesirable when designing optical components such as bends and splitters due to large radiative losses. Both $t=300$ nm waveguide structures also show a poor lateral confinement of the electric field in comparison with the $t=600$ nm ridge waveguides, which is in accordance with the EIM-1 results. The ridge dimensions which show the best confinement both laterally and vertically are clearly the largest ($t=600$ nm, $w=600$ nm [Fig. 7(c)]).

In the EIM, the field in the corner regions is disregarded, and for large ridges this appears to be a good approximation. Here, the field is mainly confined to the ridge and, in particular, to the gold-polymer interface. For small ridge dimensions, however, this approximation leads to an error, as a relatively large part of the field is concentrated in the two upper corner regions. The effect this has on the calculated mode effective indexes and propagation lengths is investigated in Sec. IV.

B. Electric-field orientation

In order to investigate the validity of the approximation made in the EIM of strictly vertical polarization, the field vectors of the electric field in the cross section of the DLSPPW, $\mathbf{E}_t$, are calculated for three different ridge dimensions by utilizing the FEM (Fig. 9). The field vectors of the small ridge ($t=300$ nm, $w=300$ nm [Fig. 9(a)]) show a quite large deviation from strictly vertical polarization. This is especially pronounced around the corners in the air surrounding the ridge, but it is evident in the entire plot except right through the middle of the ridge due to the symmetry of the ridge structure. The plot of the field vectors in the $t=300$ nm, $w=600$ nm structure [Fig. 9(b)] also shows nonvertical electric-field vectors, but since a larger part of the field is confined to the ridge, the deviation from vertical polarization is smaller. The $t=600$ nm, $w=300$ nm ridge structure [Fig. 9(c)] also shows less nonvertical polarization than

TABLE III. The mode effective indexes and propagation lengths of the DLSPPWs calculated by means of the FEM, the EIM-1, and the EIM-2. The ridge width is constant at $w=500$ nm and the thickness is varied.

	Ridge thickness (nm)						
	200	300	400	500	600	700	800
Mode index FEM	1.041	1.111	1.176	1.221	1.250	1.269	1.282
Mode index EIM-1	1.057	1.140	1.205	1.244	1.268	1.284	1.294
Mode index EIM-2	1.089	1.149	1.198	1.232	1.255	1.270	1.282
Prop. length (μm) FEM	66.0	41.7	39.5	42.2	46.4	50.4	54.8
Prop. length (μm) EIM-1	59.1	39.8	39.9	43.5	47.8	52.2	56.4
Prop. length (μm) EIM-2	61.9	51.3	51.2	54.6	59.4	64.5	69.6

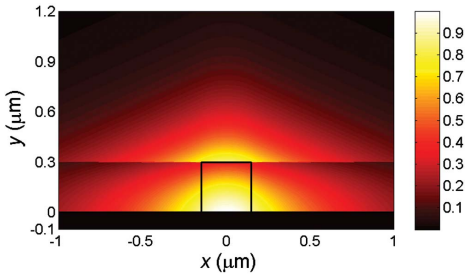

FIG. 11. (Color online) Field distribution of the magnitude of the vertical component of the electric field obtained by combining lateral and vertical field profiles from the EIM-1 for a $t=300$ nm, $w=300$ nm ridge.

the smaller structure, but there is still deviation evident in the corner regions outside the ridge. The variance from vertical polarization will cause discrepancy in the calculated mode effective indexes and propagation lengths of the two methods. The effect of this is investigated further in the following, where the accuracy of another EIM is also evaluated.

IV. COMPARISON OF SIMULATION METHODS

In order to investigate the validity of the EIM-1 results, the calculated mode effective indexes and propagation lengths are compared to those calculated by means of the FEM. Furthermore, the results of another effective-index approach (EIM-2) are compared to the FEM and EIM-1 results. The 2D waveguide geometry considered in the EIM-2 is the same as that of the EIM-1 [Fig. 1(a)]; however, a different approach is taken in the reduction of the 2D geometry to two 1D waveguide structures that can be dealt with consecutively (Fig. 10). First, an infinitely tall ridge is considered, i.e., an air-polymer-air layer with infinitely extending vertical boundaries [Fig. 10(a)]. A ridge width dependent effective index N_{eff}^{*} of this structure is calculated by assuming polarization parallel to the interfaces. One can then view the appearance of a DLSPPW by truncating the air-polymer-air structure vertically and surrounding it by air above and a gold-dielectric structure below. The effective index N_{eff}^{*} found by solution of the three-layer vertical structure is thus used in the solution of a four-layer planar waveguide structure, where infinite horizontal extension of the layers is assumed [Fig. 10(b)].

A. Mode effective index and propagation loss

The mode effective indexes and propagation lengths of DLSPPWs, calculated by means of the three different methods, are presented in Table II for a constant ridge thickness of $t=600$ nm. The table presents the results of seven different waveguide dimensions, $w=200$ nm to $w=800$ nm. Note that the $t=600$ nm, $w=800$ nm waveguide is not single mode; however, it is included for illustration purposes. The results for constant ridge thickness show some general tendencies. Firstly, the mode effective indexes calculated by means of the EIM-1 and the EIM-2 are larger than those calculated by means of the FEM. The maximum deviation from the FEM results is, however, less than 3%. Secondly, the propagation lengths calculated by means of the EIM-1 and the EIM-2 are longer than those calculated by application of the FEM. The maximum deviation from the FEM results is 10% for the EIM-1 and 33% for the EIM-2. Thirdly, the deviations of the EIM-1 and EIM-2 from the FEM results decrease with increasing ridge width. Lastly, the results show that the EIM-2 is more accurate than the EIM-1 regarding the mode effective index, but results in much larger error in the calculated propagation lengths.

In Table III, the mode effective indexes and propagation lengths calculated by means of the three methods are presented for ridges with constant width $w=500$ nm and varying thickness from $t=200$ nm to $t=800$ nm. As before, some of

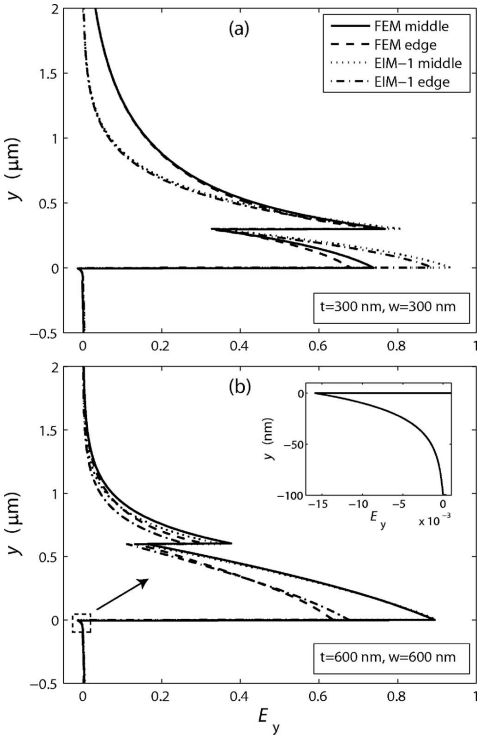

FIG. 12. Vertical profiles of the vertical component of the electric field E_y calculated by utilizing the EIM-1 and the FEM. The edge profiles are taken 50 nm from the vertical edge of the ridge. The field profiles are shown for a $t=300$ nm, $w=300$ nm ridge where $N_{eff,\mathrm{FEM}}=1.04$, $L_{\mathrm{FEM}}=68.7$ μm, $N_{eff,\mathrm{EIM\text{-}1}}=1.08$, $L_{\mathrm{EIM\text{-}1}}=59.7$ μm and for a $t=600$ nm, $w=600$ nm ridge where $N_{eff,\mathrm{FEM}}=1.29$, $L_{\mathrm{FEM}}=44.4$ μm, $N_{eff,\mathrm{EIM\text{-}1}}=1.31$, $L_{\mathrm{EIM\text{-}1}}=45.2$ μm. The inset is a zoom of the EIM-1 middle profile in the metal film.

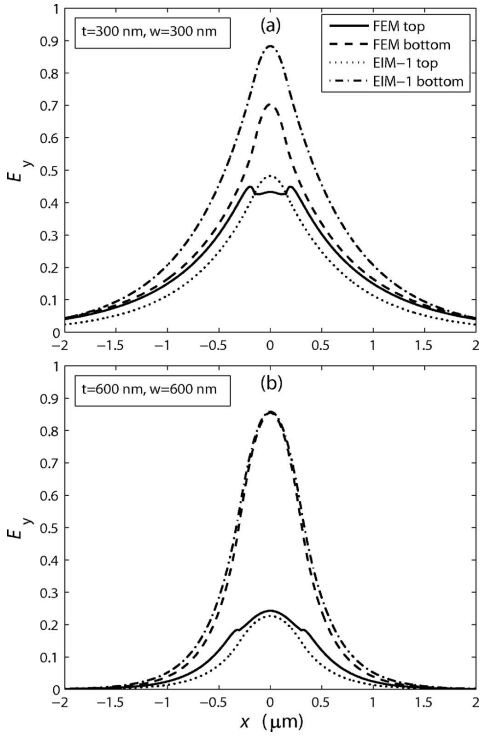

FIG. 13. Lateral profiles of the vertical component of the electric field calculated by utilizing the EIM-1 and the FEM. The bottom profiles are taken 50 nm from the gold-polymer interface and the top profiles are taken 50 nm from the top of the ridge. The field profiles are shown for a $t=300$ nm, $w=300$ nm and for a $t=600$ nm, $w=600$ nm ridge SPP waveguide.

the waveguides are not single mode; however, they are included for illustration purposes. The results of the constant ridge width calculations also show some general tendencies; however, in this case the EIM-2 results are not unambiguously closer to the FEM results regarding N_{eff} and the EIM-1 results are not unambiguously closer to the FEM results regarding the propagation length, as was the case for the constant-thickness waveguide. It is interesting to note that at small ridge thicknesses ($t \lesssim 350$ nm), the accuracy of the EIM-2 regarding N_{eff} is largely affected. This is found to inherit from the approximation that the polymer layer extends infinitely in the vertical direction [Fig. 10(a)], which is a poor approximation for small ridge thicknesses. For larger thicknesses, however, the EIM-2 shows superior results regarding N_{eff} and the EIM-1 is superior regarding the calculation of propagation loss.

The reason for the overestimation of the propagation constant in the EIM can be explained according to previous analysis on dielectric ridge waveguides, where it is found that overestimation occurs when the normalized frequency is large.[25–27] That the accuracy of the propagation length is superior for the EIM-1 is a consequence of the inclusion of the SPP nature of the modes in both steps, whereas the SPP nature of the mode field outside the polymer region, i.e., at the gold-air interface, is not properly accounted for in the EIM-2. This is supported by the following reasoning. An increase in the width of the ridge ($w=300 \rightarrow w=600$ nm) leads to a decrease of the electric field at the gold-air interface outside the ridge [Figs. 8(a) and 8(b)]. Increasing the thickness of the ridge ($t=300 \rightarrow t=600$ nm) does not, however, largely affect the electric field at the interface outside the ridge [Figs. 8(a) and 8(c)]. This implies that if the above explanation of the longer propagation length calculated by the EIM-2 is correct, an increase in ridge width should decrease the error in propagation length of the EIM-2, whereas an increase in thickness should not affect the error largely. This is confirmed in the results presented in Tables II and III as an increase in width ($w=400 \rightarrow w=800$) nm reduces the error from 32% to 19%, whereas an increase in thickness ($t=400 \rightarrow t=800$) nm only reduces the error from 30% to 27%.

The results show that in general the total deviation is larger for the EIM-2 as the error in propagation length is quite large for this method. The error in N_{eff} and L of the EIM-1 for larger ridge dimensions is, however, less than 3% and thus the validity of the EIM-1 proves to be justified except for contemplation of guided SPP modes in very small ridges.

B. Vertical and lateral field distributions

While the accuracy of the mode effective index and propagation length is important for analyzing mode propagation in straight waveguides, the accuracy of the field distribution is of great practical interest in the realization of optical components such as bends, splitters, and directional couplers, because the bend and coupling losses depend strongly on the field distribution (mode confinement) in the cross section of the waveguide. In the EIM-1, field distributions are obtained by taking the product of the lateral and vertical field distributions as calculated in the first and second steps of the EIM-1, respectively, i.e., $E_{\text{EIM-1}}=\psi(x)\phi(y)$ (Fig. 11). Apparent deviations from the FEM result [$E_{\text{FEM}}=E(x,y)$] [Fig. 8(a)] are evident for the $t=300$ nm, $w=300$ nm ridge, especially the discontinuity of the field at $y=300$ nm that accentuates the errors introduced in the EIM-1 by disregarding the corner regions. It is chosen to compare vertical and lateral field profiles obtained from the EIM-1 and FEM field plots to investigate the accuracy of the calculated field distributions further. The field distributions from the EIM-1 and the FEM are normalized so that the surface integrals of E_y^2 in the cross section are equal.

Vertical field profiles taken through the middle of the ridge and 50 nm from the edge of the ridge are found for a $t=300$ nm, $w=300$ nm ridge and a $t=600$ nm, $w=600$ nm ridge (Fig. 12). Lateral field profiles taken 50 nm from the top and 50 nm from the bottom of the ridge are found for the same ridge dimensions (Fig. 13). The field profiles of the

smaller waveguide show that the discrepancy between the two methods is significant in regard to the field distribution. The results of the EIM-1 illustrate that the field is noticeably larger at the metal surface, implying better vertical confinement, but also introducing larger Ohmic losses. The field profiles of the larger structure show a close correlation between the EIM-1 and FEM distributions, implying nearly identical mode confinement. However, whereas the bottom lateral profiles all are Gaussian in shape, the top lateral profiles of the FEM show irregularities at the ridge edges, which are found to inherit from the strong confinement of the electric field around the 90° corners of the ridge. In addition, the squeezing of the field into the ridge and the nonvertical components of the electric field in the smaller structure [Fig. 9(a)] makes these irregularities more apparent there [Fig. 13(a)]. The inset in Fig. 12(b) further confirms that the modes indeed are DLSPPW modes, as the field is shown to decrease exponentially into the metal film.

V. DISCUSSION AND CONCLUSIONS

The characteristics of DLSPPWs have been considered in detail by making use of different simulation methods, i.e., the EIM and the FEM. The validity of two different EI approaches has been evaluated by comparing the computed mode effective indexes, propagation lengths, and vertical and lateral field profiles to those found by means of the FEM. As expected, the EIM results showed noticeable deviations from the FEM results when treating weakly bound DLSPPW modes, whereas for the modes being far from cutoff the EIM was found reasonably accurate. The EIM, in which the DLSPPW was first considered as a planar multilayered waveguide before correcting for the finite width of the ridge (EIM-1), has been proved the most accurate in the whole range, as the other approach (EIM-2) failed to properly account for the field magnitude at the gold-air interface outside the ridge. By analyzing electric-field distributions in the DLSPPW cross sections calculated with the FEM, it has been found that the EIM inaccuracy when treating weakly bound modes inherits from not accounting for the field magnitude in the corner regions. Furthermore, the FEM field vector plots for different DLSPPWs showed that the assumption of linear (vertical) polarization in the EIM introduces an error, which is quite large for close to cutoff waveguides.

The DLSPPW mode effective index, confinement, and propagation length were calculated at the telecom wavelength $\lambda=1.55$ μm for different widths and thicknesses of a polymer ridge placed on a gold film surface. The condition for single-mode guiding has been investigated (using the EIM), and it has been found that single-mode DLSPPW guiding can be realized for ridge thicknesses smaller than ~630 nm and widths below ~655 nm (when decreasing the ridge thickness, the ridge width suitable for single-mode guiding increases). It has also been established that, in contrast to the usual trade-off, the DLSPPW mode lateral confinement can be improved simultaneously with the increase in the mode propagation length by choosing the appropriate ridge thickness [cf. Figs. 4(b) and 6]. In general, for each ridge thickness, the ridge width can be optimized with respect to the mode lateral confinement (Fig. 6). This optimum ridge width ranges from 850 to 500 nm for the thicknesses considered ($t=200$ nm to $t=600$ nm), where a larger ridge thickness implies a smaller mode width. It has thus been found favorable to have as thick a dielectric ridge waveguide as possible allowed by the single-mode condition, both regarding the mode confinement and propagation loss. For telecom wavelengths ($\lambda=1.55$ μm), the EIM calculations showed that a ridge having the thickness of 600 nm and the width of 500 nm would support a DLSPPW mode with the mode width $W=915$ nm, implying the subwavelength confinement (inside the ridge), and the propagation length $L=48$ μm, which is still relatively long. We believe that the presented results improve our understanding of the main features of SPP guiding in DLSPPW structures as well as provide useful guidelines for the design of DLSPPW-based photonic components. We conduct further investigations in this area.

ACKNOWLEDGMENTS

The authors thank Thomas Søndergaard for his help in developing a multilayer waveguide program used in this work and acknowledge the support of the PLASMOCOM project (EC FP6 IST 034754 STREP).

*Electronic address: holmgaard@physics.aau.dk

[1] H. Raether, *Surface Plasmons on Smooth and Rough Surfaces and on Gratings*, 1st ed. (Springer-Verlag, Berlin, 1988).
[2] W. L. Barnes, A. Dereux, and T. W. Ebbesen, Nature (London) **424**, 824 (2003).
[3] J. Takahara, S. Yamagishi, H. Taki, A. Morimoto, and T. Kobayashi, Opt. Lett. **22**, 475 (1997).
[4] M. Quinten, A. Leitner, J. R. Krenn, and F. R. Aussenegg, Opt. Lett. **23**, 1331 (1998).
[5] S. A. Maier, P. G. Kik, H. A. Atwater, S. Meltzer, E. Harel, B. E. Koel, and A. A. G. Requicha, Nat. Mater. **2**, 229 (2003).
[6] R. Zia, M. D. Selker, and M. L. Brongersma, Phys. Rev. B **71**, 165431 (2005).
[7] S. I. Bozhevolnyi, J. Erland, K. Leosson, P. M. W. Skovgaard, and J. M. Hvam, Phys. Rev. Lett. **86**, 3008 (2001).
[8] K. Tanaka and M. Tanaka, Appl. Phys. Lett. **82**, 1158 (2003).
[9] B. Wang and G. P. Wang, Appl. Phys. Lett. **85**, 3599 (2004).
[10] I. V. Novikov and A. A. Maradudin, Phys. Rev. B **66**, 035403 (2002).
[11] D. K. Gramotnev and D. F. P. Pile, Appl. Phys. Lett. **85**, 6323 (2004).
[12] S. I. Bozhevolnyi, V. S. Volkov, E. Devaux, and T. W. Ebbesen, Phys. Rev. Lett. **95**, 046802 (2005).
[13] S. I. Bozhevolnyi, V. S. Volkov, E. Devaux, J.-Y. Laluet, and T. W. Ebbesen, Nature (London) **440**, 508 (2006).
[14] C. Manolatou, S. G. Johnson, S. Fan, P. R. Villeneuve, H. A.

Haus, and J. D. Joannopoulos, J. Lightwave Technol. **17**, 1682 (1999).
[15] B. Steinberger, A. Hohenau, D. Ditlbacher, A. L. Stepanov, A. Drezet, F. R. Aussenegg, A. Leitner, and J. R. Krenn, Appl. Phys. Lett. **88**, 094104 (2006).
[16] C. Reinhardt, S. Passinger, B. N. Chichkov, C. Marquart, I. P. Radko, and S. I. Bozhevolnyi, Opt. Lett. **31**, 1307 (2006).
[17] A. Hohenau, J. R. Krenn, A. L. Stepanov, A. Drezet, H. Ditlbacher, B. Steinberger, A. Leitner, and F. R. Aussenegg, Opt. Lett. **30**, 893 (2005).
[18] A. B. Buckman, *Guided-Wave Photonics*, 1st ed. (Saunders College Publishing, New York, 1992).
[19] H. Kogelnik, *Integrated Optics* (Springer-Verlag, Berlin, 1979).
[20] A. Boltasseva, T. Nikolajsen, K. Leosson, K. Kjaer, M. S. Larsen, and S. I. Bozhevolnyi, J. Lightwave Technol. **23**, 413 (2005).
[21] S. I. Bozhevolnyi, Opt. Express **14**, 9467 (2006).
[22] S. J. Al-Bader, IEEE J. Quantum Electron. **40**, 325 (2004).
[23] P. Berini, Phys. Rev. B **61**, 10484 (2000).
[24] M. P. Nezhad, K. Tetz, and Y. Fainman, Opt. Express **12**, 4072 (2004).
[25] G. B. Hocker and W. K. Burns, Appl. Opt. **16**, 113 (1977).
[26] A. Kumar, D. F. Clark, and B. Culshaw, Opt. Lett. **13**, 1129 (1988).
[27] K. S. Chiang, Opt. Lett. **16**, 714 (1991).
[28] E. D. Palik, *Handbook of Optical Constants of Solids*, 1st ed. (Academic, New York, 1985).
[29] H. Kogelnik and V. Ramaswamy, Appl. Opt. **13**, 1857 (1974).
[30] J. Jin, *The Finite Element Method in Electromagnetics*, 2nd ed. (Wiley, New York, 2002).
[31] T. Itoh, *Numerical Techniques for Microwave and Millimeter-Wave Passive Structures*, 1st ed. (Wiley, New York, 1989).
[32] R. D. Cook, D. S. Malkus, M. E. Plesha, and R. J. Witt, *Concepts and Applications of Finite Element Analysis*, 4th ed. (Wiley, New York, 2002).

Appendix B

Appl. Phys. Lett. **92**, 2008

T. Holmgaard, S. I. Bozhevolnyi, L. Markey, and A. Dereux, *"Dielectric-loaded surface plasmon-polariton waveguides at telecommunication wavelengths: Excitation and characterization"*, Appl. Phys. Lett. **92**, 011124 (2008).

Dielectric-loaded surface plasmon-polariton waveguides at telecommunication wavelengths: Excitation and characterization

Tobias Holmgaard[a] and Sergey I. Bozhevolnyi
Department of Physics and Nanotechnology, Aalborg University, Skjernvej 4A, DK-9220 Aalborg Øst, Denmark

Laurent Markey and Alain Dereux
Institut Carnot de Bourgogne, UMR 5209 CNRS-Université de Bourgogne, 9 Av. A. Savary, BP 47 870, F-21078 Dijon Cedex, France

(Received 17 October 2007; accepted 28 November 2007; published online 9 January 2008)

The excitation and propagation of strongly confined surface plasmon-polariton (SPP) waveguide modes, supported by 500-nm-wide and 550-nm-high dielectric ridges fabricated on smooth gold films, are investigated at telecommunication wavelengths using a scanning near-field optical microscope. Different tapering structures for coupling of SPPs, excited at bare gold surfaces, into dielectric-loaded SPP waveguide (DLSPPW) modes are considered. The DLSPPW mode confinement and propagation loss are characterized. The DLSPPW mode propagation along an S bend having the smallest curvature radius of 2.48 μm is shown, demonstrating the potential of DLSPPW technology for the realization of high-density photonic integrated circuits. © *2008 American Institute of Physics*. [DOI: 10.1063/1.2825588]

Ever increasing demands for high-density photonic integrated circuits impel the search for waveguide configurations ensuring strong (lateral) mode field confinement, which is a prerequisite for realizing efficient and compact bends, splitters, and other waveguide components. For this reason, surface plasmon polaritons (SPPs) have attracted great interest in recent years.[1] SPPs are surface electromagnetic modes propagating along a metal-dielectric interface. They feature a maximum of the electric field at the interface and decay exponentially away from it.[2] A variety of SPP waveguide structures such as two dimensional SPP band gaps,[3] metal stripes,[4–6] and V grooves in a metal surface[7–9] have been proposed and investigated. An alternative and technologically simple strategy for achieving tight SPP mode confinement exploits the dependence of the SPP propagation constant on the refractive index of the dielectric at the metal-dielectric interface by depositing dielectric ridges on the metal surface. The resulting configuration, known as dielectric-loaded SPP waveguides (DLSPPWs), has been demonstrated experimentally at the free space wavelengths $\lambda=800$ nm (Refs. 10 and 11) and $\lambda=1520$ nm.[12] Numerical analysis of DLSPPWs at telecommunication wavelengths[13,14] showed prospects for obtaining very low radiation losses at compact bends and splitters provided that the ridges used are sufficiently high and narrow to ensure both large index contrast and strong field confinement in the single-mode propagation. In the present work, highly confined DLSPPW modes are demonstrated experimentally by near-field optical characterization of straight DLSPPW ridges and S bends at telecommunication wavelengths.

The waveguide dimensions, i.e., ridge height and width, are deduced by simultaneously considering mode confinement and propagation loss, while retaining the demand of single mode DLSPPWs. It is advantageous to choose a ridge as high as allowed by the single mode condition, as both lateral confinement and propagation length increases with ridge height (true only for ridges higher than $\sim$300 nm).[13] Decreasing the ridge width initially has the effect of squeezing the field laterally, thereby achieving better mode confinement. However, at a certain width the field can no longer be confined to the ridge and spreads out into the surrounding air. At telecommunication wavelengths, these considerations led to the determined optimum ridge height $h=600$ nm and width $w=500$ nm.[13]

The investigated sample consists of poly-methylmethacrylate (PMMA) ridges ($n_r=1.493$) deposited on a 50-nm-thick gold film by utilizing deep ultraviolet lithography. A thin glass substrate supports the metal film and the dielectric waveguides.

A funnel structure has been designed and realized in order to efficiently couple the SPPs excited at the gold-air interface by total internal reflection into bound DLSPPW modes. Moreover, close to the waveguide, this tapering structure may screen the propagation of the incident gold-air interface SPPs. Four tapering dimensions have been realized in order to determine the optimum structure for coupling SPPs into DLSPPW modes [Fig. 1(a)]. In the four designs, the initial funnel width is kept constant (10 μm) and the length is varied from 10 to 25 μm by steps of 5 μm, thereby varying funnel angles. The width of the fabricated waveguides has been investigated by scanning electron microscopy (SEM) and found to be $w\sim500$ nm [Fig. 1(b)]. An atomic force microscope (AFM) has determined the height of the ridges to be $h\sim550$ nm [Figs. 1(c) and 1(d)]. The measured waveguide characteristics are in good agreement with the targeted optimum values. Furthermore, the dielectric waveguides are generally found to be of high quality with only very small variations in width and height.

To characterize DLSPPW components at telecommunication wavelengths, the experimental setup consists of a scanning near-field optical microscope (SNOM) where SPPs are excited at the gold-air interface in the Kretschmann-Raether configuration.[2] Once the sample is placed in the SNOM setup, an immersion oil matches the index between

[a]Electronic mail: holmgaard@nano.aau.dk.

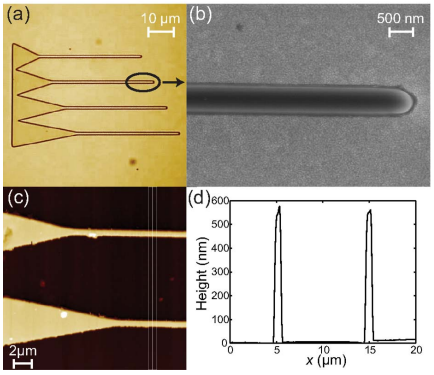

FIG. 1. (Color online) (a) Microscope image of a block with four waveguides with in coupling funnel of different dimensions. (b) SEM image of the termination region of a straight waveguide, revealing a waveguide width of ~500 nm. (c) AFM image of the tapering region and (d) cross section of the AFM image revealing a waveguide height of ~550 nm.

the prism and the sample substrate. Using a lensed fiber, an incident Gaussian beam is focused on the gold film to a spot size of ~15 μm. The adjustment of the incident angle is performed by minimizing the reflected signal recorded with a charge-coupled device camera. An uncoated etched fiber tip is scanned over the sample by means of a feedback loop, yielding both topographic and near-field optical images of the investigated area. SPPs are excited outside the funnel at the gold-air interface and propagate from top to bottom in the reported near-field images.

The DLSPPW block with four tapering designs [Fig. 1(a)] has been investigated in order to determine the in-coupling efficiency of the different funnel dimensions [Fig. 2]. The funnels show increasing in-coupling efficiency with decreasing funnel angle, and the scattering of SPPs at the tapering-waveguide transition is clearly weaker in the 10 $\times$25 μm funnel [Fig. 2(a)] as compared to the 10$\times$10 μm funnel [Fig. 2(d)]. Thus, the longest and smoothest transition

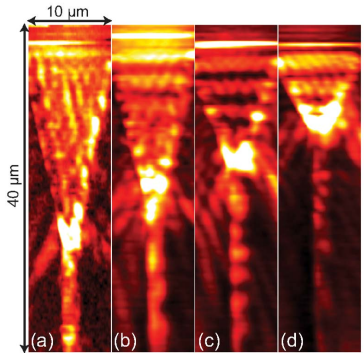

FIG. 2. (Color online) Near-field optical images of the tapering region for four different dimensions of the funnel in coupling at the free space excitation wavelength λ=1520 nm. (a) 10$\times$25 μm funnel, (b) 10$\times$20 μm funnel, (c) 10$\times$15 μm funnel, and (d) 10$\times$10 μm funnel.

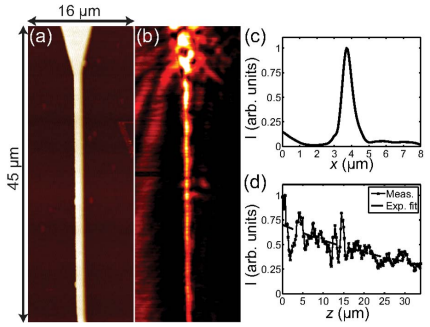

FIG. 3. (Color online) Near-field optical measurements of a straight DLSPPW with a 10$\times$25 μm in coupling funnel. [(a) and (b)] Topographical and near-field optical signal images, respectively, for λ=1550 nm. (c) Cross section of the optical image perpendicular to the waveguide and (d) averaged profile of the near-field optical signal recorded along the waveguide.

from tapering region to waveguide is found to be desirable.

Straight DLSPPWs have been investigated at the telecommunication wavelength λ=1550 nm [Fig. 3]. The topography recorded with the fiber tip shows a smooth transition from the tapering region to the waveguide region, revealing only very small irregularities in the waveguide structure [Fig. 3(a)]. The image of the recorded near-field optical signal shows a highly confined DLSPPW mode [Fig. 3(b)]. The cross section of the optical signal perpendicular to the waveguide yields a full width at half maximum of ~706 nm. Furthermore, it confirms that the tapering region, in addition to launching DLSPPW modes, also reduces SPP propagation along the gold-air interface close to the waveguide [Fig. 3(c)]. An averaged profile of the optical signal taken along the ridge reveals a 1e propagation length of ~39 μm, determined from an exponential fit to the profile [Fig. 3(d)]. This value is lower than the propagation length of 50 μm, expected from the numerical results,[13] however, the discrepancy can be partly explained by radiation losses into the substrate due to the thin metal film, and scattering losses from small roughnesses in the dielectric ridge and gold surface, which were not included in the calculations. Other explanations for the discrepancy include statistical errors introduced in the exponential fit and possible variations of the permittivity of the gold film, caused by the deposition process. The absence of mode beating confirms that the DLSPPW indeed is single mode as expected from theoretical predictions.[13]

The confinement of the DLSPPW modes has been investigated by characterizing S bends with different displacements [Fig. 4]. The recorded topographies show S bends resulting in a waveguide displacement of 5 μm [Fig. 4(b)] and 10 μm [Fig. 4(d)] over a distance of 10 μm. In the case of the small S bend, characterized with the smallest curvature radius $R_{min} \simeq 3.95$ μm, no significant bend loss can be observed from the optical image [Fig. 4(c)], and the strong scattering and back reflection at the termination of the waveguide [Fig. 4(g)] also imply low bend and propagation losses. From Figs. 4(c) and 4(e), it is clear that the size of the excitation spot (~15 μm) is large enough to cause SPPs propagating parallel to the DLSPPW at the gold-air interface, which then scatters off the DLSPPW bend. This could, how-

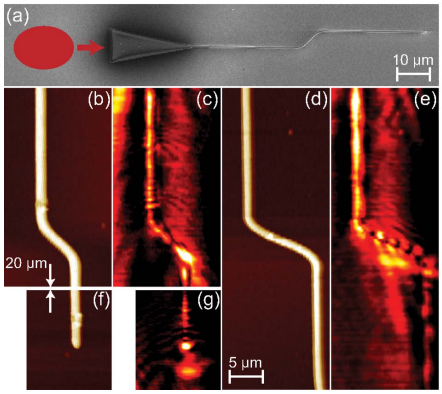

FIG. 4. (Color online) Near-field measurements of two different S bends, performed for $\lambda = 1550$ nm. (a) SEM image of an S bend with 5 μm displacement over a distance of 10 μm, where the ellipse illustrates the position of the excitation spot, and the arrow indicates the direction of SPP propagation. [(b) and (c)] Topographic and near-field optical images, respectively, of the S bend shown in (a). [(d) and (e)] Topographic and near-field optical images, respectively, of an S bend with a 10 μm displacement over a distance of 10 μm. [(f) and (g)] Topographic and near-field optical images, respectively, of the termination region of the S bend shown in (a). The images in (b)–(g) all share the scale shown in (d).

ever, be avoided either by placing funnels adjacent to the one used for in coupling, as was the case with the straight waveguides [Fig. 1(a)], or by decreasing the spot size to funnel width ratio. The large bend reveals some radiation effects at the bends due to the very small radius of curvature ($R_{\min} \simeq 2.48$ μm) of this bend [Fig. 4(e)]. Although some radiation losses occur, waveguiding can still be observed after the S bend, indicating very strong confinement of the DLSPPW modes.

In conclusion, it has been demonstrated, that it is possible to achieve strong mode confinement of SPPs at telecommunication wavelengths by utilizing ~550-nm-high and ~500-nm-wide dielectric ridges deposited on a thin gold film as waveguides. The use of a funnel structure for efficient in coupling of SPPs excited at the gold-air interface into DLSPPW modes is found advantageous, also because it reduces the propagation of SPPs at the gold-air interface adjacent to the waveguide. In addition to this, two S bends with different radii of curvature have been characterized, and it is found that a 5 μm displacement over a distance of 10 μm gives rise to very low radiation losses, confirming the strong confinement of the DLSPPW mode.

The authors acknowledge the financial support of the PLASMOCOM project (EC FP6 IST 034754 STREP).

[1] W. L. Barnes, A. Dereux, and T. W. Ebbesen, Nature (London) **424**, 824 (2003).
[2] H. Raether, *Surface Plasmons—on Smooth and Rough Surfaces and on Gratings*, 1st ed. (Springer, Berlin, 1988).
[3] S. I. Bozhevolnyi, J. Erland, K. Leosson, P. M. W. Skovgaard, and J. M. Hvam, Phys. Rev. Lett. **86**, 3008 (2001).
[4] P. Berini, Phys. Rev. B **61**, 10484 (2000).
[5] T. Nikolajsen, K. Leosson, I. Salakhutdinov, and S. I. Bozhevolnyi, Appl. Phys. Lett. **82**, 668 (2003).
[6] A. Boltasseva, T. Nikolajsen, K. Leosson, K. Kjaer, M. S. Larsen, and S. I. Bozhevolnyi, J. Lightwave Technol. **23**, 413 (2005).
[7] I. V. Novikov and A. A. Maradudin, Phys. Rev. B **66**, 035403 (2002).
[8] D. K. Gramotnev and D. F. P. Pile, Appl. Phys. Lett. **85**, 6323 (2004).
[9] S. I. Bozhevolnyi, V. S. Volkov, E. Devaux, J.-Y. Laluet, and T. W. Ebbesen, Nature (London) **440**, 508 (2006).
[10] B. Steinberger, A. Hohenau, H. Ditlbacher, A. L. Stepanov, A. Drezet, F. R. Aussenegg, A. Leitner, and J. R. Krenn, Appl. Phys. Lett. **88**, 094104 (2006).
[11] B. Steinberger, A. Hohenau, H. Ditlbacher, F. R. Aussenegg, A. Leitner, and J. R. Krenn, Appl. Phys. Lett. **91**, 081111 (2007).
[12] C. Reinhardt, S. Passinger, B. N. Chichkov, C. Marquart, I. P. Radko, and S. I. Bozhevolnyi, Opt. Lett. **31**, 1307 (2006).
[13] T. Holmgaard and S. I. Bozhevolnyi, Phys. Rev. B **75**, 245405 (2007).
[14] A. V. Krasavin and A. V. Zayats, Appl. Phys. Lett. **90**, 211101 (2007).

Appendix C

Phys. Rev. B **78**, 2008

T. Holmgaard, S. I. Bozhevolnyi, L. Markey, A. Dereux, A. V. Krasavin, P. Bolger, and A. V. Zayats, *"Efficient excitation of dielectric-loaded surface plasmon-polariton waveguide modes at telecommunication wavelengths"*, Phys. Rev. B **78**, 165431 (2008).

Efficient excitation of dielectric-loaded surface plasmon-polariton waveguide modes at telecommunication wavelengths

Tobias Holmgaard*
Department of Physics and Nanotechnology, Aalborg University, Skjernvej 4A, DK-9220 Aalborg Øst, Denmark

Sergey I. Bozhevolnyi
Department of Physics and Nanotechnology, Aalborg University, Skjernvej 4A, DK-9220 Aalborg Øst, Denmark and Institute of Sensors, Signals, and Electrotechnics (SENSE), University of Southern Denmark, Niels Bohrs Allé 1, DK-5230 Odense M, Denmark

Laurent Markey and Alain Dereux
Institut Carnot de Bourgogne, UMR 5209 CNRS-Université de Bourgogne, 9 Av. A. Savary, BP 47 870, F-21078 DIJON Cedex, France

Alexey V. Krasavin, Pádraig Bolger, and Anatoly V. Zayats
Centre for Nanostructured Media, IRCEP, The Queens University of Belfast, Belfast BT7 1NN, United Kingdom
(Received 5 May 2008; revised manuscript received 10 September 2008; published 31 October 2008)

The excitation of surface plasmon-polariton (SPP) waveguide modes in subwavelength dielectric ridges deposited on a thin gold film has been characterized and optimized at telecommunication wavelengths. The experimental data on the electromagnetic mode structure obtained using scanning near-field optical microscopy have been directly compared to full vectorial three-dimensional finite element method simulations. Two excitation geometries have been investigated where SPPs are excited outside or inside the dielectric tapered region adjoint to the waveguide. The dependence of the efficiency of the SPP guided mode excitation on the taper opening angle has been measured and modeled. Single-mode guiding and strong lateral mode confinement of dielectric-loaded SPP waveguide modes have been characterized with the near-field measurements and compared to the effective-index method model.

DOI: 10.1103/PhysRevB.78.165431 PACS number(s): 73.20.Mf, 71.36.+c, 68.37.Uv, 42.79.Gn

I. INTRODUCTION

The recent acceleration of the research on photonic components based on surface plasmon polaritons (SPPs) is motivated by the expectation that plasmonics is able to combine the asset of optical components, with respect to bandwidth, and the asset of electronic components, with respect to size.[1,2] SPPs are collective oscillations in the surface plasma of a metal coupled to an optical wave, bound to, and propagating along, the metal-dielectric interface.[3,4] In addition to the signal carrying properties, SPPs have been found useful for other applications, such as achieving active photonic functionalities[5] and enhanced sensing and detection of biomolecules,[6] all utilizing the strong SPP field confinement near the metal-dielectric interface. The strong lateral confinement in the direction perpendicular to the SPP propagation is essential for the development of compact plasmonic circuits since it ensures smaller bend losses and higher density of components. It should be noted, however, that strong confinement is often achieved by reducing the SPP field in the dielectric, therefore, with an increase in the propagation loss. Thus, the choice of optimum waveguide structure often is subject to a trade-off. In addition to a demand of strong lateral confinement and low propagation loss, single-mode guiding by the plasmonic waveguide structures is usually desired in order to avoid various mode dispersion and interference effects.

Several metal-dielectric structures have been investigated for guiding SPPs. Channel SPP waveguides, where lateral confinement is achieved by fabricating a square or V shaped groove in a flat metal surface, have been subject to extensive theoretical and experimental investigations in recent years.[7–11] Rectangular metal stripes, where lateral confinement is achieved by shrinking the lateral extension of a thin metal film, have been investigated theoretically[12–14] and characterized experimentally.[15–17] Lateral SPP confinement has also been achieved by utilizing nanostructured periodic variations in the metal surface surrounding the waveguide[18] or by using chains of closely spaced metal nanoparticles as waveguides.[19,20]

An alternative and technologically simple approach to achieving SPP waveguiding with strong lateral confinement is the use of dielectric stripes deposited on a thin metal film, thereby achieving dielectric-loaded surface plasmon-polariton (DLSPP) waveguides (DLSPPWs). Such waveguides rely on the same principle used in conventional integrated optics, where high-index-contrast waveguides (waveguides with a core refractive index much higher than that of the surrounding cladding) are used to achieve a small mode size.[21] Dielectric optical elements for focusing, reflection and refraction,[22] and DLSPPWs (Refs. 23–26) have been analyzed, fabricated, and characterized at near-infrared wavelengths. The mode confinement, propagation loss, and single-mode conditions of DLSPPWs have been analyzed theoretically by the effective-index method (EIM) and finite element method (FEM) at telecommunication wavelengths,[27] as have basic passive plasmonic components such as bends,

splitters, and directional couplers.[28] The excitation and propagation of DLSPPW modes in straight waveguides and bends have also recently been reported at telecommunication wavelengths,[29] giving prospect of the realization of compact plasmonic components based on DLSPPWs. In this paper different schemes for exciting DLSPPW modes are analyzed and the mode confinement and propagation loss are characterized at telecommunication wavelengths.

The paper is organized as follows. In Sec. II the experimental and theoretical techniques employed in the characterization of DLSPPWs are presented and a description of the investigated sample is given. In Sec. III the results of the FEM calculations, the EIM calculations, and scanning near-field optical microscope (SNOM) characterization are presented. Finally in Sec. IV a discussion of the obtained results is given and we offer our conclusions.

II. METHODS AND MATERIALS

In the characterization of the excitation and propagation of DLSPPW modes a SNOM imaging system is utilized and in modeling the FEM and the EIM are applied. After a description of the sample configuration, a brief introduction to the methods is presented.

A. Sample configuration

The investigated sample consists of polymethylmethacrylate (PMMA) ridges ($n_r=1.493$) lying on an $\sim$50 nm thin gold film thermally evaporated on a 170 μm thick glass substrate. The fabrication process is briefly described as follows: after the initial substrate cleaning and gold deposition, a PMMA film was spin coated from 950 K molecular weight PMMA resist (Allresist Gmbh, Ref. AR-P 671.04) and soft baked. Photolithography was performed on a Süss Microtech MJB4 mask aligner, equipped with UV250 optics, using the vacuum mode, and the resist was finally developed in methyl-isobutyl-ketone. Due to in coupling considerations the DLSPPWs are extended by funnel tapering structures [Fig. 1(a)].

Four different in coupling funnels with a fixed width of 10 μm and a length varying from 10 to 25 μm in steps of 5 μm are realized in a DLSPPW block. The optimum waveguide dimensions, i.e., ridge height and width, were deduced by simultaneously considering mode confinement and propagation loss while retaining the demand of single-mode DLSPPWs.[27] Investigation of the sample with a scanning electron microscope (SEM) reveals a waveguide width of $w\sim500$ nm [Fig. 1(b)]. Application of an atomic force microscope (AFM) in the investigation of the sample yields a waveguide height of $h\sim550$ nm [Figs. 1(c) and 1(d)]. These waveguide dimensions are found in accordance with the calculated design parameters presented in Ref. 27.

B. SNOM measurements

The experimental setup for near-field characterization of DLSPPW structures consists of an aperture SNOM operating in collection mode [Fig. 2]. The sample under investigation is placed on a glass prism using index matching immersion

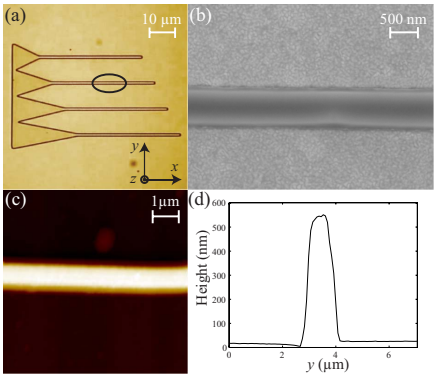

FIG. 1. (Color online) (a) Microscope image of a DLSPPW block with four different tapering structures. (b) SEM image of a straight section of a waveguide, revealing a waveguide width of $w\sim500$ nm. (c) AFM image of a straight section of a waveguide and (d) cross sectional profile of the AFM image revealing a waveguide height of $h\sim550$ nm.

oil. SPPs are excited utilizing two different schemes, but common for both is that a lensed fiber is used to focus a *p*-polarized Gaussian beam to a spot size of $\sim$15 μm at the gold surface opposite to the DLSPPW components, thus exciting SPPs by means of the Kretschmann-Raether configuration.[4] An uncoated etched fiber tip is raster scanned across the sample surface, whereby topographic and near-field optical images are achieved. In one excitation scheme SPPs are excited at the gold-air interface $\sim$20 μm before the in coupling funnel by matching the lateral component of the incident wave vector to that of SPPs propagating along, and bound to, the gold-air interface (see Fig. 3). In this configuration the funnels have the effect of coupling the SPPs into DLSPPW modes by total internal reflection (TIR) in the dielectric funnel. Moreover, close to the waveguides these funnels will screen the propagation of SPPs at the gold-air interface. In the other excitation scheme DLSPPs are excited directly in the funnel region by matching the lateral compo-

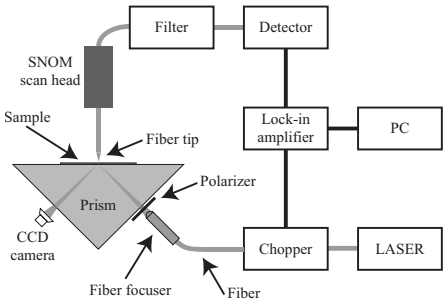

FIG. 2. The experimental setup of the SNOM imaging system used to obtain near-field optical images of the DLSPPW structures.

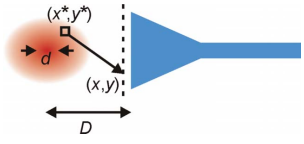

FIG. 3. (Color online) Schematic drawing illustrating the calculation of the incident SPP field distribution used in the 3D FEM calculations.

nent of the incident wave vector to that of SPPs propagating along, and bound to, the gold-PMMA interface. This is done by utilizing a high-index prism ($n=1.73$).

C. FEM calculation

Numerical simulation of funnel efficiency is performed using full three-dimensional (3D) FEM calculations, proved to be very rigorous in simulation of various photonic and plasmonic structures.[27,30,31] This method solves Maxwell's equations in frequency domain without any simplifications. As a refractive index for gold a tabulated value $n_{\mathrm{Au}}=0.55-11.5i$, taken from Ref. 33, was used. Simulation of the whole setup including attenuated total reflection (ATR) coupling of light into a SPP wave propagating at the metal surface before the funnel proved too demanding in three dimensions in terms of the simulation domain volume. To overcome this problem, only the essential processes of coupling into the DLSPPW mode using a funnel and its further propagation are simulated while calculating the SPP wave fields incident on the funnel analytically. The incident SPP field distribution at a distance of 1 μm before the funnel was calculated using a standard method of calculating diffracted fields in optics.[32] The laser spot, of Gaussian profile and with diameter $d=10$ μm, incident at an angle of $\psi=40°$ was placed at a distance $D=15$ μm from the funnel (see Fig. 3).

The phase distribution of the excited SPP wave was derived from the condition of resonant SPP excitation $k_x=\mathrm{Re}(k_{\mathrm{SPP}})$. Thus the following expression for the y component of the magnetic field, completely defining the incident SPP field, appears:

$$H_y(x,y) \propto \int A_0(x^*,y^*)\exp[i\phi_0(x^*)]K_{\mathrm{damp}}(x,y,x^*,y^*) \times \exp[i\phi(x,y,x^*,y^*)]\cos(\alpha)dx^*dy^*, \quad (1)$$

where

$$A_0(x^*,y^*) = \exp[-x^{*2}/(d/(2\cos\psi)^2) - y^{*2}/(d/2)^2] \quad (2)$$

represents the amplitude distribution of the incident beam,

$$\phi_0(x^*) = \mathrm{Re}(k_{\mathrm{SPP}})x^*, \quad (3)$$

its phase distribution,

$$K_{\mathrm{damp}}(x,y,x^*,y^*) = \frac{\exp(-\sqrt{(x-x^*)^2+(y-y^*)^2}\,\mathrm{Im}(k_{\mathrm{SPP}}))}{\sqrt[4]{(x-x^*)^2+(y-y^*)^2}}, \quad (4)$$

represents damping of SPP wave due to the radial spreading and the absorption damping, and

$$\cos(\alpha) = (x-x^*)/\sqrt{(x-x^*)^2+(y-y^*)^2} \quad (5)$$

represents the cosine of the SPP incident angle.

D. EIM calculation

The EIM is one of the standard methods for mode analysis of optical and SPP waveguides, attractive due to its simplicity and low demand for computational capabilities. The method is known to yield reasonably accurate results for DLSPPW modes far from cutoff,[27] which is the case for the DLSPPW modes considered in this work. In the EIM the two-dimensional cross section of the DLSPPW is considered and solved for guided modes by consecutively considering two one-dimensional waveguide structures. In the first step of the EIM the waveguide geometry is considered to have infinite lateral extend, thus the problem is reduced to finding bound modes in a multilayer waveguide. In this step the waveguide is considered as an air-PMMA-gold-glass structure, where the air and glass layers are considered semi-infinite in extend, and the mode p-polarized. In the second step a three layer structure with infinite vertical extend and s-polarized fields is considered. The mode effective index found in the first step is used to represent the middle layer (ridge region), enclosed by two semi-infinite layers with mode index set to that of a SPP wave at a gold-air interface. By solving this multilayer structure the mode indexes for bound SPP modes supported by the DLSPPW geometry are found.[27]

III. RESULTS

The DLSPPW block with four different tapering designs has been characterized by using near-field imaging with a SNOM in order to determine the efficiency for coupling in SPPs excited at the bare gold-air interface, i.e., the fraction of the power of the incident SPP field which is coupled into a guided DLSPPW mode [Figs. 4(a) and 4(b)]. The same in coupling structures have also been investigated using the FEM, where the incident SPP field distribution has been calculated as described in Sec. II C [Figs. 4(c) and 4(d)].

Both experimental and theoretical results show an increase in the coupling efficiency with increasing funnel length. Furthermore the characterization shows that the longer tapers, which have smaller funnel angle, cause less scattering at the end of the tapering region as the incident SPP wave hits the dielectric-air boundary under a larger angle. Thus it experiences TIR not only at the first intersection with the funnel boundary, as is the case with the shortest funnel. In both experimental and simulation field maps, oscillations in the field intensity can be observed along both taper and waveguide. By analyzing the modes existing in the funnel (particularly their effective indexes, defining the inter-

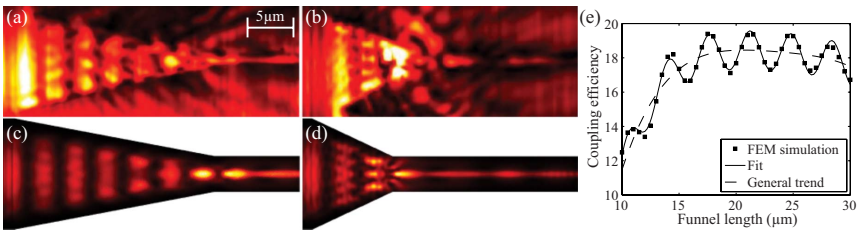

FIG. 4. (Color online) Near-field optical images of the tapering region of the DLSPPWs at the free space excitation wavelength $\lambda = 1550$ nm. [(a) and (c)] SNOM and FEM images, respectively, of a 10×25 μm^2 funnel. [(b) and (d)] SNOM and FEM images, respectively, of a 10×10 μm^2 funnel. (e) Coupling efficiency as a function of taper length, calculated using the FEM, where the incident SPP field is kept identical for all funnel lengths. The reconstructed SPP power flow at the beginning of the straight waveguide section is normalized to the power flow incident on the funnel, thus obtaining the coupling efficiency. The images in (a)–(d) share the scale shown in (a).

ference period) it was found that the oscillations in the FEM and SNOM images can be explained by the interference between the fundamental TM_{00} mode, excited when the SPP hits the taper, and freely propagating waves, part of which also propagate inside the taper before spreading out in the process of diffraction. A detailed analysis of the coupling efficiency performed with the FEM reveals that the efficiency initially increases with funnel length until reaching a level where the increase in efficiency, due to better focusing, is balanced by the increased loss caused by longer propagation through the funnel [Fig. 4(e)]. For the shortest taper the losses are found to be caused by SPPs escaping through the sides of the funnel, accounting for ~50% loss, SPP scattering through the top of the funnel, accounting for ~15%, and absorption losses from propagation through the funnel, accounting for ~10%, while a smaller fraction is lost due to reflection from the initial funnel boundary and excitation of freely propagating waves in the ridge waveguide. For longer funnels the fraction lost due to propagation increases and the losses due to scattering through the sides of the funnel and excitation of freely propagating waves in the ridge decreases, whereas the other loss factors are more or less constant. It is logical that with further taper length increase the propagation loss becomes dominant and the performance of the taper will be decreasing. Thus the optimal value of the taper length is estimated to be ~20 μm.

In the determination of the coupling efficiency great care has been taken to eliminate influence of the oscillations along the waveguide, which can be observed in Figs. 4(c) and 4(d). By analyzing the interference pattern along the waveguide it was possible to derive only the desired SPP signal, which was then used to evaluate the coupling efficiency. The oscillations in the coupling efficiency as a function of funnel length [Fig. 4(e)] are found to be primarily caused by the propagating waves in the funnel, which are diffracted at the end of the taper and thus couple to the SPP mode in the waveguide. This contribution will interfere with the main one (originating from the TM_{00} mode in the funnel) and produce the oscillations observed in the coupling efficiency. Depending with which phase difference these SPP and propagating waves in the taper arrive at the taper end, a different result of interference of the SPP waveguide modes produced from each of them occurs. Moreover, the periodicity of the phase difference of the taper SPP and light modes are given by their interference in the taper ~3.5 μm. The same periodicity is observed in the coupling efficiency, which confirms this explanation.

The method of excitation of SPPs at the gold-air interface and subsequent coupling into bound DLSPPW modes is attractive due to its simplicity; however, it has some apparent disadvantages, which become clear when considering profiles of the near-field optical images (Fig. 5). An averaged cross-sectional profile of the near-field optical image taken at the straight waveguide section just after the tapering region [see Fig. 5(c)] reveals that a strongly confined DLSPPW mode indeed is excited; however, it is also apparent that scattered light from the funnel along with copropagating SPPs at the gold-air interface (not screened by the funnel) result in a large degree of background. This is undesired and a potential problem when realizing plasmonic components such as bends and splitters, where the waveguide is displaced, as the copropagating fields will scatter off the waveguides.[29] A profile of the near-field optical image taken parallel to the waveguide, through the funnel and the waveguide, shows that the DLSPP field is damped when propagating through the funnel as the effect of propagation loss is larger than the focusing effect of the funnel [Fig. 5(d)]. The oscillations that can be observed are caused by interference between the TM_{00} mode and propagating modes as discussed above.

The alternative excitation scheme, where DLSPP modes are excited directly in the tapering structure, is attractive as it is expected that no copropagating SPP fields at the gold-air interface are excited due to the much higher effective index of the dielectric funnel region. This is indeed observed by SNOM characterization of a 10×25 μm^2 funnel (Fig. 6).

An averaged cross-sectional profile of the near-field optical image taken at the straight waveguide section just after the end of the funnel shows a highly confined DLSPPW mode with no copropagating SPPs at the gold-air interface and almost no apparent scattering originating from the end of the funnel [Fig. 6(c)]. A profile of the near-field optical signal taken parallel to the waveguide shows a strong buildup of the DLSPP mode in the tapering region [Fig. 6(d)]. This effect is strongly opposed to that observed in the other excitation method [Fig. 5(d)] and is caused by several factors all con-

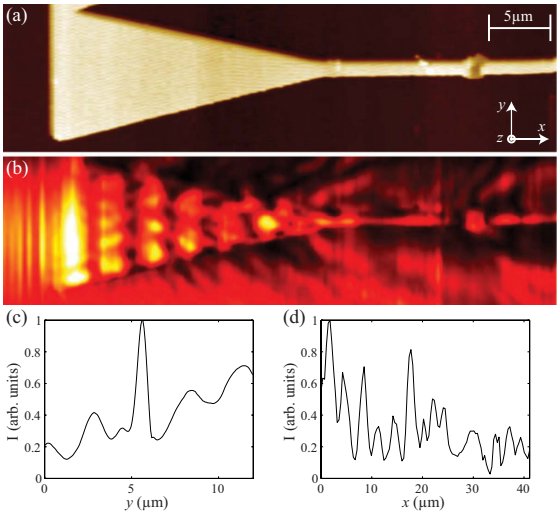

FIG. 5. (Color online) SNOM images of a 10×25 μm^2 funnel in coupling, where SPPs are excited at the gold-air interface outside the tapering region (in the area to the left of the funnel, not shown in the images), for the free space excitation wavelength $\lambda=1550$ nm. [(a) and (b)] Topographical and near-field optical images, respectively, obtained with the SNOM imaging system. (c) Averaged cross sectional profile of the near-field optical image taken at the straight waveguide section just after the end of the funnel. (d) Averaged profile of the near-field optical image taken parallel with the waveguide, through the funnel and waveguide regions.

tributing to a stronger optical signal toward the end of the tapering region. First the excitation of SPPs by the attenuated TIR method causes a strong initial increase in SPP intensity, as the propagation loss initially has a small effect. Second the tapering structure has a focusing effect toward the funnel end due to TIR of DLSPPs, which will also result in a stronger optical signal toward the funnel end. Finally the imaging process further enhances this trend as near-field optical modes with lower effective indexes are picked up more strongly with the tapered fiber, and as the mode effective index of a dielectric ridge decreases with width this also contributes to a stronger optical signal toward the funnel end. Due to the strong excitation of DLSPPWs without causing copropagating SPPs and scattering of SPPs, this excitation scheme is found highly attractive and superior to the previously described excitation method and has thus been used in the achievement of the results presented in the rest of the paper.

The propagation and confinement of DLSPPW modes in straight waveguides have been characterized by considering a waveguide section ~ 50 μm after the tapering region using SNOM imaging at the free space excitation wavelength λ

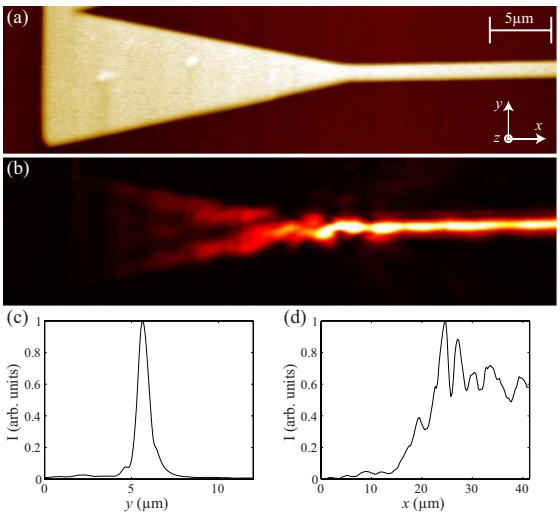

FIG. 6. (Color online) SNOM images of a 10×25 μm^2 funnel in coupling, where SPPs are excited at the gold-PMMA interface inside the tapering region, for the free space excitation wavelength $\lambda=1550$ nm. [(a) and (b)] Topographical and near-field optical images, respectively, obtained with the SNOM. (c) Averaged cross-sectional profile of the near-field optical image taken at the straight waveguide section just after the end of the funnel. (d) Averaged profile of the near-field optical image taken parallel with the waveguide through the funnel and waveguide regions.

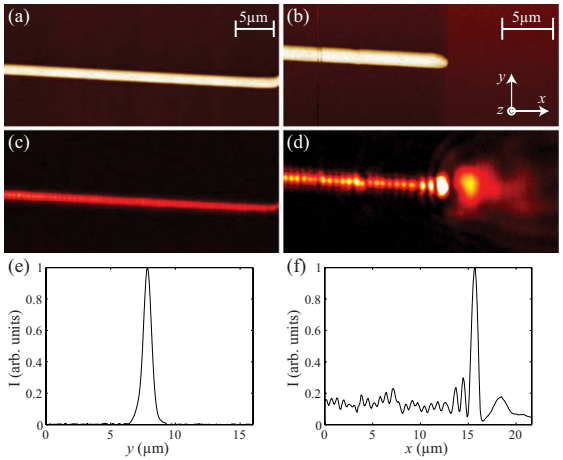

FIG. 7. (Color online) SNOM images of a straight DLSPPW section and a waveguide termination, recorded at the free space excitation wavelength $\lambda=1550$ nm. [(a) and (c)] Topographical and near-field optical images, respectively, of a straight DLSPPW section. [(b) and (d)] Topographical and near-field optical images, respectively, of a waveguide termination. (e) Cross sectional profile of the near-field optical image in (c) yielding a FWHM of ~743 nm. (f) Profile of the near-field optical image in (d) taken parallel with the waveguide, revealing an interference pattern with a period of $\Lambda \sim 700$ nm.

$=1550$ nm [Figs. 7(a) and 7(c)]. The near-field optical image shows a strongly confined DLSPPW mode, and the absence of mode beating confirms that the designed DLSPPW structure indeed only supports a single TM mode. The mode width is investigated by making an averaged cross-sectional profile of the near-field optical signal, revealing a full width at half maximum (FWHM) of ~743 nm [Fig. 7(e)], indicating subwavelength confinement. The waveguide termination region has also been investigated by using SNOM imaging, and it is found that even after propagation over more than ~100 μm a strong DLSPPW signal exists as can be observed from the strong scattering at the waveguide termination [Figs. 7(b) and 7(d)]. An interference pattern can be observed in the near-field optical signal, and by considering a profile taken along the waveguide the interference period is found to be $\Lambda \sim 700$ nm [Fig. 7(f)]. This interference pattern is thus found to be caused by interference between the forward propagating DLSPPW (TM_{00}) mode with mode effective index $N_{\mathrm{eff}} \sim 1.21$ (EIM calculations at $\lambda=1550$ nm yields $N_{\mathrm{eff}}=1.22$) and a backward propagating light wave with effective index close to 1. The origin of the backward propagating light wave is the waveguide termination, where the DLSPPW mode is scattered from. No significant back reflection of the DLSPPW mode inside the ridge for the termination is expected due to the, in this respect, relatively small difference in mode effective index between the DLSPPW mode and a SPP at the gold-air interface and the fact that the termination of the dielectric ridge is not completely abrupt. This is supported from FEM simulations of a DLSPPW termination, where the reflectivity has been estimated to be ~5%.

The propagation loss in the fabricated DLSPPWs has been investigated by using near-field imaging with a SNOM to characterize a straight waveguide section at different wavelengths in the telecommunication range (Fig. 8). From EIM calculations the DLSPPWs are expected to show similar properties at the investigated telecommunication wavelengths, however, with an increase in propagation length

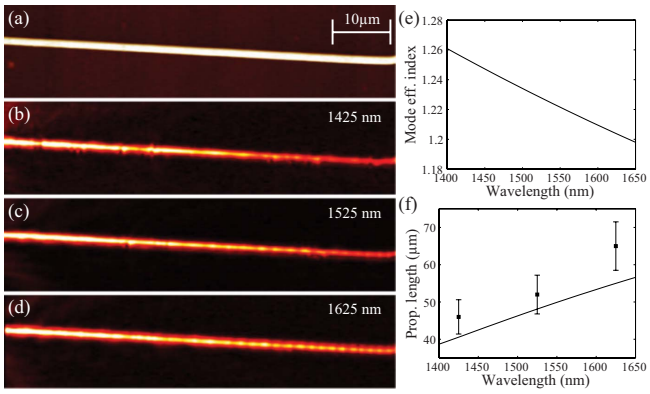

FIG. 8. (Color online) SNOM images of a straight waveguide at different free space excitation wavelengths. (a) Topographic image, (b) near-field optical image for $\lambda=1425$ nm, where the propagation length is determined to $L=46$ μm, (c) near-field optical image for $\lambda=1525$ nm, where $L=52$ μm, and (d) near-field optical image for $\lambda=1625$ nm, where $L=65$ μm. [(e) and (f)] Mode effective index and propagation length, respectively, as a function of wavelength, calculated by utilizing the EIM (fully drawn line) and measured with the SNOM (squares) (Ref. 33).

with increasing wavelength, at the expense of poorer mode confinement (lower mode effective index) [Figs. 8(e) and 8(f)]. This trend is confirmed from contemplation of the obtained near-field optical images, where an exponential fit to an averaged profile taken along the waveguide yields propagation lengths of $L=46$ μm, $L=52$ μm, and $L=65$ μm at the free space excitation wavelengths $\lambda=1425$ nm, $\lambda=1525$ nm, and $\lambda=1625$ nm, respectively [Figs. 8(b)–8(d)]. It is observed that the measured propagation lengths in all cases are longer than those expected from the EIM calculations conducted for the DLSPPWs having the designed ridge width and height. This can be caused by several effects, where the most likely are found to be discrepancy in waveguide dimensions, e.g., smaller waveguide width than designed or a slightly trapezoidal shape of the waveguide, which can result in quite large deviations in propagation length.[27] Another possible cause could be discrepancy between the actual gold refractive index and that used in the EIM calculations.

IV. DISCUSSION AND CONCLUSIONS

The excitation and propagation of DLSPPW modes have been characterized at telecommunication wavelengths by utilizing calculations made with the FEM and the EIM and by near-field measurements with a SNOM. The performance of different funnel shaped tapering structures for coupling into DLSPPW modes, utilizing the Kretschmann-Raether configuration, has been investigated, and it was found that funnels with smaller opening angle, i.e., larger length to width ratio, proved better for in coupling. By analysis of field intensity maps obtained by numerical simulations with FEM and by near-field optical measurements with a SNOM it is found that the larger incident angle to the dielectric funnel boundary results in less scattering and better focusing toward the funnel end, thus resulting in stronger coupling into bound DLSPPW modes. This results in an increasing coupling efficiency with funnel length, until a certain length of ~ 20 μm, where the propagation loss through the funnel becomes dominant, thereby decreasing the efficiency. Two different excitation schemes, one where SPPs are excited at the bare gold-air interface and coupled into DLSPPW modes using the funnel and other where DLSPPs are excited directly in the dielectric funnel by using a high-index prism, were characterized by using near-field imaging with a SNOM. The second method is found superior, as it avoids excitation of copropagating SPPs at the gold-air interface, and as it minimizes scattering of SPPs off the funnel.

A straight waveguide section has been characterized with a SNOM imaging system in order to evaluate the mode confinement and propagation loss. The obtained images confirmed the expectation of single-mode propagation, as no mode beatings could be observed. A cross sectional profile of a near-field optical image obtained for $\lambda=1550$ nm showed a strong lateral confinement with a FWHM of ~ 743 nm. The mode effective index of the bound DLSPPW mode has been evaluated by contemplation of the waveguide termination where the forward propagating DLSPPW mode interferes with a backward propagating light wave originating from scattering at the waveguide termination. The mode effective index has been evaluated to be $N_{\mathrm{eff}} \sim 1.21$ for $\lambda=1550$ nm, in very good agreement with the EIM calculated index of $N_{\mathrm{eff}}=1.22$. The propagation lengths, measured at the telecommunication wavelengths $\lambda=1425$ nm, $\lambda=1525$ nm, and $\lambda=1625$ nm by making an exponential fit to near-field optical images obtained with a SNOM, showed an increase with wavelength expected from theoretical investigations. The measured propagation lengths are longer than those expected from the EIM calculations, which is found to be a result of slightly differing waveguide dimensions and possible variations in the gold refractive indexes from those used in EIM calculations.

In conclusion we have demonstrated efficient excitation of DLSPPW modes with low background noise, single-mode propagation, strong confinement, and reasonably low propagation loss, all issues which are crucial for realizing efficient plasmonic components. We conduct further investigations in this area.

ACKNOWLEDGMENTS

The authors thank Thomas Søndergaard for help in developing a multilayer waveguide program used in this work and Jens Rafaelsen for assistance in SEM imaging of the samples. The financial support of the EC FP6 STREP PLASMOCOM (Grant No. IST 034754) is acknowledged. A.V.K., P.B., and A.V.Z. acknowledge the financial support of EPSRC-GB (U.K.).

*holmgaard@nano.aau.dk

[1] W. L. Barnes, A. Dereux, and T. W. Ebbesen, Nature (London) **424**, 824 (2003).
[2] E. Ozbay, Science **311**, 189 (2006).
[3] V. M. Agranovich and D. L. Mills, *Surface Polaritons—Electromagnetic Waves at Surfaces and Interfaces*, 1st ed. (North-Holland, Amsterdam, 1982).
[4] H. Raether, *Surface Plasmons—on Smooth and Rough Surfaces and on Gratings*, 1st ed. (Springer-Verlag, Berlin, 1988).
[5] A. V. Zayats, I. I. Smolyaninov, and A. Maradudin, Phys. Rep. **408**, 131 (2005).
[6] S. Lal, S. Link, and N. J. Halas, Nat. Photonics **1**, 641 (2007).
[7] I. V. Novikov and A. A. Maradudin, Phys. Rev. B **66**, 035403 (2002).
[8] D. K. Gramotnev and D. F. P. Pile, Appl. Phys. Lett. **85**, 6323 (2004).
[9] S. I. Bozhevolnyi, Opt. Express **14**, 9467 (2006).
[10] S. I. Bozhevolnyi, V. S. Volkov, E. Devaux, J.-Y. Laluet, and T. W. Ebbesen, Nature (London) **440**, 508 (2006).
[11] S. I. Bozhevolnyi and J. Jung, Opt. Express **16**, 2676 (2008).
[12] P. Berini, Phys. Rev. B **61**, 10484 (2000).
[13] R. Zia, M. D. Selker, and M. L. Brongersma, Phys. Rev. B **71**,

165431 (2005).
[14] J. Jung, T. Søndergaard, and S. I. Bozhevolnyi, Phys. Rev. B **76**, 035434 (2007).
[15] T. Nikolajsen, K. Leosson, I. Salakhutdinov, and S. I. Bozhevolnyi, Appl. Phys. Lett. **82**, 668 (2003).
[16] K. Leosson, T. Nikolajsen, A. Boltasseva, and S. I. Bozhevolnyi, Opt. Express **14**, 314 (2006).
[17] P. Berini, R. Charbonneau, and N. Lahoud, Nano Lett. **7**, 1376 (2007).
[18] S. I. Bozhevolnyi, J. Erland, K. Leosson, P. M. W. Skovgaard, and J. M. Hvam, Phys. Rev. Lett. **86**, 3008 (2001).
[19] M. Quinten, A. Leitner, J. R. Krenn, and F. R. Aussenegg, Opt. Lett. **23**, 1331 (1998).
[20] S. A. Maier, P. G. Kik, H. A. Atwater, S. Meltzer, E. Harel, B. E. Koel, and A. A. G. Requicha, Nature Mater. **2**, 229 (2003).
[21] C. Manolatou, S. G. Johnson, S. Fan, P. R. Villeneuve, H. A. Haus, and J. D. Joannopoulos, J. Lightwave Technol. **17**, 1682 (1999).
[22] A. Hohenau, J. R. Krenn, A. L. Stepanov, A. Drezet, H. Ditlbacher, B. Steinberger, A. Leitner, and F. R. Aussenegg, Opt. Lett. **30**, 893 (2005).
[23] C. Reinhardt, S. Passinger, B. N. Chichkov, C. Marquart, I. P. Radko, and S. I. Bozhevolnyi, Opt. Lett. **31**, 1307 (2006).
[24] B. Steinberger, A. Hohenau, H. Ditlbacher, A. L. Stepanov, A. Drezet, F. R. Aussenegg, A. Leitner, and J. R. Krenn, Appl. Phys. Lett. **88**, 094104 (2006).
[25] B. Steinberger, A. Hohenau, H. Ditlbacher, F. R. Aussenegg, A. Leitner, and J. R. Krenn, Appl. Phys. Lett. **91**, 081111 (2007).
[26] S. Massenot, J. Grandidier, A. Bouhelier, G. C. des Francs, L. Markey, J.-C. Weeber, A. Dereux, J. Renger, M. U. Gonzàlez, and R. Quidant, Appl. Phys. Lett. **91**, 243102 (2007).
[27] T. Holmgaard and S. I. Bozhevolnyi, Phys. Rev. B **75**, 245405 (2007).
[28] A. V. Krasavin and A. V. Zayats, Appl. Phys. Lett. **90**, 211101 (2007).
[29] T. Holmgaard, S. I. Bozhevolnyi, L. Markey, and A. Dereux, Appl. Phys. Lett. **92**, 011124 (2008).
[30] M. P. Nezhad, K. Tetz, and Y. Fainman, Opt. Express **12**, 4072 (2004).
[31] A. V. Krasavin, A. S. Schwanecke, and N. I. Zheludev, J. Opt. A, Pure Appl. Opt. **8**, S98 (2006).
[32] E. Hecht, *Optics*, 4th ed. (Addison-Wesley, San Francisco, 2002).
[33] E. D. Palik, *Handbook of Optical Constants of Solids*, 1st ed. (Academic, New York, 1985).

Appendix D

Opt. Express **16**, 2008

T. Holmgaard, Z. Chen, S. I. Bozhevolnyi, L. Markey, A. Dereux, A. V. Krasavin, and A. V. Zayats, *"Bend- and splitting loss of dielectric-loaded surface plasmon-polariton waveguides"*, Opt. Express **16**, 13585-13592 (2008).

Bend- and splitting loss of dielectric-loaded surface plasmon-polariton waveguides

Tobias Holmgaard[1], Zhuo Chen[1], Sergey I. Bozhevolnyi[1,2], Laurent Markey[3], Alain Dereux[3], Alexey V. Krasavin[4], and Anatoly V. Zayats[4]

[1]*Department of Physics and Nanotechnology, Aalborg University, Skjernvej 4A, DK-9220, Aalborg Øst, Denmark*

[2]*Institute of Sensors, Signals, and Electrotechnics (SENSE), University of Southern Denmark, Niels Bohrs Allé 1, DK- 5230 Odense M, Denmark*

[3]*Institut Carnot de Bourgogne, UMR 5209 CNRS-Université de Bourgogne, 9 Av. A. Savary, BP 47 870, F-21078 DIJON Cedex, France*

[4]*Centre for Nanostructured Media, IRCEP, The Queens University of Belfast, Belfast BT7 1NN, United Kingdom*

holmgaard@nano.aau.dk

Abstract: The design, fabrication, characterization, and modeling of basic building blocks of plasmonic circuitry based on dielectric-loaded surface polariton waveguides, such as bends, splitters, and Mach-Zehnder interferometers are presented. The plasmonic components are realized by depositing subwavelength dielectric ridges on a smooth gold film using mass-production-compatible UV-photolithography. The near-field characterization at telecommunication wavelengths shows the strong mode confinement and low radiation and bend losses. The performance of the devices is found in good agreement with results obtained by full vectorial three-dimensional finite element simulations.

OCIS codes: (240.6680) Surface plasmons; (250.5300) Photonic integrated circuits; (250.5460) Polymer waveguides

References and links

1. H. Raether, *Surface Plasmons on Smooth and Rough Surfaces and on Gratings*, 1st ed. (Springer-Verlag, Berlin, 1988).
2. R. Zia, J. A. Schuller, A. Chandran, and M. L. Brongersma, "Plasmonics: the next chip-scale technology," Mater. Today **9**, 20–27 (2006).
3. E. Ozbay, "Plasmonics: Merging photonics and electronics at nanoscale dimensions," Science **311**, 189–193 (2006).
4. T. W. Ebbesen, C. Genet, and S. I. Bozhevolnyi, "Surface-plasmon circuitry," Phys. Today **61**, 44–50 (2008).
5. W. L. Barnes, A. Dereux, and T. W. Ebbesen, "Surface plasmon subwavelength optics," Nature (London) **424**, 824–830 (2003).
6. S. A. Maier and H. A. Atwater, "Plasmonics: Localization and guiding of electromagnetic energy in metal/dielectric structures," J. Appl. Phys. **98**, 011101 (2005).
7. S. Lal, S. Link, and N. J. Halas, "Nano-optics from sensing to waveguiding," Nat. Photonics **1**, 641–648 (2007).
8. I. V. Novikov and A. A. Maradudin, "Channel polaritons," Phys. Rev. B **66**, 035403 (2002).
9. S. I. Bozhevolnyi, V. S. Volkov, E. Devaux, J.-Y. Laluet, and T. W. Ebbesen, "Channel plasmon subwavelength waveguide components including interferometers and ring resonators," Nature (London) **440**, 508–511 (2006).

10. V. S. Volkov, S. I. Bozhevolnyi, E. Devaux, J.-Y. Laluet, and T. W. Ebbesen, "Wavelength selective nanophotonic components utilizing channel plasmon polaritons," Nano Lett. **7**, 880–884 (2007).
11. C. Reinhardt, S. Passinger, B. N. Chichkov, C. Marquart, I. P. Radko, and S. I. Bozhevolnyi, "Laser-fabricated dielectric optical components for surface plasmon polaritons," Opt. Lett. **31**, 1307–1309 (2006).
12. B. Steinberger, A. Hohenau, H. Ditlbacher, A. L. Stepanov, A. Drezet, F. R. Aussenegg, A. Leitner, and J. R. Krenn, "Dielectric stripes on gold as surface plasmon waveguides," Appl. Phys. Lett. **88**, 094104 (2006).
13. B. Steinberger, A. Hohenau, H. Ditlbacher, F. R. Aussenegg, A. Leitner, and J. R. Krenn, "Dielectric stripes on gold as surface plasmon waveguides: Bends and directional couplers," Appl. Phys. Lett. **91**, 081111 (2007).
14. T. Holmgaard and S. I. Bozhevolnyi, "Theoretical analysis of dielectric-loaded surface plasmon-polariton waveguides," Phys. Rev. B **75**, 245405 (2007).
15. A. V. Krasavin and A. V. Zayats, "Passive photonic elements based on dielectric-loaded surface plasmon polariton waveguides," Appl. Phys. Lett. **90**, 211101 (2007).
16. S. Massenot, J. Grandidier, A. Bouhelier, G. C. des Francs, L. Markey, J.-C. Weeber, A. Dereux, J. Renger, M. U. Gonzàlez, and R. Quidant, "Polymer-metal waveguides characterization by Fourier plane leakage radiation microscopy," Appl. Phys. Lett. **91**, 243102 (2007).
17. A. V. Krasavin and A. V. Zayats, "Three-dimensional numerical modeling of photonic integration with dielectric-loaded SPP waveguides," Phys. Rev. B **78**, 045425 (2008).
18. T. Holmgaard, S. I. Bozhevolnyi, L. Markey, and A. Dereux, "Dielectric-loaded surface plasmon-polariton waveguides at telecommunication wavelengths: Excitation and characterization," Appl. Phys. Lett. **92**, 011124 (2008).
19. A. Kumar and S. Aditya, "Performance of s-bends for integrated-optic waveguides," Microwave Opt. Technol. Lett. **19**, 289–292 (1998).

1. Introduction

Photonic components based on surface plasmon polaritons (SPPs) have attracted great interest in recent years due to the enticing promise of realizing compact optical circuits with high bandwidths. SPPs, being electromagnetic light waves coupled to collective oscillations in the surface plasma of a metal, are bound to, and propagate along, a metal-dielectric interface. SPPs feature a strong confinement in the direction perpendicular to the metal-dielectric interface due to the exponential field decay away from the interface [1]. They open the possibility of combining the asset of electronics, with respect to size, and photonics, with respect to bandwidth [2, 3, 4]. A key design parameter for realization plasmonic, i.e. SPP-based, components is thus to obtain strong lateral confinement (strong confinement is essential for lower bend losses and higher densities of components) while preserving single-mode operation and keeping propagation losses low. By utilizing nanostructured sub-wavelength-sized metal surfaces, confinement of the SPPs below the diffraction limit is possible [5, 6, 7]. One of the most promising approaches for achieving strong lateral confinement of the SPP fields, simultaneously with relatively low propagation loss, is to utilize V-grooves milled in an otherwise smooth metal surface [8, 9, 10]. This method, however, currently requires complex fabrication techniques using ion-beam milling not applicable for large-scale industrial applications. Another approach for achieving lateral confinement is to employ dielectric-loaded SPP waveguides (DLSPPWs), comprised of dielectric ridges deposited on a smooth gold film [11, 12, 13]. By carefully designing the width and height of the ridges, single-mode propagation and very strong lateral confinement can be achieved with this technology [14, 15, 16, 17]. This promising approach is naturally compatible with different dielectrics and can easily be adapted for industrial fabrication using UV lithography [18]. Here we report the design, fabrication, characterization and modeling of DLSPPW based subwavelength components operating at telecommunication wavelengths.

A metal-dielectric interface is known to support the SPP propagation characterized with the propagation constant β determined by the corresponding dielectric constants, ε_m and ε_d, and light wavelength λ : $\beta = (2\pi/\lambda)[\varepsilon_d\varepsilon_m/(\varepsilon_d + \varepsilon_m)]^{0.5}$ [1]. The real part of β can be related to the SPP effective refractive index, i.e., $N_{eff} = (\lambda/2\pi)Re(\beta)$, implying that the presence of a dielectric layer on the top of a metal surface results in a higher SPP index as compared to a

metal-air interface. Dielectric ridges deposited on the metal surface, known as DLSPPWs [14], can thereby guide SPP modes similarly to conventional dielectric waveguides known in fiber and integrated optics. Comprehensive analysis and simulations conducted for telecommunication wavelengths have shown that, for typical dielectrics with the refractive index of ~ 1.5, the optimum ridge parameters are ~ 500 nm of width and ~ 600 nm of height [14]. Numerical simulations [15, 17] and experimental investigations [11, 18] of DLSPPW components confirmed that DLSPPWs with these parameters are suitable for achieving relatively low bend and propagation losses at telecom wavelengths. We have also demonstrated the possibility of large-scale printing of DLSPPWs with UV lithography [18] rather than writing point-by-point with electron-beam [12, 13] or by using two-photon polymerization lithography [11].

In the present work, we introduce and investigate in detail the operation of basic building blocks of integrated optical circuits: S-bends (i.e., curved bends connecting two parallel waveguides offset with respect to each other), Y-splitters which are composed of two mirrored S-bends and Mach-Zehnder interferometers realized by combining two parallel waveguide sections with two mirrored Y-splitters. All waveguide structures were fabricated using deep UV lithography (wavelength of ~ 250 nm) with a mask aligner in the vacuum contact mode and a ~ 550-nm-thick layer of poly-methyl-methacrylate (PMMA) resist spin-coated on a 60-nm-thin gold film, which was supported by a thin glass substrate. Typically, the width of the produced waveguides, inspected with scanning electron microscopy (SEM), was close to 500 nm ensuring the single-mode (and close to optimum) DLSPPW operation [14]. The performance of the fabricated components was characterized using a collection scanning near-field optical microscope (SNOM) having an uncoated fiber tip used as a probe, and an arrangement for SPP excitation (at $\lambda = 1,500 - 1,620$ nm) in the Kretschmann-Raether configuration [1], as described in detail elsewhere [18]. All waveguide structures were connected to funnel structures [Fig. 1(a)] facilitating efficient excitation of the DLSPPW mode [18]. However, in contrast with the previous experiments [11, 18], the DLSPPW mode was excited directly inside the taper [Fig. 1(b) and (c)] by matching the excitation angle (in total internal reflection configuration). This resulted in that the recorded SNOM images were of high quality, being practically free from background associated with SPP waves propagating along uncoated areas of the sample (cf. Fig. 1 of this manuscript and Fig. 4 from Ref. [18]).

2. S-bends

The design of S-bends was based on sine curves [19], allowing for continuous bend curvature and thereby adiabatic modification of the DLSPPW mode throughout the bend. Using the SNOM, we characterized several 10-μm-long S-bends with different offsets d, ranging from 2 to 15 μm, and observed for small offsets ($d \leq 5$ μm) excellent performance [Fig. 1(d) and (e)] that gradually deteriorated with the offset increase due to the radiation (into SPP waves) out of the bend [Fig. 1(f) and (g)]. However, even the S-bend with the largest offset ($d = 15$ μm), and the smallest curvature radius of 1.95 μm, transmitted a noticeable amount of DLSPPW mode radiation [Fig. 1(h) and (i)] confirming the strong confinement of the DLSPPW mode.

Bend transmission data (Fig. 2) has been calculated using full vectorial three-dimensional finite element method (3D-FEM) numerical simulations and obtained directly from the SNOM images by averaging the optical signal over a few micro-meters just before and after the S-bend (see Fig. 1(d)). The calculated and measured transmission values were found in good agreement with each other [Fig. 2], and this agreement is also observed in the optical images when comparing the field intensity distributions obtained with the 3D-FEM simulations (see insets in Fig. 2) with the near-field images obtained with the SNOM [Fig. 1]. Note that the transmission shown in Fig. 2 reflects not only the pure bend loss (due to the mode radiation out of the bend) but also the DLSPPW mode propagation loss (due to absorption in gold)

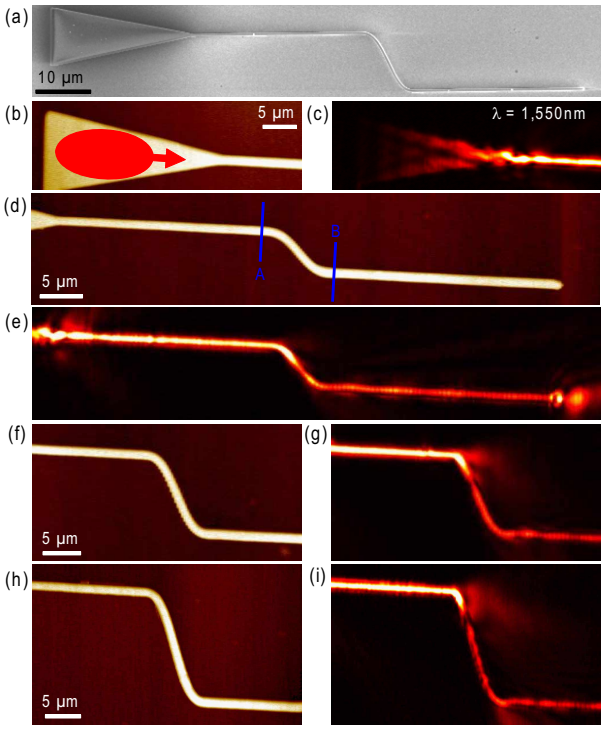

Fig. 1. Plasmonic tapers and S-bends: (a) SEM image of a taper waveguide structure comprising a 10-μm-long S-bend with an offset of 10 μm; (b) topographical and (c) near-field optical ($\lambda = 1,550$ nm) images of the SPP excitation in the taper region and coupling into the single-mode waveguide; (d) topographical and (e) near-field optical ($\lambda = 1,550$ nm) images of the SPP mode propagation in a 10-μm-long S-bend with an offset of 5 μm (note the out-coupling of the SPP waveguide mode into a free-propagating and diverging SPP wave at the waveguide termination). [(f) and (g)] As (d) and (e) but for a waveguide offset of 10 μm. [(h) and (i)] As (f) and (g) but for a waveguide offset of 15 μm.

accumulated over the length of 10-μm-long S-bends. Given the DLSPPW propagation length (whether it being ~ 47 μm as found with the 3D-FEM simulations or ~ 50 μm as obtained from the SNOM images), the pure bend loss is found very small ($< 10\%$) for $d \leq 3$ μm, whereas it constitutes the main loss contribution for $d > 6$ μm.

3. Y-splitters

The performance of 10-μm-long Y-splitters was studied in a similar manner by carrying out the SNOM characterization of Y-splitters fabricated with different arm separations ranging from 3

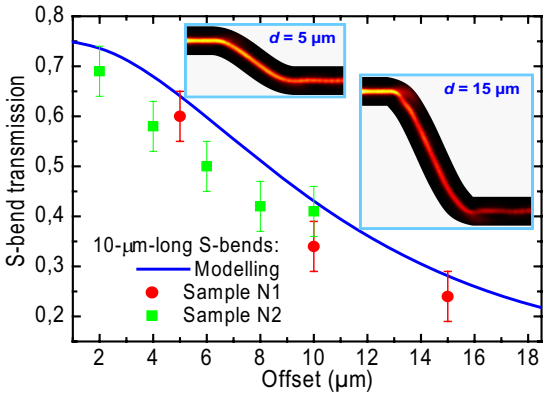

Fig. 2. S-bend transmission dependence on the offset distance between the arms for the 10-μm-long S-bends ($\lambda = 1{,}550$ nm) determined experimentally from SNOM images (similar to those shown in Fig. 1) and by modeling with 3D-FEM simulations. Insets show calculated intensity distributions in two S-bends with different offsets that should be compared to the optical images shown in Fig. 1(e) and Fig. 1(i). The error bars are obtained from single measurements and, thus, represent the uncertainty in each measurement due to variations in the optical signal.

to 30 μm [Fig. 3]. It is found that the Y-splitters feature pronounced rounding ($\sim$ 300-nm-radius) of the junction area (inset in Fig. 3(b) and (c)) due to limited resolution of the UV-lithography technique used for their fabrication. Such a rounding prevents adiabatic separation of the waveguides and introduces a mismatch between the incoming mode field (into the junction area) and the field of outgoing modes in the waveguide branches, resulting thereby in a transmission loss due to radiation out of the junction as SPP waves propagating in the forward direction on the smooth surface [Fig. 3(c), (e), and (g)]. The occurrence of this radiation along with its influence on the Y-splitter transmission was further verified with the 3D-FEM simulations [Fig. 4]. Simulation of Y-splitters with a 300-nm-radius rounding of the junction area (derived from the SEM image shown as inset in Fig. 3(b) and (c)) shows a $\sim$ 20% decrease in transmission related to the adiabatic splitters, which is in good agreement with the experimentally obtained values. Note that the transmission of adiabatic Y-splitters is expected to be very close to that of the corresponding S-bends (cf. Fig. 2 and Fig. 4), impelling one to improve on the resolution in DLSPPW fabrication, e.g. by exploiting optical proximity correction techniques.

4. Mach-Zehnder interferometers

Upon having achieved efficient splitting of DLSPPW modes, a natural step is to realize a Mach-Zehnder interferometer composed of a Y-splitter followed by two parallel waveguides sections, which are recombined by a mirrored Y-splitter. A 45-μm-long Mach-Zehnder interferometer with an arm separation of 3 μm, consisting of two 10-μm-long Y-splitters and a 25 μm straight waveguide section, has been fabricated and characterized [Fig. 5]. The path lengths of the two waveguide arms are identical as the fabricated Mach-Zehnder interferometer is symmetrical,

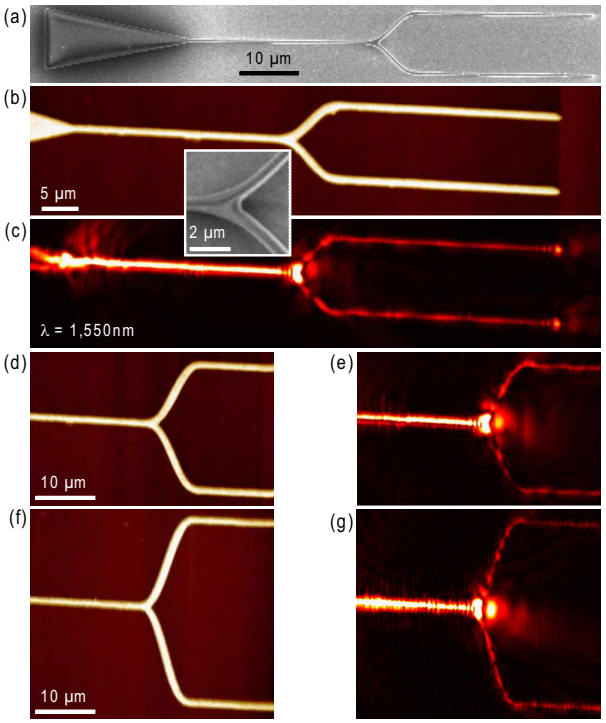

Fig. 3. Plasmonic Y-splitters composed of two mirrored S-bends: (a) SEM image of a taper waveguide structure comprising a 10-μm-long Y-splitter with the arm separation of 10 μm; (b) topographical and (c) near-field optical ($\lambda = 1,550$ nm) images of the Y-splitter shown in (a) along with an inset showing an SEM image of the junction area. [(d) and (e)] As (b) and (c) but for the arm separation of 20 μm. [(f) and (g)] As (d) and (e) but for the arm separation of 30 μm.

and thus constructive interference is expected and indeed observed [Fig. 5(b)], upon recombination of the SPP modes in the two waveguide arms. With an arm length of $\ell \sim 45$ μm and $\lambda = 1,550$ nm, the change in effective index of one arm needed for a switch to complete extinction is $\Delta N_{eff} = \lambda/(2\ell) \sim 1.72 \times 10^{-2}$, which is achievable, e.g., by utilizing thermo-optic effects. The transmission through the 45-μm-long Mach-Zehnder interferometer has been evaluated to ~ 20 %. Due to the overall length of the Mach-Zehnder interferometer the losses are largely dominated by the DLSPPW mode propagation loss accounting for ~ 74 % of the total loss. The fabricated Mach-Zehnder interferometer demonstrates efficient splitting and recombination of the DLSPPW modes as expected from the consideration of Y-splitters above. Furthermore, the near-field optical image confirms the strong lateral confinement of the DLSPPW

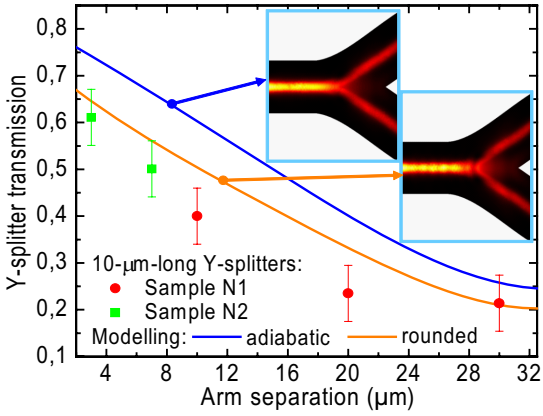

Fig. 4. Transmission of 10-μm-long Y-splitters ($\lambda = 1{,}550$ nm) as a function of arm separation determined experimentally from the SNOM images similar to the ones shown in Fig. 3 and by modeling with 3D-FEM simulations. Insets show the calculated intensity distributions in 10-μm-wide Y-splitters having adiabatic arm separation and 300-nm-radius rounding of the junction area respectively (the latter should be compared to the optical image in Fig. 3(c)).

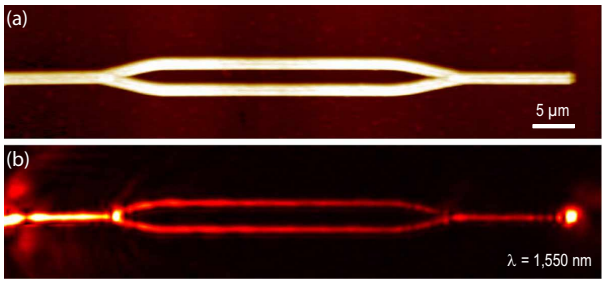

Fig. 5. Mach-Zehnder interferometer with an arm separation of 3 μm: (a) topographical and (b) near-field optical ($\lambda = 1{,}550$ nm) images, respectively. The SPP mode propagates from left to right.

mode as no mode beating between the parallel waveguides sections is observed [Fig. 5(b)], since the cross-talk is small for 3 μm separation between the waveguides [15, 17].

5. Conclusion

Using industrially compatible large-scale UV-lithography-based fabrication and exploiting the principles of DLSPPW-based plasmonic technology, we have realized compact and low-loss S-bends, Y-splitters and Mach-Zehnder interferometers. The performance of the fabricated pas-

sive plasmonic components has been investigated by applying a SNOM imaging system operating at telecommunication wavelengths, and an excellent correspondence to simulated results, obtained by using the 3D-FEM, has been found. Overall, the SNOM investigations showed that all fabricated basic DLSPPW components, S-bends and Y-splitters, performed as expected in the whole range of laser tunability, exhibiting single-mode and well-confined guiding with the loss level close to calculated, demonstrating thereby robustness to small variations in structural parameters. The pure bend loss of the fabricated S-bends is found very small for small displacements ($d \leq 5\,\mu$m), but dominates the loss contribution for larger displacements. SNOM imaging of Y-splitters demonstrates the realization of a 50/50 splitting of the DLSPPW mode, however, the fabricated Y-splitters exhibit a rounding of the junction area, with a resulting additional radiation loss as compared to an adiabatical split of the waveguide. Thus, the performance of the considered structures could be further improved by perfecting the fabrication (e.g., by using optical proximity correction techniques). The investigated 45 μm-long Mach-Zehnder interferometer, in addition, demonstrates efficient recombination of two DLSPPW modes, yielding a total transmission of ~ 20 %, which can be improved by reducing the overall length of the interferometer (if allowed by the desired functionality), as ~ 74 % of the loss is caused by Ohmic absorption losses during SPP propagation.

Acknowledgments

This work was supported by the FP6 STREP PLASMOCOM (IST 034754). AZ also acknowledges the financial support from EPSRC (UK).

Appendix E

Appl. Phys. Lett. **94**, 2009

T. Holmgaard, Z. Chen, S. I. Bozhevolnyi, L. Markey, A. Dereux, A. V. Krasavin, and A. V. Zayats, *"Wavelength selection by dielectric-loaded plasmonic components"*, Appl. Phys. Lett. **94**, 051111 (2009).

Wavelength selection by dielectric-loaded plasmonic components

Tobias Holmgaard,[1,a)] Zhuo Chen,[1] Sergey I. Bozhevolnyi,[2] Laurent Markey,[3] Alain Dereux,[3] Alexey V. Krasavin,[4] and Anatoly V. Zayats[4]
[1]*Department of Physics and Nanotechnology, Aalborg University, Skjernvej 4A, DK-9220 Aalborg Øst, Denmark*
[2]*Institute of Sensors, Signals and Electrotechnics (SENSE), University of Southern Denmark, Niels Bohrs Allé 1, DK-5230 Odense M, Denmark*
[3]*Institut Carnot de Bourgogne, UMR 5209 CNRS-Université de Bourgogne, 9 Av. A. Savary, BP 47 870, F-21078 Dijon Cedex, France*
[4]*Centre for Nanostructured Media, IRCEP, The Queen's University of Belfast, Belfast BT7 1NN, United Kingdom*

(Received 31 October 2008; accepted 6 January 2009; published online 6 February 2009)

Fabrication, characterization, and modeling of waveguide-ring resonators and in-line Bragg gratings for wavelength selection in the telecommunication range are reported utilizing dielectric-loaded surface plasmon-polariton waveguides. The devices were fabricated by depositing subwavelength-sized polymer ridges on a smooth gold film using industrially compatible large-scale UV photolithography. We demonstrate efficient and compact wavelength-selective filters, including waveguide-ring resonators with an insertion loss of ~2 dB and a footprint of only 150 μm^2 featuring narrow bandwidth (~20 nm) and high contrast (~13 dB) features in the transmission spectrum. The performance of the components is found in good agreement with the results obtained by full vectorial three-dimensional finite element simulations. © *2009 American Institute of Physics*. [DOI: 10.1063/1.3078235]

Surface plasmon polaritons (SPPs), being light waves coupled to free electron oscillations in metals,[1,2] can be laterally confined below the diffraction limit using subwavelength metal structures.[2–7] Plasmonic components open an enticing perspective of combining high operational bandwidth of photonic components with subwavelength dimensions of SPP waveguides.[6,7] Recently developed dielectric-loaded SPP waveguides (DLSPPWs), utilizing high effective indices of SPP modes guided by dielectric ridges on smooth metal films,[8–13] represent an attractive alternative to other plasmonic technologies by virtue of being naturally compatible with different dielectrics and industrial fabrication using UV lithography.[14,15] Preliminary investigations indicated that DLSPPW-based components feature relatively low bend and propagation losses[14,15] but their potential for wavelength selection, a crucial functionality for any photonic circuit, has so far not been explored.

Here we report on the investigation of main wavelength-selective DLSPPW components such as waveguide-ring resonators (WRRs) and in-line Bragg gratings (BGs) exploited for wavelength selection in the telecommunication range.

All devices were fabricated using deep-UV lithography (wavelength of ~250 nm) with a Süss Microtech MJB4 mask aligner in the vacuum contact mode and a ~550-nm-thick layer of polymethyl-methacrylate (PMMA) resist spin coated on a 60-nm-thin gold film, which was supported by a thin glass substrate. Typically, the width of the produced waveguides, inspected with scanning electron microscopy (SEM), was close to 500 nm ensuring the single mode (and close to optimum) DLSPPW operation.[10] The performance of the fabricated components was characterized using a collection scanning near-field optical microscope (SNOM) having an uncoated fiber tip used as a probe and an arrangement for SPP excitation ($\lambda = 1500-1620$ nm) in the Kretschmann configuration,[1] as described in detail elsewhere.[14,15] All waveguide structures were connected to funnel structures [Fig. 1(a)], facilitating efficient excitation of the DLSPPW mode,[16] with the further improvement in the DLSPPW mode, was excited *directly* inside the taper by matching the excitation angle (under total internal reflection), resulting in SNOM images of high quality.[16]

The first wavelength-selective components to be studied were WRRs designed to have 5-μm-radius rings separated by different gaps from straight DLSPPWs [Fig. 1(a)]. Using the SNOM imaging it was found that while the WRRs with the gaps (the minimum distance between the edge of the waveguide and the edge of the ring [Fig. 1(b)]) designed, having the widths $g \cong 2.53$ and 1.53 μm, did not exhibit noticeable ring-DLSPPW mode excitation, the WRR with the gap $g \cong 0.53$ μm [Fig. 1(b)] featured very efficient ring excitation and well-pronounced wavelength-dependent behavior [Figs. 1(d)–1(g)]. The SEM image of the $g \cong 0.53$ μm WRR reveals that the gap is not completely resolved as some residual PMMA resistance still exists in the gap [Fig. 1(b)], which is likely to cause slightly more coupling to the ring than expected for that gap size. Note that the WRR transmission [Fig. 1(h)] was evaluated using the input and output waveguide cross sections separated by 10 μm [Fig. 1(c)], a propagation length that alone introduces ~20% of loss as estimated from the DLSPPW propagation length of ~50 μm.

In general, the WRR transmission is expected to be periodic with respect to the phase accumulated by the ring-DLSPPW mode per circulation and can be described with the following expression:[17]

a)Electronic mail: holmgaard@nano.aau.dk.

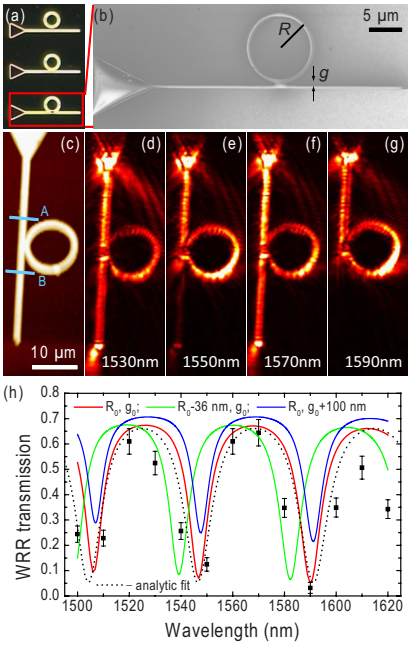

FIG. 1. (Color online) Plasmonic WRR. (a) Dark-field microscope image of fabricated WRRs with different gaps. (b) SEM image along with (c) topographical, and [(d)–(g)] near-field optical [λ=(*d*) 1530, (e) 1550, (f) 1570, and (g) 1590 nm] SNOM images of the investigated WRR. (h) Transmission WRR spectra determined experimentally from SNOM images [similar to (d)–(g)] using an analytic fit by Eq. (1) and with 3D-FEM simulations for 10-μm-long input-to-output propagation [marked by lines A and B in (c)] and for three sets of WRR parameters: ring radius R_0=5486 nm and gap width g_0=250 nm, R=5450 nm and g=250 nm, R=5486 nm, and g =350 nm.

$$T = \exp(-l/L_{SP})\frac{\alpha^2 + t^2 - 2\alpha t\cos\theta}{1 + \alpha^2 t^2 - 2\alpha t\cos\theta}, \quad (1)$$

where $\theta=(2\pi/\lambda)n_{eff}(\lambda)2\pi R$. The first factor in Eq. (1) reflects the power loss incurred by the propagation over the distance l=10 μm related to the DLSPPW propagation length $L_{SP}\sim 50$ μm. α is the mode propagation and bend loss in the ring, t is the mode transmission through the coupling region in the straight waveguide,[17] λ is the light wavelength in air, R is the ring radius, and $n_{eff}(\lambda)$ is the DLSPPW effective index, whose dispersion has to be taken into account. When fitting the experimental data [Fig. 1(h)], we used the calculated[10] mode dispersion resulting in $n_{eff}(\lambda) \cong 1.61-0.25\lambda(\mu m)$, finding other parameters to be at $\alpha \cong 0.55$, $t\cong 0.7$, and $R\cong 5.43$ μm. Note that the fitted mode loss in the ring α implies that the bend loss amounted to ~0.36 dB/rad was indeed relatively small as expected. Finally, it is seen that the investigated WRR features nearly *complete extinction* (reaching ~13 dB at 1590 nm) with a ~20-nm bandwidth, showing thereby much better performance than the channel plasmon polariton (CPP)-based WRRs of the same size.[18]

Full three-dimensional finite element (3D-FEM) simulations of the WRR transmission using the ring radius R and ring-waveguide gap g as fitting parameters are presented in Fig. 1(h). It is seen that the WRR transmission calculated for R_0=5486 nm and g_0=250 nm, being close to the analytic fit, reproduces well the experimental features. More importantly, the simulations predict the observed trend of increasing the contrast with wavelength much better than the fit by virtue of taking consistently into account the DLSPPW dispersion influencing the phase delay, insertion loss, and coupling strength. Note that the positions of the minima are very sensitive to the ring radius, whereas their level is strongly influenced by the gap width (controlling the coupling strength), indicating the tolerance level in the WRR design and fabrication.

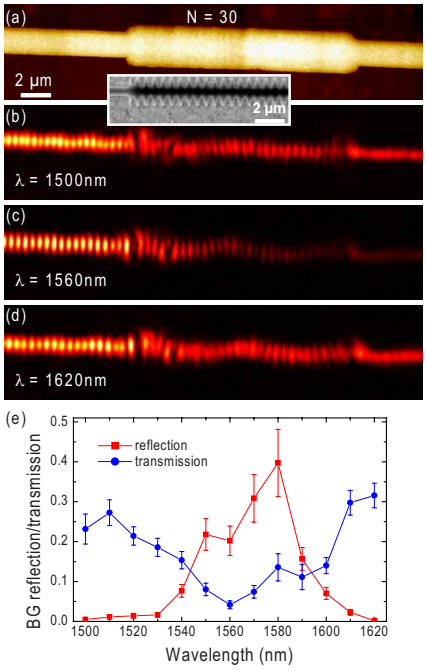

FIG. 2. (Color online) Plasmonic BG. (a) Topographical and [(b)–(d)] near-field optical [λ=(*b*) 1500, (c) 1560, and (d) 1620 nm] SNOM images of an 18-μm-long BG with the period of 600 nm along with an inset showing an SEM image of the BG section. (e) BG reflection and transmission spectra determined experimentally from SNOM images similar to (b)–(d).

Wavelength selection can also be realized with diffraction gratings, e.g., by using in-line BG-based filters well known in integrated optics and introduced recently for long range SPP waveguides.[19,20] We made use of the dependence of DLSPPW mode index on the dielectric ridge width,[10] and fabricated 600-nm-period step-in-width (from 500 nm to 2 μm) BGs with 300-nm-long intervals between wide BG sections and containing different number of periods: N=10, 20, 30, and 50. The DLSPPW mode index variation was estimated[10] between ~1.2 and 1.4 at λ~1.55 μm, so that the BG transmission minimum was expected at $\lambda\cong 2\Lambda n_{av}$ =1.56 μm (Λ and n_{av} being the grating period and average DLSPPW mode index). The advantage of this design is that the BG fabrication does not require additional processing (as,

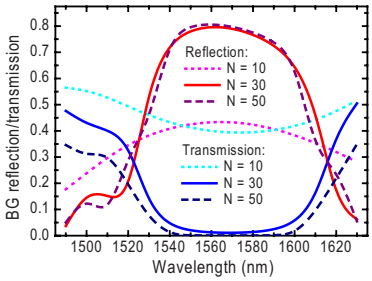

FIG. 3. (Color online) Reflection and transmission BG spectra calculated with 3D-FEM simulations for the 600 nm period BGs with different numbers of grating periods: $N=10$, 30, and 50.

for example, step-in-depth gratings[20]). However, UV lithography resolution is more critical here than in the above case of the WRRs because of small-sized (~300 nm) features throughout the whole BG length, resulting in more pronounced proximity effects, seen as a rounding of the gratings, affecting the geometry of fabricated BGs [see inset in Fig. 2(a)]. Still, the 30-period BG exhibited well-defined Bragg reflection and extinction in transmission with the wavelength interval of 1540–1600 nm (Fig. 2). Note that relatively low transmission levels (~0.3) observed outside of the band gap are partially accounted for by the DLSPPW mode propagation loss reducing alone the transmission to ~0.7. In comparison, the 20-period BG performed similarly but with considerably weaker Bragg reflection (~0.15) and extinction (~0.13), while the 50-period BG featured about the same Bragg reflection but very low transmission (<0.15) at all wavelengths.

The 3D-FEM simulations of BG reflection and transmission (Fig. 3) showed all the main features observed: the well defined band gap (seen in both reflection and transmission) within the range of 1540–1600 nm, the similar reflection for $N=30$ and $N=50$ but lower transmission for the latter, and the rather weak band-gap effects for $N=10$. However, the simulated BG characteristics are much better with respect to the insertion loss (most probably due to weaker out-of-plane scattering), a circumstance that we attribute to the structural imperfections.

In conclusion, in using industrially compatible large-scale UV-lithography-based fabrication and exploiting the principles of DLSPPW-based plasmonic technology, we have realized efficient and compact wavelength-selective components: WRRs and BGs, operating at telecommunication wavelengths. In particular, we have demonstrated the WRR with an insertion loss of ~2 dB and a footprint of only 150 μm^2 ($\sim 60\lambda^2$) featuring deep minima (with the contrast of up to ~13 dB) in its wavelength transmission spectrum with a bandwidth of ~20 nm. Taking into account that this technology is naturally compatible with different dielectrics, one can envisage the development of ultracompact plasmonic components utilizing thermo-, electro-, magneto-, acousto-, and nonlinear optical effects as well as being integrated with electrical circuits.

This work was supported by EC FP6 STREP PLASMOCOM. A.V.Z. also acknowledge the financial support from EPSRC (UK).

[1] H. Raether, *Surface Plasmons on Smooth and Rough Surfaces and on Gratings*, 1st ed. (Springer, Berlin, 1988).
[2] W. L. Barnes, A. Dereux, and T. W. Ebbesen, Nature (London) **424**, 824 (2003).
[3] S. A. Maier and H. A. Atwater, J. Appl. Phys. **98**, 011101 (2005).
[4] S. Lal, S. Link, and N. J. Halas, Nat. Photonics **1**, 641 (2007).
[5] W. A. Murray and W. L. Barnes, Adv. Mater.(Weinheim, Ger.) **19**, 3771 (2007).
[6] R. Zia, J. A. Schuller, A. Chandran, and M. L. Brongersma, Mater. Today **9**, 20 (2006).
[7] T. W. Ebbesen, C. Genet, and S. I. Bozhevolnyi, Phys. Today **61**, 44 (2008).
[8] C. Reinhardt, S. Passinger, B. N. Chichkov, C. Marquart, I. P. Radko, and S. I. Bozhevolnyi, Opt. Lett. **31**, 1307 (2006).
[9] B. Steinberger, A. Hohenau, H. Ditlbacher, A. L. Stepanov, A. Drezet, F. R. Aussenegg, A. Leitner, and J. R. Krenn, Appl. Phys. Lett. **88**, 094104 (2006).
[10] T. Holmgaard and S. I. Bozhevolnyi, Phys. Rev. B **75**, 245405 (2007).
[11] A. V. Krasavin and A. V. Zayats, Appl. Phys. Lett. **90**, 211101 (2007).
[12] B. Steinberger, A. Hohenau, H. Ditlbacher, F. R. Aussenegg, A. Leitner, and J. R. Krenn, Appl. Phys. Lett. **91**, 081111 (2007).
[13] A. V. Krasavin and A. V. Zayats, Phys. Rev. B **78**, 045425 (2008).
[14] T. Holmgaard, S. I. Bozhevolnyi, L. Markey, and A. Dereux, Appl. Phys. Lett. **92**, 011124 (2008).
[15] T. Holmgaard, Z. Chen, S. I. Bozhevolnyi, L. Markey, A. Dereux, A. V. Krasavin, and A. V. Zayats, Opt. Express **16**, 13585 (2008).
[16] T. Holmgaard, S. I. Bozhevolnyi, L. Markey, A. Dereux, A. V. Krasavin, P. Bolger, and A. V. Zayats, Phys. Rev. B **78**, 165431 (2008).
[17] A. Yariv, Electron. Lett. **36**, 321 (2000).
[18] S. I. Bozhevolnyi, V. S. Volkov, E. Devaux, J.-Y. Laluet, and T. W. Ebbesen, Nature (London) **440**, 508 (2006).
[19] S. Jetté-Charbonneau, R. Charbonneau, N. Lahoud, G. Mattiussi, and P. Berini, Opt. Express **13**, 4674 (2005).
[20] S. I. Bozhevolnyi, A. Boltasseva, T. Søndergaard, T. Nikolajsen, and K. Leosson, Opt. Commun. **250**, 328 (2005).

Appendix F

Opt. Express **17**, 2009

T. Holmgaard, Z. Chen, S. I. Bozhevolnyi, L. Markey, and A. Dereux, *"Dielectric-loaded plasmonic waveguide-ring resonators"*, Opt. Express **17**, 2968-2975 (2009).

Dielectric-loaded plasmonic waveguide-ring resonators

Tobias Holmgaard[1], Zhuo Chen[1], Sergey I. Bozhevolnyi[1,2], Laurent Markey[3], and Alain Dereux[3]

[1]*Department of Physics and Nanotechnology, Aalborg University, Skjernvej 4A, DK-9220, Aalborg Øst, Denmark*

[2]*Institute of Sensors, Signals, and Electrotechnics (SENSE), University of Southern Denmark, Niels Bohrs Allé 1, DK- 5230 Odense M, Denmark*

[3]*Institut Carnot de Bourgogne, UMR 5209 CNRS-Université de Bourgogne, 9 Av. A. Savary, BP 47 870, F-21078 DIJON Cedex, France*

holmgaard@nano.aau.dk

Abstract: Using near-field microscopy, the performance of dielectric-loaded plasmonic waveguide-ring resonators (WRRs) operating at telecom wavelengths is investigated for various waveguide-ring separations. It is demonstrated that compact (footprint $\sim 150\ \mu m^2$) and efficient (extinction ratio ~ 13 dB) WRR-based filters can be realized using UV-lithography. The WRR wavelength responses measured and calculated using the effective-index method are found in good agreement.

OCIS codes: (240.6680) Surface plasmons; (250.5300) Photonic integrated circuits; (250.5460) Polymer waveguides

References and links

1. H. Raether, *Surface Plasmons on Smooth and Rough Surfaces and on Gratings*, 1st ed. (Springer-Verlag, Berlin, 1988).
2. P. Berini, "Plasmon-polariton waves guided by thin lossy metal films of finite width: Bound modes of symmetric structures," Phys. Rev. B **61**, 10484 (2000).
3. T. Nikolajsen, K. Leosson, I. Salakhutdinov, and S. I. Bozhevolnyi, "Polymer-based surface-plasmon-polariton stripe waveguides at telecommunication wavelengths," Appl. Phys. Lett. **82**, 668–670 (2003).
4. S. I. Bozhevolnyi, J. Erland, K. Leosson, P. M. W. Skovgaard, and J. M. Hvam, "Waveguiding in Surface Plasmon Polariton Band Gap Structures," Phys. Rev. Lett. **86**, 3008–3011 (2001).
5. S. A. Maier, P. G. Kik, H. A. Atwater, S. Meltzer, E. Harel, B. E. Koel, and A. A. G. Requicha, "Local detection of electromagnetic energy transport below the diffraction limit in metal nanoparticle plasmon waveguides," Nat. Mat. **2**, 229–232 (2003).
6. S. I. Bozhevolnyi, V. S. Volkov, E. Devaux, and T. W. Ebbesen, "Channel plasmon-polariton guiding by subwavelength metal grooves," Phys. Rev. Lett. **95**, 046802 (2005).
7. S. I. Bozhevolnyi, V. S. Volkov, E. Devaux, J.-Y. Laluet, and T. W. Ebbesen, "Channel plasmon subwavelength waveguide components including interferometers and ring resonators," Nature (London) **440**, 508–511 (2006).
8. V. S. Volkov, S. I. Bozhevolnyi, E. Devaux, J.-Y. Laluet, and T. W. Ebbesen, "Wavelength selective nanophotonic components utilizing channel plasmon polaritons," Nano Lett. **7**, 880–884 (2007).
9. C. Reinhardt, S. Passinger, B. N. Chichkov, C. Marquart, I. P. Radko, and S. I. Bozhevolnyi, "Laser-fabricated dielectric optical components for surface plasmon polaritons," Opt. Lett. **31**, 1307–1309 (2006).
10. B. Steinberger, A. Hohenau, H. Ditlbacher, A. L. Stepanov, A. Drezet, F. R. Aussenegg, A. Leitner, and J. R. Krenn, "Dielectric stripes on gold as surface plasmon waveguides," Appl. Phys. Lett. **88**, 094104 (2006).
11. T. Holmgaard and S. I. Bozhevolnyi, "Theoretical analysis of dielectric-loaded surface plasmon-polariton waveguides," Phys. Rev. B **75**, 245405 (2007).

12. A. V. Krasavin and A. V. Zayats, "Passive photonic elements based on dielectric-loaded surface plasmon polariton waveguides," Appl. Phys. Lett. **90**, 211101 (2007).
13. A. V. Krasavin and A. V. Zayats, "Three-dimensional numerical modeling of photonic integration with dielectric-loaded SPP waveguides," Phys. Rev. B **78**, 045425 (2008).
14. S. Massenot, J. Grandidier, A. Bouhelier, G. C. des Francs, L. Markey, J.-C. Weeber, A. Dereux, J. Renger, M. U. Gonzàlez, and R. Quidant, "Polymer-metal waveguides characterization by Fourier plane leakage radiation microscopy," Appl. Phys. Lett. **91**, 243102 (2007).
15. T. Holmgaard, S. I. Bozhevolnyi, L. Markey, and A. Dereux, "Dielectric-loaded surface plasmon-polariton waveguides at telecommunication wavelengths: Excitation and characterization," Appl. Phys. Lett. **92**, 011124 (2008).
16. T. Holmgaard, Z. Chen, S. I. Bozhevolnyi, L. Markey, A. Dereux, A. V. Krasavin, and A. V. Zayats, "Bend- and splitting loss of dielectric-loaded surface plasmon-polariton waveguides," Opt. Express **16**, 13585–13592 (2008).
17. T. Nikolajsen, K. Leosson, and S. I. Bozhevolnyi, "Surface plasmon polariton based modulators and switches operating at telecom wavelengths," Appl. Phys. Lett. **85**, 5833–5835 (2004).
18. G. Gagnon, N. Lahoud, G. A. Mattiussi, and P. Berini, "Thermally Activated Variable Attenuation of Long-Range Surface Plasmon-Polariton Waves," J. Lightwave Technol. **24**, 4391–4402 (2006).
19. T. Holmgaard, S. I. Bozhevolnyi, L. Markey, A. Dereux, A. V. Krasavin, P. Bolger, and A. V. Zayats, "Efficient excitation of dielectric-loaded surface plasmon-polariton waveguide modes at telecommunication wavelengths," Phys. Rev. B **78**, 165431 (2008).
20. A. Yariv, "Universal relations for coupling of optical power between microresonators and dielectric waveguides," Electron. Lett. **36**, 321–322 (2000).

1. Introduction

In order to develop compact nanophotonic integrated circuits, it is essential to realize various individual components with specific functionalities to offer and requirements to meet. A possible solution for realizing compact integrated nanophotonic circuits is by utilizing surface plasmon-polaritons (SPPs), which are surface waves in the plasma of a metal coupled to light waves. SPPs are bound to, and propagate along a metal-dielectric interface, with the fields decaying exponentially away from its maximum at the interface [1]. This implies a strong inherent confinement in the direction perpendicular to the interface, and thus the design task consists of achieving single-mode waveguides with strong lateral confinement, and propagation loss as low as possible. Several proposals for plasmonic waveguides and integrated components have been made, e.g. by using metal stripes embedded in a dielectric [2, 3], SPP band gap structures [4], chains of metal particles [5], and V-groves cut into an otherwise planar metal surface [6, 7, 8].

An alternative, and technologically simple, approach to achieve ultra-compact plasmonic integrated components is to utilize dielectric stripes deposited on a smooth metal film as waveguides [9, 10]. This type of waveguides has been thoroughly investigated by utilizing the effective index method (EIM) and the finite element method (FEM) [11, 12, 13]. Near-field characterization of fabricated dielectric-loaded SPP waveguides (DLSPPWs) has revealed the realization of single-mode waveguides with sub-wavelength confinement and relatively low propagation loss [14, 15]. In addition compact basic plasmonic components such as bends, splitters and Mach-Zehnder interferometers have been fabricated and characterized, demonstrating efficient bending, splitting and recombination of DLSPPW modes [16]. Although the metal film (or stripes) supporting the dielectric ridges greatly enhances the propagation loss (compared to conventional dielectric waveguides), the presence of metal adjacent to the waveguides is also one of the greatest virtues of the DLSPPW technology. The main apparent advantage is in having simultaneously at hand a plasmonic and electrical circuit, whose metal stripes can be employed, e.g., for heating the dielectric ridges, thereby inducing a thermo-optical effect in the plasmonic waveguides by changing the refractive index of the ridge. This process is very efficient since, similarly to the case of thermo-optical components utilizing long-range SPPs [17, 18], the DLSPPW mode field is maximal at the metal-dielectric interface and thereby at the heating electrode, unlike in most conventional dielectric waveguides, where the mode power extends far out in the surrounding cladding and the proximity of electrodes should be avoided

to minimize the absorption loss. In this manner one can envisage the realization of wavelength tunable filters, controlled by applying a voltage over the underlying electrodes. As the DLSPPW technology is naturally compatible with different dielectrics, the realization of active plasmonic components utilizing electro-optical, magneto-optical, acousto-optical, or nonlinear optical effects is furthermore possible. In the present work we report on the design, fabrication and characterization of passive wavelength-band selective filters based on waveguide-ring resonators (WRRs), operating in the telecommunication range by utilizing the DLSPPW technology.

Samples are fabricated by deep UV lithography using a vacuum contact mask aligner with either a home-made mask or a manufactured commercial mask. The DLSPPW-ring resonators consist of $\sim$ 550-nm-high and $\sim$ 500-nm-wide poly-methyl-methacrylate(PMMA) ridges deposited on a 60-nm-thick gold film, which is supported by a thin glass substrate. These waveguide dimensions ensure single-mode propagation and close to optimum lateral mode confinement [11], at telecommunication wavelengths, which imply low bend losses imperative in the realization of compact WRRs. When preparing the samples for near-field characterization, they are placed on an equilateral prism using index matching immersion oil. DLSPPW modes are excited at telecommunication wavelengths by utilizing the Kretschmann-Raether configuration [1]. By focusing a Gaussian beam on the metal-prism interface opposite the waveguide structures, at an angle above that of total internal reflection, the lateral component of the incident wave-vector is matched to the effective mode index of the SPP in the dielectric ridge. In this particular case, a high-index prism is applied as funnel in-coupling structures (with high mode effective index), connected to the ridge waveguides, are utilized for more efficient DLSPPW excitation [Fig. 1(a)]. The near-field characterization is performed using a scanning near-field optical microscope (SNOM) operating in collection mode. In this setup an etched uncoated fiber tip is raster scanned across the sample, thus recording the topography and near-field optical signal as described in detail elsewhere [16, 19].

2. Coupling to ring resonators

The WRRs considered in this work consist of a straight waveguide, extended in one end by a funnel (used for coupling in SPPs), and a circular resonator placed in proximity of the straight waveguide to allow for coupling between the two [Fig. 1(a)]. In the design of WRRs one must

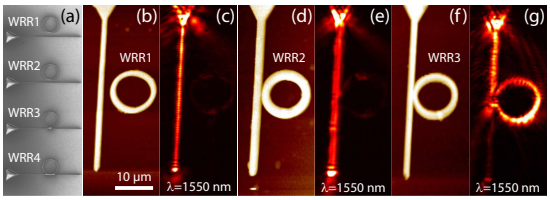

Fig. 1. (Color online) Waveguide-ring resonators with different gaps between the waveguide and the ring. (a) SEM image showing four WRRs with different gap sizes. [(b) and (c)] Topographical and near-field optical images, respectively of a WRR with a gap of $g \simeq 2.5\ \mu$m, [(d) and (e)] of a WRR with a gap of $g \simeq 1.5\ \mu$m, and [(f) and (g)] of a WRR with a gap of $g \simeq 0.5\ \mu$m. The images (b)-(g) share the scale shown in (b), and all near-field images are recorded for a free-space excitation wavelength of $\lambda = 1550$ nm.

carefully consider several parameters impacting the performance. The bandwidth of the WRR is determined by the radius of the ring resonator along with the wavelength dependent mode

effective index of the bent waveguide, whereas the extinction ratio (ratio between minimum and maximum signal output) is determined by the coupling strength to the ring and the attenuation due to SPP propagation and bend loss around the ring. In the design of the fabricated waveguides a fixed ring radius of $R = 5\ \mu$m has been used, whereas the gap between waveguide and ring is varied in order to investigate the effect on the extinction ratio. A weak coupling is expected for waveguide-ring gaps larger than $\sim 0.5\ \mu$m due to the very strong mode confinement [12, 15, 19] and short interaction region, which, by SNOM characterization of WRRs with gaps of $g \simeq 2.5\ \mu$m, $g \simeq 1.5\ \mu$m, and $g \simeq 0.5\ \mu$m, indeed is found to be the case [Fig. 1]. It is observed that the output signal is clearly damped in the $g \simeq 0.5\ \mu$m WRR [Fig. 1(g)], as compared to the two other WRRs, indicating strong coupling and good resonator performance in this case. For the WRR with the largest gap ($g \simeq 2.5\ \mu$m) a strongly confined DLSPPW mode propagates in the straight waveguide without any noticeable change in the interaction region [Fig. 1(c)]. This is also the case for the $g \simeq 1.5\ \mu$m WRR [Fig. 1(e)], whereas the $g \simeq 0.5\ \mu$m WRR exhibits strong coupling to the ring resonator [Fig. 1(g)].

A wavelength analysis of the $g \simeq 0.5\ \mu$m gap WRR reveals that the output signal is strongly modulated with a period of $\Lambda \simeq 45$ nm [Fig. 2]. Averaged cross sectional profiles of the near-

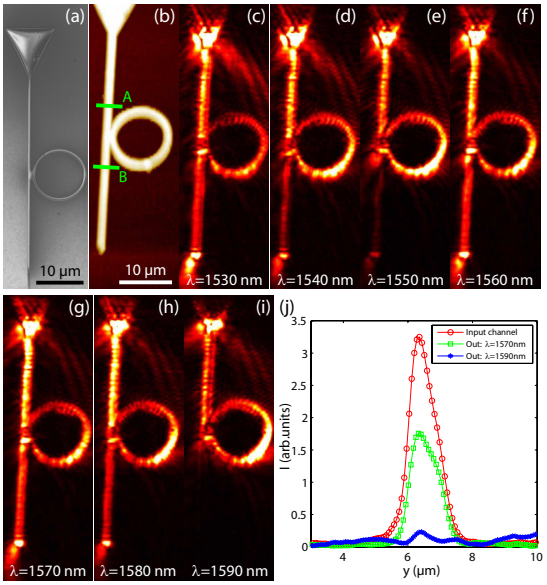

Fig. 2. (Color online) WRR with a gap of $g \simeq 0.5\ \mu$m. (a) SEM image of the whole WRR structure. (b) Topographical image recorded with the SNOM. [(c)-(i)] Near-field optical images with free-space excitation wavelength varying from 1530 nm to 1590 nm in steps of 10 nm, which share the scale shown in (b). (j) Averaged cross sectional profile of the near-field optical images (g) and (i), taken at lines A and B as marked in (b).

field optical signal taken perpendicular to the waveguide before and after the interaction region

(A and B in Fig. 2(b)) demonstrate the large contrast in output signal between wavelengths subject to constructive and destructive interference, respectively [Fig. 2(j)]. The near-field characterization of the $g \simeq 0.5$ μm WRR reveals an extinction ratio of ~ 13 dB, giving promise of realization of very effective band selective filters. An SEM image of the $g \simeq 0.5$ μm WRR reveals that the gap is not completely resolved as some residual PMMA resist still exists in the gap [Fig. 2(a)], which, by perfecting the fabrication, or by using lithography techniques more advanced than a simple contact mask aligner, is likely to be avoided. The effect of this non-resolved gap could be larger coupling to the ring than expected, and the effect of this is further investigated in the following.

3. Transmission through WRRs

In order to further investigate the periodic behavior of the WRR transmission, the measured transmission values are fitted to an analytical expression for the power transmission taken from [20]

$$T = \exp\left(\frac{-l}{L_{SP}(\lambda)}\right)\frac{\alpha^2 + t^2 - 2\alpha t\cos\theta}{1+\alpha^2 t^2 - 2\alpha t\cos\theta} \tag{1}$$

where scattering losses at the interaction region have been disregarded.

The first factor reflects the propagation loss from cross section A to B ($l = 10$ μm). $\alpha = \exp(-2\pi R\beta'')\sigma$ is the field attenuation factor per roundtrip around the ring (β'' being the imaginary part of the propagation constant of the DLSPPW mode and σ being a parameter accounting for the pure bend loss). t is the field transmission through the interaction region in the straight waveguide. $\theta = (2\pi/\lambda)N_{\text{eff}}(\lambda)2\pi R$ is the phase change around the ring, where λ is the free space excitation wavelength, and R is the ring radius. In the calculations the wavelength dependent power propagation length $L_{SP}(\lambda)$ and mode effective index $N_{\text{eff}}(\lambda)$ are taken from EIM calculations [11]. The fitting parameters are thus the ring radius R, determining the period of oscillations and position of transmission bands, and the ring bend loss factor σ, and transmission t determining the amplitude and offset of the oscillations.

By minimizing the total deviation from the measured transmission values a best fit is obtained for the $g \simeq 0.5$ μm WRR, where $R = 5.39$ μm, $\sigma = 0.71$ (giving α values in the range 0.49 to 0.52 due to the wavelength dependence of L_{SP}), and $t = 0.66$ [Fig. 3]. The realized ring radius is close to the designed, and gives a transmission bandwidth of ~ 20 nm, with a period of $\simeq 45$ μm. At resonance, i.e., for $\theta = m2\pi$ (m being an integer), Eq. (1) simplifies to

$$T = \exp\left(\frac{-l}{L_{SP}(\lambda)}\right)\frac{(\alpha - t)^2}{(1-\alpha t)^2} \tag{2}$$

implying that critical coupling occurs for $\alpha = t$. For the $g \simeq 0.5$ μm WRR this is quite close, and along with the relatively large α and t values, this gives the large extinction ratio of $\sim$ 13 dB. In order to achieve even larger extinction ratios a slight increase in α or decrease in t is necessary. By decreasing the gap between the waveguide and the ring a larger coupling ratio is expected, implying a smaller t value, however, the bend loss factor σ is not expected to change significantly due to unchanged ring radius and waveguide widths in the design.

A WRR with a gap of $g \simeq 0.3$ μm has been designed and fabricated using a second mask, and by characterization with the SNOM [Figs. 4(a)-(e)] transmission values were obtained [Fig. 4(f)].

Due to imperfect fabrication, the near-field optical images show more scattering than for the previous sample, implying that lower transmission values are to be expected as compared to the $g \simeq 0.5$ μm WRR. This trend is further enhanced due to the expectance of a lower t value, and by observing Fig. 4(f) this is indeed found to be the case. The best fit to the measured

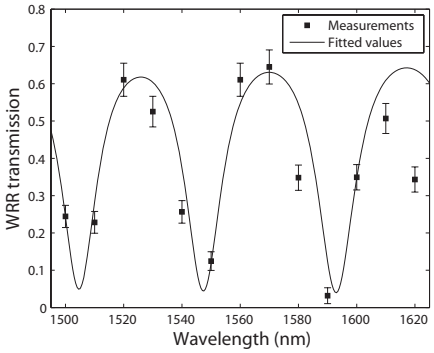

Fig. 3. Transmission through the WRR with a gap of $g \simeq 0.5\ \mu$m, measured by taking averaged cross sectional profiles of the optical images at the input A and output B (Fig. 2(b)), similar to those shown in Fig. 2(j). A fit to the measured transmission values is obtained by utilizing Eq. (1).

transmission values is found to be for $R = 4.90\ \mu$m, $\sigma = 0.66$ (giving α values in the range 0.47 to 0.50), and $t = 0.23$, indicating that the coupling change significantly by decreasing the gap by 200 nm. As expected the bend loss factor is almost unchanged, and the small variation is likely to be caused by scattering, or simply due to the slightly smaller ring radius of the fabricated WRR, originating from the second mask used.

On the same sample a WRR with a designed gap of $g = 0.0\ \mu$m, i.e., intersection between ring and waveguide, has been realized [Fig. 5]. In this case the coupling mechanism between the waveguide and the ring differs significantly, as the geometry in the interaction region resembles that of a double-width waveguide instead of two closely spaced waveguides. This double width waveguide is split into two arms, one continuing straight and one bending off as part of the ring resonator, by means of a Y-splitter like separation, which implies that a scattering loss in the intersection region is to be expected [16]. Due to the non-symmetric splitting of the double width waveguide a significantly smaller fraction of the mode power will be coupled to the ring resonator as this requires a change in wavevector in the intersection region. This implies that although the gap size is the smallest of the investigated WRRs a smaller coupling (larger transmission) is expected due to the different coupling mechanism. From the obtained near-field optical images [Fig. 5(b)-(e)] it is apparent the the coupling to the ring is much weaker than for the other investigated WRRs, and that the Y-splitting separation of the waveguide in the interaction region gives rise to a scattering loss. As the WRR is fabricated using the same mask as the $g \simeq 0.3\ \mu$m WRR, similar ring characteristics are expected, which is confirmed as the best fit to the measured transmission values is found to be $R = 4.89\ \mu$m, $\sigma = 0.65$ (giving α values in the range 0.47 to 0.49), and $t = 0.79$. The larger transmission implies a higher throughput, but lower extinction ratio, relative to the $g \simeq 0.5\ \mu$m WRR, as apparent from Eq. (2).

4. Conclusion

Compact wavelength selective waveguide-ring resonators have been designed and fabricated by using large-scale compatible UV lithography to deposit PMMA ridges on a smooth gold

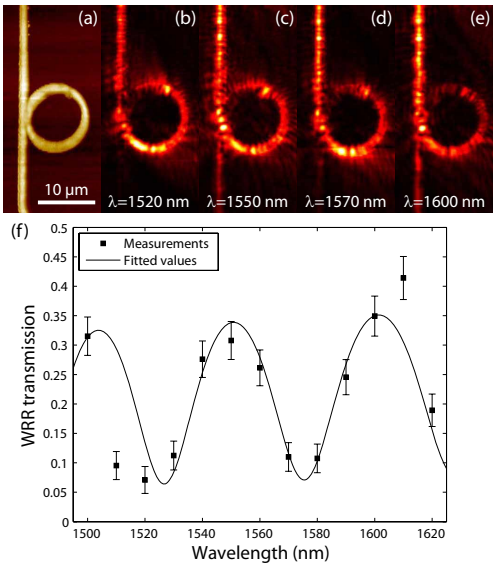

Fig. 4. (Color online) Transmission of a WRR with a gap of $g \simeq 0.3\ \mu$m. (a) Topographical image recorded with the SNOM. [(b)-(e)] Near-field optical images of the WRR for the wavelengths $\lambda = 1520$ nm, $\lambda = 1550$ nm, $\lambda = 1570$ nm, and $\lambda = 1600$ nm, respectively. (f) Measured WRR transmission along with an analytical fit obtained from Eq. (1).

surface. Characterization of the fabricated WRRs with a SNOM imaging system, at telecommunication wavelengths, shows a strong coupling to the ring resonator for waveguide-ring gaps smaller than $\sim 0.5\ \mu$m, whereas gap sizes larger than $\sim 1.5\ \mu$m does not give rise to any noticeable coupling to the ring resonator. Near-field characterization of a $g \simeq 0.5\ \mu$m WRR with a designed ring radius of $R = 5\ \mu$m reveals an extinction ratio of ~ 13 dB and transmission bandwidth of ~ 20 nm, giving promise of realization of very effective band selective filters based on DLSPPWs. Characterization of a $g \simeq 0.3\ \mu$m WRR reveals a much stronger coupling to the ring resulting in lower transmission values and smaller extinction ratio, whereas a $g \simeq 0.0\ \mu$m WRR, i.e., waveguide-ring intersection, shows weak coupling due to the change in coupling mechanism. A good correspondence is found between measured transmission values and values obtained from an analytical expression for the transmission. This expression explains the features of each WRR well, with regard to coupling to the ring and attenuation in the resonator, and can thus be used in the design of WRRs to obtain the desired bandwidth and extinction ratio.

Acknowledgments

The authors thank Thomas Søndergaard for help in developing a multilayer waveguide program used in this work. The financial support of the EC FP6 STREP PLASMOCOM (IST 034754) is acknowledged.

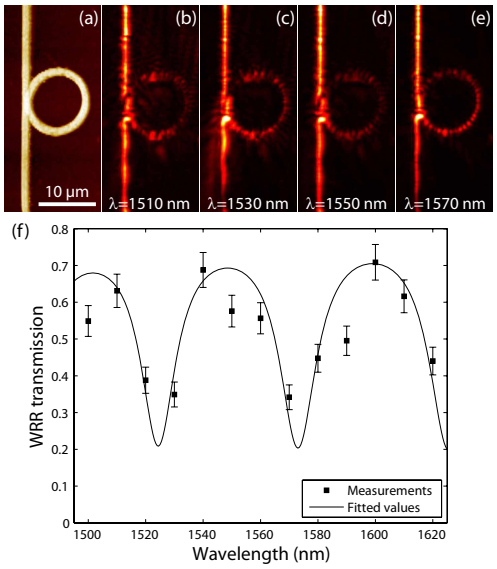

Fig. 5. (Color online) Transmission of a WRR with a gap of $g \simeq 0.0$ μm, i.e., intersection between waveguide and ring. (a) Topographical image recorded with the SNOM. [(b)-(e)] Near-field optical images for the wavelengths $\lambda = 1510$ nm, $\lambda = 1530$ nm, $\lambda = 1550$ nm, and $\lambda = 1570$ nm, respectively. (f) Measured and fitted WRR transmission.

Appendix G

Opt. Lett. **34**, 2009

Z. Chen, T. Holmgaard, S. I. Bozhevolnyi, A. V. Krasavin, A. V. Zayats, L. Markey, and A. Dereux, *"Wavelength-selective directional coupling with dielectric-loaded plasmonic waveguides"*, Opt. Lett. **34**, 310-312 (2009).

Wavelength-selective directional coupling with dielectric-loaded plasmonic waveguides

Zhuo Chen,[1] Tobias Holmgaard,[1] Sergey I. Bozhevolnyi,[1,2,*] Alexey V. Krasavin,[3] Anatoly V. Zayats,[3] Laurent Markey,[4] and Alain Dereux[4]

[1]*Department of Physics and Nanotechnology, Aalborg University, Skjernvej 4A, DK-9220 Aalborg Øst, Denmark*
[2]*Institute of Sensors, Signals and Electrotechnics (SENSE), University of Southern Denmark, Niels Bohrs Allé 1, DK-5230 Odense M, Denmark*
[3]*Centre for Nanostructured Media, International Research Centre for Experimental Physics, The Queen's University of Belfast, Belfast BT7 1NN, United Kingdom*
[4]*Institut Carnot de Bourgogne, UMR 5209 CNRS—Université de Bourgogne, 9 Avenue A. Savary, BP 47 870, F-21078 Dijon CEDEX, France*
**Corresponding author: seib@sense.sdu.dk*

Received November 10, 2008; revised December 18, 2008; accepted December 18, 2008; posted December 22, 2008 (Doc. ID 103903); published January 26, 2009

We consider wavelength-selective splitting of radiation using directional couplers (DCs) formed by dielectric-loaded surface-plasmon-polariton waveguides (DLSPPWs). The DCs were fabricated by depositing subwavelength-sized polymer ridges on a gold film using large-scale UV photolithography and characterized at telecommunications wavelengths with near-field microscopy. We demonstrate a DLSPPW-based 45-μm-long DC comprising 3 μm offset S bends and 25-μm-long parallel waveguides that changes from the "through" state at 1500 nm to 3 dB splitting at 1600 nm, and show that a 50.5-μm-long DC should enable complete separation of the radiation channels at 1400 and 1620 nm. The DC performance is found to be in good agreement with full vectorial three-dimensional finite-element simulations. © 2009 Optical Society of America

OCIS codes: 240.6680, 130.3120, 130.5460.

Surface-plasmon polaritons (SPPs), light waves coupled to free-electron oscillations in metal [1], can be laterally confined below the diffraction limit using subwavelength metal structures [2]. Plasmonic components open an appealing perspective of combining the high operational bandwidth of photonic components with the subwavelength dimensions of SPP waveguides [1,2]. Recently developed dielectric-loaded SPP waveguides (DLSPPWs), utilizing high effective indexes of SPP modes guided by dielectric ridges on smooth metal films [3–7], represent an attractive alternative to other plasmonic technologies by virtue of being naturally compatible with different dielectrics and large-scale industrial fabrication using UV lithography [8–10]. Preliminary investigations indicated that DLSPPW-based components feature relatively low bend and propagation losses [9,10], but their potential for wavelength selection, a crucial functionality for any photonic circuit, has so far not been explored.

Wavelength-selective plasmonic components generally feature more complicated geometry [2], thereby imposing additional requirements to the accuracy of fabrication. In our case, one should also bear in mind a (diffraction) limited resolution of UV lithography [9] employed for the DLSPPW fabrication. Taking into account a rather good performance of recently investigated DLSPPW-based S bends [9], we suggest making use of wavelength-dependent behavior of directional couplers (DCs) [11] for the selection and spatial separation of radiation channels at different wavelengths. Note that the wavelength dispersion of directional coupling using DLSPPWs has not been considered in previous publications [6,7]. Here we report on the fabrication, characterization, and modeling of DLSPPW-based wavelength-selective DCs operating at telecommunication wavelengths.

All waveguide structures were fabricated using deep UV lithography (wavelength of ~250 nm) with a Süss Microtech MJB4 mask aligner in the vacuum contact mode and a ~550 nm thick layer of polymethyl-methacrylate (PMMA) resist spin coated on a 60 nm thin gold film, which was supported by a thin glass substrate. Typically, the width of the produced waveguides, inspected with scanning electron microscopy (SEM), was close to 500 nm ensuring the single-mode (and close to optimum) DLSPPW operation [5]. The performance of the fabricated components was characterized using a scanning near-field optical microscope (SNOM), operating in collection mode with an uncoated fiber tip used as a probe, and an arrangement for SPP excitation (at $\lambda = 1500-1620$ nm) in the Kretschmann–Raether configuration, as described in detail elsewhere [10]. All waveguide structures were connected to funnel structures [Fig. 1(a)], facilitating efficient excitation of the DLSPPW mode [8], with the further improvement in that the DLSPPW mode was excited directly inside the taper by matching the excitation angle (under total internal reflection), resulting in SNOM images of high quality [9,10]. We found that all structures exhibited the DLSPPW propagation length of ~50 μm, slightly increasing with the wavelength [10].

Several DLSPPW-based 45-μm-long DCs, comprising 3 μm offset, 10-μm-long (input and output) S bends, having different center-to-center separations, $S = 800$, 900, and 1000 nm, between 25-μm-long parallel waveguides were fabricated and characterized with the SNOM at different wavelengths (Fig. 1). It

0146-9592/09/030310-3/$15.00

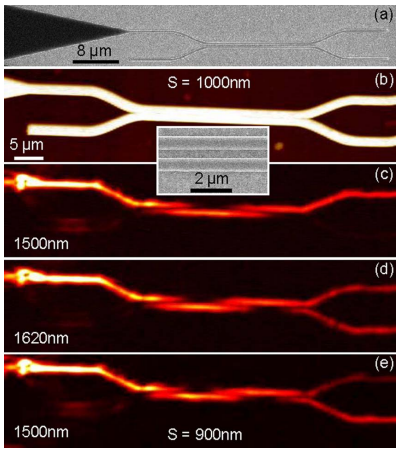

Fig. 1. (Color online) (a) Scanning electron microscope image of the fabricated DC showing the funnel structure facilitating the DLSPPW excitation. (b) Topographical and (c)–(e) near-field optical [λ=(c) 1500, (d) 1620, and (e) 1500 nm] SNOM images of 45 μm long DCs with the separations (b)–(d) $S=1000$ nm along with an inset showing SEM image of the coupling region and (e) $S=900$ nm.

was observed that the coupling length l_c (i.e., the interaction length needed to completely transfer the power from one waveguide to another) depends strongly on the separation [Figs. 1(c) and 1(e)] and varies noticeably with the wavelength, influencing the power level in the output waveguides [Figs. 1(c) and 1(d)]. At the same time, the total DC transmission evaluated using the input and output waveguide cross sections (separated by $L=45$ μm) is practically wavelength independent maintaining the level of ~0.23, a value that is consistent with the loss incurred by 25-μm-long propagation (~40%) and two S bends (~35% per bend) [9]. One can thereby conclude that the performance of the fabricated DCs is not degraded owing to fabrication errors, an important circumstance that is achieved because the DC design does not contain critical elements requiring high-resolution lithography.

To get further insight into the DLSPPW-based DC operation, we conducted full three-dimensional finite-element method (3D-FEM) simulations of the DC operation [6] that allowed us to retrieve the coupling length dispersion. It is seen that the simulation results agree well with the experimental values obtained directly from the SNOM images (Fig. 2). This dispersion was used to calculate the normalized output signals, i.e., straight T_s and cross T_c transmissions, with only one waveguide being excited at the input,

$$T_{s,c}(\lambda) = (T_{\text{bend}})^2 \exp\left(-\frac{L_p}{L_{SP}}\right)\left\{\begin{matrix}\cos^2\left(\dfrac{\pi L_i}{2l_c(\lambda)}\right)\\ \sin^2\left(\dfrac{\pi L_i}{2l_c(\lambda)}\right)\end{matrix}\right\}, \quad (1)$$

where the first factor reflects the S-bend transmission, the second one reflects the power loss incurred

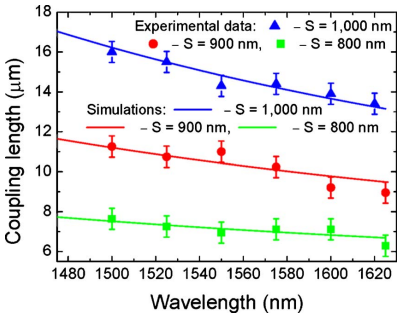

Fig. 2. (Color online) DC coupling length evaluated for different wavelengths and separations directly from SNOM images similar to those shown in Figs. 1(c)–1(e) and calculated with 3D-FEM simulations.

by the propagation through the section of parallel waveguides (of length L_p), and L_i denotes the effective interaction length; typically, $L_i > L_p$ due to the additional mode coupling in the S bends [11]. Using the already known parameters, $T_{\text{bend}} \sim 0.65$ (evaluated using the available experimental data [9]), $L_p = 25$ μm and $l_c(\lambda)$ for $S=1000$ nm (Fig. 2), we found that the interaction length $L_i \cong 34$ μm results in good agreement (Fig. 3) between the calculated [Eq. (1)] output signals and the values obtained from SNOM images, similar to those shown in Fig. 1. Using the obtained results one can *design* a DC structure that would ensure spatial separation of radiation corresponding to different bands used in optical telecommunications. For example, an increase of the length of parallel section by ≅5.5 μm for the DC with $S=1000$ nm would enable spatial separation of the wavelengths of 1400 and 1620 nm (belonging to E and L bands) as seen from the calculations using Eq. (1) with $L_p=30.5$ μm and $L_i \cong 39.5$ μm (Fig. 3).

In conclusion, we have considered the usage of DC wavelength dispersion for the selection and spatial

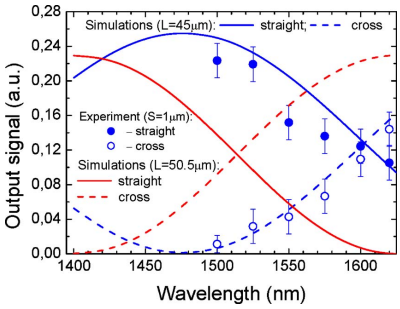

Fig. 3. (Color online) DC output signals normalized with respect to the input when exciting only one waveguide, determined experimentally from SNOM images similar to those shown in Figs. 1(c)–1(e) and calculated using Eq. (1) and the DC coupling length dispersion shown in Fig. 2.

separation of radiation channels at different wavelengths. Using industrially compatible large-scale UV-lithography-based fabrication and exploiting the principles of DLSPPW-based plasmonic technology, we have fabricated and characterized wavelength-selective DCs operating at telecommunications wavelengths. We have demonstrated a DLSPPW-based 45-μm-long DC comprising 3 μm offset S bends and 25-μm-long parallel waveguides that changes from the through state at 1500 nm to 3 dB splitting at 1600 nm and have shown that a 50.5-μm-long DC should enable complete separation of the radiation channels at 1400 and 1620 nm (belonging to E and L bands). The performance of the considered structures could be further improved by fine tuning the DC parameters so as to achieve overall optimization (e.g., with the 3D-FEM simulations) with respect to the wavelength selection and insertion loss. Taking into account the fact that this technology is naturally compatible with different dielectrics, one can envisage the development of ultracompact plasmonic components utilizing thermo-optical, electro-optical, magneto-optical, acousto-optical, and nonlinear optical effects as well as being integrated with electrical circuits.

This work was supported by EC FP6 STREP PLASMOCOM. A. V. Krasavin and A. V. Zayats also acknowledge the financial support from the Engineering and Physical Sciences Research Council (EPSRC) (UK).

References

1. W. L. Barnes, A. Dereux, and T. W. Ebbesen, Nature **424**, 824 (2003).
2. T. W. Ebbesen, C. Genet, and S. I. Bozhevolnyi, Phys. Today **61**, 44 (May 2008).
3. C. Reinhardt, S. Passinger, B. N. Chichkov, C. Marquart, I. P. Radko, and S. I. Bozhevolnyi, Opt. Lett. **31**, 1307 (2006).
4. B. Steinberger, A. Hohenau, H. Ditlbacher, A. L. Stepanov, A. Drezet, F. R. Aussenegg, A. Leitner, and J. R. Krenn, Appl. Phys. Lett. **88**, 094104 (2006).
5. T. Holmgaard and S. I. Bozhevolnyi, Phys. Rev. B **75**, 245405 (2007).
6. A. V. Krasavin and A. V. Zayats, Appl. Phys. Lett. **90**, 211101 (2007).
7. B. Steinberger, A. Hohenau, H. Ditlbacher, F. R. Aussenegg, A. Leitner, and J. R. Krenn, Appl. Phys. Lett. **91**, 081111 (2007).
8. T. Holmgaard, S. I. Bozhevolnyi, L. Markey, and A. Dereux, Appl. Phys. Lett. **92**, 011124 (2008).
9. T. Holmgaard, Z. Chen, S. I. Bozhevolnyi, L. Markey, A. Dereux, A. V. Krasavin, and A. V. Zayats, Opt. Express **16**, 13585 (2008).
10. T. Holmgaard, S. I. Bozhevolnyi, L. Markey, A. Dereux, A. V. Krasavin, P. Bolger, and A. V. Zayats, Phys. Rev. B **78**, 165431 (2008).
11. A. Boltasseva and S. I. Bozhevolnyi, IEEE J. Sel. Top. Quantum Electron. **12**, 1233 (2006).

Appendix H

J. Lightwave Technol. (submitted), 2009

T. Holmgaard, Z. Chen, S. I. Bozhevolnyi, L. Markey, and A. Dereux, *"Design and characterization of dielectric-loaded plasmonic directional couplers"*, J. Lightwave Technol. (submitted) (2009).

Design and characterization of dielectric-loaded plasmonic directional couplers

Tobias Holmgaard, Zhuo Chen, Sergey I. Bozhevolnyi, Laurent Markey, and Alain Dereux

***Abstract*—Ultra-compact directional couplers (DCs), based on dielectric-loaded surface plasmon-polariton waveguides (DLSPPWs) are analyzed using the effective index method (EIM) with the coupling both in the parallel interaction region and in- and out-coupling regions being taken into account. Near-field characterization of fabricated DCs performed with a scanning near-field optical microscope verifies the applicability of the EIM in the analysis and design of DLSPPW-based wavelength selective DCs. The design approach applicable to a large variety of integrated optical waveguides is developed enabling the realization of DCs, in which optical signals at two different wavelengths are coupled into two separate output channels. The developed approach ensures minimization of the cross-talk and overall DC length via simultaneous adjustment of the waveguide separation and length of the interaction region. As an example, the design of a DLSPPW-based DC for complete separation of telecommunication signals at the wavelengths $\lambda = 1400$ nm and $\lambda = 1600$ nm between two output channels separated by 6 μm is worked out resulting in the total device length of 52.3 μm. In addition, the design of an ultra-compact DLSPPW-based DC waveguide crossing that ensures a very low cross-talk over a large wavelength band in the telecommunication range is considered.**

***Index Terms*—Directional couplers, dielectric-loaded waveguides, surface plasmons, integrated optics devices**

I. Introduction

THE recent intensification of the research in nanophotonics is, among other things, motivated by the expectation of realizing compact nanophotonic integrated circuits, where the asset of electronics, with regard to component size, is combined with the asset of photonics, with regard to operational bandwidth. In order to realize compact devices, several essential components are necessary, among which are single-mode waveguides with strong confinement, waveguide bends and splitters, waveguide crossings, and wavelength selective components for filtering and separation of wavelengths. Such wavelength selective components are essential in the realization of demultiplexing components and could be based on, e.g., waveguide-ring resonators (WRRs) or directional couplers (DCs). Some of the most promising technologies to achieve compact nanophotonic circuits are based on plasmonics, i.e., surface plasmon polaritons (SPP). SPPs are collective waves in the surface plasma of a metal coupled to light waves [1], [2]. The SPPs are transverse magnetic in nature, are bound to, and propagate along the interface between a metal and a dielectric, with a field maximum right at the interface, and an exponential decay away from it. SPPs typically penetrate in the order of tens of nanometers in the metal, and hundreds of nanometers in the dielectric, and thus feature a strong intrinsic confinement in the direction perpendicular to the metal-dielectric interface [3]. When designing plasmonic waveguides it is thus important to achieve a strong lateral confinement in order to minimize radiation losses when bending the waveguide, and to maximize the integration of plasmonic components. Due to the metal involved, another challenge in the design is to minimize the propagation losses, while retaining the demand of single-mode propagation and strong confinement. Several different plasmonic waveguide structures seeking to obey these demands have been proposed and investigated in the recent years, among which are V shaped and rectangular grooves in an otherwise smooth metal film [4], [5], [6], thin metal stripes embedded in a dielectric [7], [8], and chains of closely spaced metal nanoparticles [9], [10]. The possibility of realizing wavelength dependent components and in particular directional coupling with these types of plasmonic waveguides has also recently been investigated by several research groups [11], [12], [13], [14], [15], [16], [17], [18], [19].

Another promising, and technologically simple, approach to achieve strong lateral confinement with plasmonic waveguides is to utilize dielectric ridges deposited on a smooth metal film as high-index contrast waveguides [20], [21]. This type of plasmonic waveguides are attractive due to the fabrication method, which is compatible with large scale industry lithography, and the versatility offered by the choice of dielectric used as the ridge guides. Extensive theoretical [22], [23], [24], [25] and experimental [26], [27], [28] research have confirmed the promise of realizing single-mode waveguides with strong confinement, compact bends, splitters, and wavelength selective components such as Bragg filters and WRRs [29], [30], and in addition to this, DCs have also been fabricated and characterized [31], [32]. However, it still remains to be seen how DCs can be utilized to obtain physical separation of two wavelengths, needed for realizing a demultiplexer, and to achieve low cross-talk waveguide crossings. In this work we present effective index method (EIM) calculations of DLSPPW based DCs along with scanning near-field optical microscope (SNOM) measurements performed on fabricated

The financial support of the EC FP6 STREP PLASMOCOM (IST 034754) is acknowledged.

T. Holmgaard and Z. Chen are with the Department of Physics and Nanotechnology, Aalborg University, DK-9220 Aalborg Øst, Denmark (e-mail: holmgaard@nano.aau.dk).

S. I. Bozhevolnyi is with the Institute of Sensors, Signals, and Electrotechnics (SENSE), University of Southern Denmark, DK-5230 Odense M, Denmark and the Department of Physics and Nanotechnology, Aalborg University, DK-9220 Aalborg Øst, Denmark.

L. Markey and A. Dereux are with the Institut Carnot de Bourgogne, UMR 5209 CNRS-Université de Bourgogne, F-21078 Dijon Cedex, France.

DCs, which verify the validity of the EIM in the analysis of the DCs. Furthermore, approaches for designing DCs capable of physically separating two specific wavelengths and DCs which offer the possibility of crossing two waveguides are proposed, and application examples are presented.

The paper is organized as follows. In Sec. II the DLSPPW structure is introduced, the DC layout is presented, and a description of the EIM used in the analysis and design of DCs is given. In Sec. III a brief description of the experimental setup for performing near-field measurements is given, and results obtained from near-field optical images of fabricated DCs are compared to EIM calculations. In Sec. IV a DC design approach is introduced, and design examples are given based on the DLSPPW technology. In Sec. V a discussion of the obtained results is presented and we offer our conclusions.

II. EIM CALCULATIONS

In guided-wave photonics there are generally two approaches to analyze DCs. The coupled-mode approach, where the presence of a second identical waveguide is included by considering it a perturbation to the unperturbed field profiles associated with a mode incident in the first waveguide, and the super-mode approach, where the phase difference between the two modes supported by the entire structure is considered. The coupled-mode approach has the advantage of being computationally simple, however, since the field profiles used in the calculation of the coupling are those of two waveguides in isolation, they are approximations valid for weak coupling only, i.e., large separation between the waveguides [33]. This is not the case for the plasmonic DCs considered in this work, and thus the super-mode approach is applied in the following.

The DCs investigated in this work basically consists of four sections, being the DLSPPW mode excitation region, in the form of a funnel, an in-coupling S-bend bringing the two waveguides into close proximity, a parallel interaction region, and an out-coupling S-bend separating the two waveguides again [Fig. 1(a)]. In the notation used throughout, the initial and final center-to-center separation of the two waveguides is $2d_0 + S_0$, the separation at the parallel section is S_0, the length of the parallel section is L_p, and the length of the S-bends is x_s. The S-bends are based on cosine curves, where the center-to-center separation is given as

$$S(x) = S_0 + d_0 \left[1 + \cos\left(\frac{\pi x}{x_\mathrm{s}}\right)\right], \tag{1}$$

in the case of the in-coupling S-bend ($x = 0$ at the beginning of the bend). The DLSPPWs consists of a rectangular dielectric ridge of height h, width w, and refractive index n_2 deposited on a metal film of refractive index n_3, and bound by air, n_1, above [Fig. 1(b)].

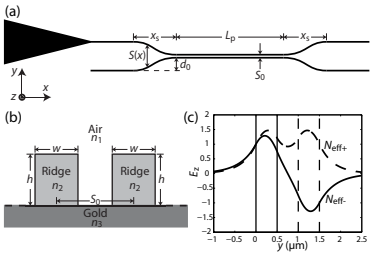

Fig. 1. DC layout and design parameters. (a) DC layout consisting of a funnel used for exciting DLSPPWs in the experiments, an S-bend "in-coupling" region, a parallel interaction section where the waveguide modes overlap, and an S-bend "out-coupling" region. (b) Cross-sectional view of the DC at the interaction region, where the center-to-center separation of the two waveguides is S_0. (c) Cross-sectional profile of the EIM calculated symmetric ($N_{\mathrm{eff}+}$) and anti-symmetric ($N_{\mathrm{eff}-}$) DLSPPW modes supported by the DC structure.

The EIM has previously proved to be accurate and reliable in the description of straight DLSPPWs and DLSPPW components [22], [27], [30] and is thus expected to describe the behavior of DLSPPW based DCs well. In the EIM the problem of finding eigenmodes in a two dimensional geometry is reduced to consecutively solving two one-dimensional eigenmode problems, which can be done straightforwardly with a multilayer waveguide solver. When considering DCs, the first step in the EIM calculation is to find the mode effective index of a three layer air-dielectric-metal geometry with infinite height of the air and metal layer, and height h of the dielectric layer, corresponding to setting $w \sim \infty$. In this calculation p-polarized modes are assumed, corresponding to SPP modes. The mode effective index found in this calculation is then used to represent the two waveguide regions of width w in the second step. Outside these regions the mode effective index of a SPP propagating along a smooth metal film with air above is used. This five layer geometry is then solved for s-polarized modes, and a symmetric ($N_{\mathrm{eff}+}$) and anti-symmetric ($N_{\mathrm{eff}-}$) mode is found [Fig. 1(c)]. These two modes are orthogonal and uncoupled, thus if the propagation losses are ignored, the only effect on the modes due to propagation over a distance L, is the phase shift

$$\phi_\pm = k_0 N_{\mathrm{eff}\pm} L = \frac{2\pi}{\lambda} N_{\mathrm{eff}\pm} L, \tag{2}$$

where λ is the vacuum wavelength. When the accumulated phase difference between the two modes $\Delta\phi = \phi_+ - \phi_-$ reaches a value of π the mode power has shifted completely from one waveguide to the other. The length corresponding to this shift is denoted the coupling length L_c and can be found as

$$\Delta\phi = \frac{2\pi}{\lambda} \Delta N_\mathrm{eff} L_\mathrm{c} = \pi \Rightarrow L_\mathrm{c} = \frac{\lambda}{2\Delta N_\mathrm{eff}}. \tag{3}$$

Where $\Delta N_\mathrm{eff} = N_{\mathrm{eff}+} - N_{\mathrm{eff}-}$. Thus knowing the dependencies of the effective indexes of the symmetric and anti-symmetric modes on, e.g., wavelength and waveguide separation, one can analyze the coupling properties of the DC.

In the EIM calculations gold is used for the metal film, which is considered optically thick, with the complex refractive index taken from [34]. The dielectric used is polymethylmethacrylate (PMMA) with refractive index $n_2 = 1.493$, $h = 600$ nm, and $w = 500$ nm, which are found to be the optimum dimensions at telecommunication wavelengths [22]. By varying the gap between the two waveguides in the calculation, a dependence on S_0 can be established [Fig. 2].

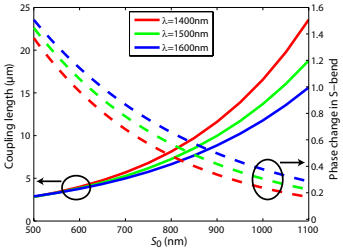

Fig. 2. (Color online) Coupling length and phase change in S-bend dependence on final waveguide separation (S_0) calculated utilizing the EIM. In the calculations the waveguide dimensions $h = 600$ nm and $w = 500$ nm are assumed. In the phase change calculation the S-bend parameters $d_0 = 3$ μm and $x_s = 10$ μm are used.

For a DC where the two waveguides are brought into contact with one another, i.e., $S_0 = w$, a very short coupling length with weak dependence on wavelength is expected as most of the mode power is concentrated inside the double width waveguide. However, in general the coupling lengths are expected to be larger for shorter wavelengths due to the better confinement to the ridge, and thus less coupling to an adjacent ridge. An increase in S_0 increases the coupling length exponentially, as the DLSPPW mode fields decrease exponentially outside the ridge. These trends are confirmed in the EIM calculations of the coupling length [Fig. 2].

When extending the calculations to considering coupling between the two waveguides in the S-bends, with non-uniform separation between the waveguides, a slightly modified approach is needed. In order to find the phase change due to coupling in the S-bend, a dependence of the coupling constant κ, given as

$$\kappa = \frac{\pi}{2L_c} = \frac{\pi \Delta N_{\text{eff}}}{\lambda}, \tag{4}$$

on the separation $S(x)$ must be established by means of the EIM. As the coupling length shows an exponential dependence on S, so does κ, and by fitting the EIM results of κ, the analytical expression

$$\kappa(S) = A \exp(BS) \tag{5}$$

can be established, with A and B being wavelength dependent factors. Using this, and the expression for the waveguide separation throughout the S-bend given by Eq. 1, the phase change due to an S-bend can be found as

$$\Delta\phi_s = 2 \int_0^{x_s} \kappa\left(S(x)\right) \mathrm{d}x. \tag{6}$$

Solving this equation, using the S-bend parameters $d_0 = 3$ μm and $x_s = 10$ μm (used in the fabricated DC samples), confirms that the coupling increases with wavelength, but decreases exponentially with S_0 [Fig. 2] as was the case in the parallel section. The results clearly illustrate the importance of including the coupling between the waveguides in the in- and out-coupling S-bends, particularly for small S_0 values.

Once established, the analytical approach to finding the phase change due to the S-bends, can easily by adapted to different S-bend parameters. Finding the phase change for several different initial separations $S(0) = 2d_0 + S_0$ ranging from barely decoupled [23] waveguides ($S(0) = 2.5$ μm) to large separation ($S(0) = 12.5$ μm) illustrates the importance in choice of initial waveguide offset values (d_0) [Fig. 3]. As expected from the above results, the coupling in the S-

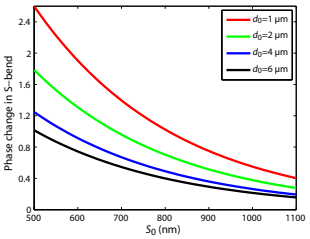

Fig. 3. (Color online) Phase change in S-bend dependence on S_0 for different initial waveguide offset values of the S-bend (d_0), calculated at the wavelength $\lambda = 1500$ nm.

bend has an exponential dependence on initial waveguide separation. The large influence of the S-bend on the total device performance is clearly illustrated by contemplating the case when $S_0 = 500$ nm and $d_0 = 1$ μm, where $\Delta\phi_s \simeq 2.6$ corresponding to a $\sim 90\%$ shift of mode energy to the cross arm (a complete shift corresponds to $\Delta\phi = \pi$).

By being able to describe the coupling in the parallel interaction region and in the in- and out-coupling S-bends, one is able to analyze the performance of the whole DC device and thus being able to describe the influence of the wavelength, the initial separation, the separation in the parallel section, and the length of the parallel section. The total accumulated phase difference can be calculated as

$$\Delta\phi_{\text{tot}} = 2\Delta\phi_s + \pi \frac{L_p}{L_c}, \tag{7}$$

where the first term is related to the two S-bends and the second term to the parallel section.

III. Near-field characterization

In order to validate the applicability of the EIM in the analysis of DLSPPW based DCs, the above results are compared to results obtained from fabricated DC structures, by application of a SNOM. The samples are fabricated using deep-UV lithography, at a wavelength of 250 nm, with a Süss Microtech MJB4 mask aligner in the vacuum contact mode. A layer of PMMA resist is spin coated on a thin gold film ($t \simeq 60$ nm) deposited on a supporting glass substrate, and the structures are written using a commercially fabricated mask. The height of the DLSPPWs, as investigated with an atomic force microscope (AFM) is found to be $h \simeq 550$ nm, and the width, as investigated with a scanning electron microscope (SEM), found to be $w \simeq 500$nm, which ensures close to optimum performance [22]. The thickness of the gold film is chosen in order to allow for DLSPPW excitation from below, using the Kretschmann-Raether configuration [2], while keeping the propagation losses, due to radiation back

into the glass substrate, as low as possible. By depositing the sample substrate on a high-index prism using index matching immersion oil, and focusing a Gaussian beam to a spot size of ~ 15 μm on the bottom interface of the gold film, just below the excitation funnel [Fig. 1(a)], the mode index of DLSPPs in the funnel is matched. Topographical and near-field optical images of the fabricated DCs are collected using a SNOM, operating in collection mode, by raster scanning a tapered uncoated fiber tip across the sample surface.

The DC structures are fabricated using the S-bend parameters $d_0 = 3$ μm and $x_s = 10$ μm while varying S_0. The length of the parallel section is kept constant $L_p = 25$ μm. The recorded topographical images confirms the fabrication of DCs of high quality with a very low degree of defects [Fig. 4(a)], and the near-field optical images shows the coupling between the straight (the one excited) and cross arm [Fig. 4(b)-(e)]. The

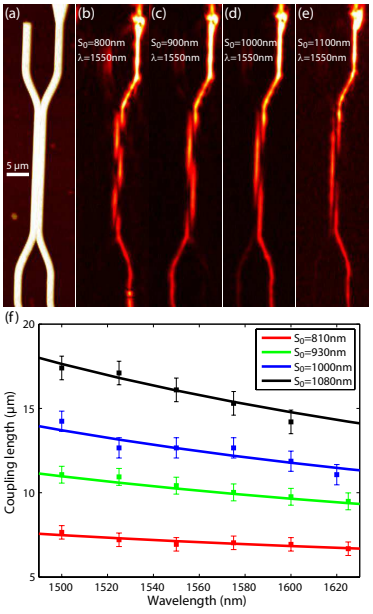

Fig. 4. (Color online) Coupling length dependence on wavelength and waveguide separation. (a) Topographical ($S_0 = 1000$ nm) and [(b)-(e)] near-field optical (at $\lambda = 1550$ nm) images of DCs measured with a SNOM. (b) $S_0 = 800$ nm, (c) $S_0 = 900$ nm, (d) $S_0 = 1000$ nm, and (e) $S_0 = 1100$ nm. (f) Coupling length as a function of wavelength measured with the SNOM (squares) along with EIM calculated dependence (lines) fitted to the measurements by slight adjustment of S_0.

propagation losses observed in the near-field optical images are found in good correspondence to previous observations of DLSPPW structures exhibiting the mode propagation length of ~ 50 μm [27]. The rapid increase in coupling length with separation is clearly observed in the recorded near-field images, and by performing a wavelength scan of each of the DCs, the dispersion with respect to wavelength can be found. By determining the coupling lengths from profiles of the near-field optical images, and finding the best fit of EIM calculated curves (fitting S_0) it is observed that the EIM describes the behavior of the DCs with regard to separation and wavelength well [Fig. 4(f)].

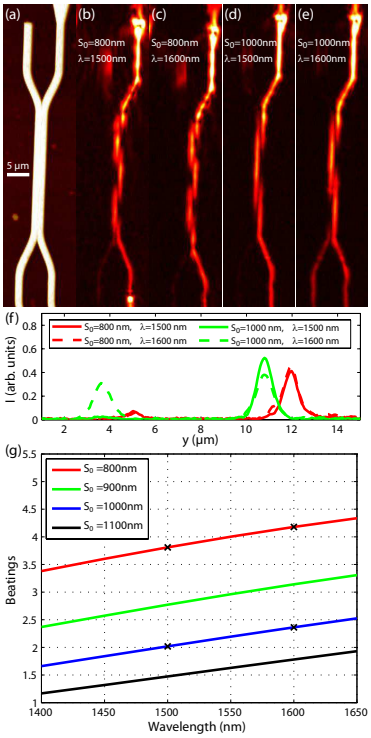

Fig. 5. (Color online) Near-field investigation and EIM calculation of number of beatings in DCs with different waveguide separations. (a) Topographical ($S_0 = 1000$ nm) and near-field optical [(b)-(e)] images of DCs measured with a SNOM. (b) $S_0 = 800$ nm and $\lambda = 1500$ nm, (c) $S_0 = 800$ nm and $\lambda = 1600$ nm, (d) $S_0 = 1000$ nm and $\lambda = 1500$ nm, and (e) $S_0 = 1000$ nm and $\lambda = 1600$ nm. (f) Cross-sectional profiles of the near-field optical images (b)-(e) taken at the DC output, i.e., after the separation of the waveguides. (g) EIM calculation (lines) of the total number of beatings throughout the DCs (including the two S-bends) as a function of wavelength, with parameters identical to those used in the design of the fabricated sample. The four cases investigated with the SNOM shown in the near-field images (b)-(e) are marked with crosses.

Observing the performance of one of the fabricated DCs with $S_0 = 800$ nm, by contemplation of the near-field images at two different wavelengths $\lambda = 1500$ nm [Fig. 5(b)] and $\lambda = 1600$ nm [Fig. 5(c)], shows that although the coupling is different at the two wavelengths, the output of the DC is more or less identical [Fig. 5(f)]. Note that the bright spot at the output of the straight arm is caused by scatting due to a defect, which occurred during near-field investigation. This performance is in strong contrast to the performance of another

of the fabricated DCs with $S_0 = 1000$ nm. In this case close to all of the mode power is transmitted through the straight arm at $\lambda = 1500$ nm [Fig. 5(d)], whereas a 50/50 splitting occurs at $\lambda = 1600$ nm [Fig. 5(e)], which is clearly illustrated by the cross-sectional profiles at the DC output [Fig. 5(f)]. Inclusion of the S-bends in the EIM calculation enables the calculation of the total number of beatings throughout the whole DC, which can easily be compared to the near-field optical images, and explain the above observation. The total number of beatings is found by using Eq. 7 to calculate the total phase change in the DC, and dividing by π [Fig. 5(g)]. An even number of beatings means transmission trough the straight arm, whereas an odd number of beatings results in transmission through the cross arm. From the EIM results it is clear that the $S_0 = 800$ nm curve intersects 4 beatings at $\lambda = 1550$ nm, i.e., in the middle of the band bound by $\lambda = 1500$ nm and $\lambda = 1600$ nm, and thus here transmits all mode power in the straight arm (see Fig. 4(b)). In the case of the $S_0 = 1000$ nm DC, however, the curve intersects 2 beatings right at $\lambda = 1500$. This clearly demonstrates need for careful design, when applying DCs for physical separation of different wavelengths, as the the output from the $S_0 = 800$ nm DC is the same at $\lambda = 1500$ nm and $\lambda = 1600$ nm. In addition the results presented in Fig. 5 show a good correspondence between EIM calculations and the results obtained by performing SNOM measurements on fabricated DC structures, thus confirming that the EIM is applicable in the analysis of DCs based on DLSPPWs.

IV. Design

Having established a valid method for analysis of DLSPPW based DCs enables design of different components necessary in the realization of compact photonic circuits. Two essential features in photonic circuits are wavelength selection, e.g., separating two wavelengths, and low cross-talk waveguide crossings. A design approach for each of these components is suggested in the following, and exemplified by application to the DLSPPW technology.

A. Wavelength selection

Physical separation of two distinct wavelengths propagating in the same multi-channel waveguide can be achieved with a DC by carefully designing the length of the parallel section L_p and the separation S_0. In order to achieve separation of two signals with the wavelengths λ_1 and λ_2, both incident in the straight channel, the total number of beatings through the DC at the two wavelengths B_1 and B_2 must be positive integers and the difference in beatings must be one,

$$1 = B_2 - B_1, \tag{8}$$

where it is assumed that $\lambda_1 < \lambda_2$. Expressing B_1 and B_2 in terms of L_p, L_c, and $\Delta\phi_\mathrm{s}$ using Eq. 7 yields

$$B_1 = \frac{L_\mathrm{p}}{L_\mathrm{c1}} + \frac{2\Delta\phi_\mathrm{s1}}{\pi}, \tag{9}$$

and

$$B_2 = \frac{L_\mathrm{p}}{L_\mathrm{c2}} + \frac{2\Delta\phi_\mathrm{s2}}{\pi}, \tag{10}$$

where L_c1 and $\Delta\phi_\mathrm{s1}$ depend on λ_1 and S_0, and L_c2 and $\Delta\phi_\mathrm{s2}$ depend on λ_2 and S_0 (assuming d_0 and x_s fixed). By insertion in Eq. 8 one can express the length of the parallel section in terms of the coupling lengths and phase changes in the S-bends as

$$L_\mathrm{p} = \frac{\left(1 - 2\frac{\Delta\phi_\mathrm{s2} - \Delta\phi_\mathrm{s1}}{\pi}\right)(L_\mathrm{c1} L_\mathrm{c2})}{L_\mathrm{c1} - L_\mathrm{c2}}. \tag{11}$$

Choosing the two wavelengths that must be separated in the DC, one can find the S_0 dependency of L_p. For small separations L_c1 approaches L_c2 [Fig. 2] and L_p thus increases rapidly as the denominator approaches zero. For large S_0, L_c1 and L_c2 increase exponentially and thus L_p increases rapidly also. Thus a minimum in L_p is expected and indeed found when plotting L_p versus S_0 for the choice of wavelengths $\lambda_1 = 1400$ nm and $\lambda_2 = 1600$ nm and the S-bend parameters $d_0 = 3$ μm and $x_\mathrm{s} = 10$ μm [Fig. 6]. Using Eq. 9 and

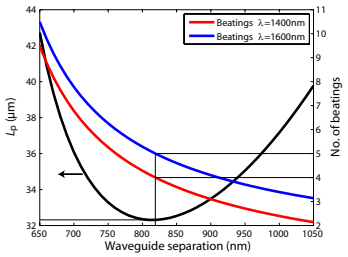

Fig. 6. (Color online) Illustration of the EIM design approach for achieving physical separation of the two wavelengths $\lambda_1 = 1400$ nm and $\lambda_2 = 1600$ nm. The length of the parallel section is shown as a function of the waveguide separation on the left y-axis, calculated using Eq. 11. The number of total beatings through the DC for the two wavelengths is plotted on the right y-axis as a function of waveguide separation using Eq. 9 and Eq. 10. The optimum (minimized device length) separation and length of parallel section is marked by the thin lines.

Eq. 10 one can now determine the number of beatings at the two wavelengths for each S_0 value. The design task is then simplified to choosing the B_1 value which makes the device as short as possible, and the optimum S_0 and L_p can be found. In the design example shown in [Fig. 6] $B_1 = 4$ is found to best match the minimum in L_p, yielding the optimum device parameters $S_0 = 819$ nm and $L_\mathrm{p} = 32.3$ μm giving a total device length $L_\mathrm{d} = 52.3$ μm (due to the two S-bends), which is comparable to the propagation length currently achieved with the DLSPPW technology [27]. It is thus illustrated that the design of very efficient wavelength separation components, with spectra similar to that of Fig. 3 in Ref. [32], is possible by utilizing the EIM in the analysis of DCs.

B. Waveguide crossing

Another essential integrated photonic component which can be realized with a DC is a waveguide crossing, where the signal incident in the straight channel is output to the cross channel, and visa versa. Strictly speaking the waveguides are not crossed, but the term waveguide crossing is used to emphasize that the result of this 100/0 coupler is the crossing

of the signals incident in the two waveguides. This implies that the total number of beatings must be a positive and odd integer at the desired wavelengths. In the case of perfect crossing (no cross-talk) of two channels transmitting at two distinct and different wavelengths it is furthermore a requirement that

$$2 = B_2 - B_1, \tag{12}$$

which results in an expression for the length of the parallel section as

$$L_\mathrm{p} = \frac{\left(2 - 2\frac{\Delta\phi_{\mathrm{s}2} - \Delta\phi_{\mathrm{s}1}}{\pi}\right)(L_{\mathrm{c}1}L_{\mathrm{c}2})}{L_{\mathrm{c}1} - L_{\mathrm{c}2}}. \tag{13}$$

This indicates a behavior with respect to S_0 similar to that shown above in Fig. 6, except of an offset toward longer parallel section due to the factor of 2 in the numerator. This is confirmed by performing a calculation of L_p for a waveguide crossing of two channels operating at $\lambda_1 = 1400$ nm and $\lambda_2 = 1600$ nm, and for the S-bend parameters $d_0 = 3$ μm and $x_\mathrm{s} = 10$ μm [Fig. 7]. Using the calculated waveguide

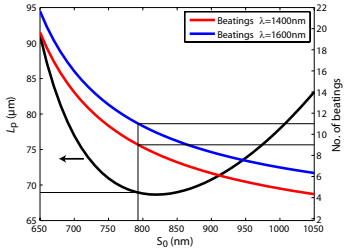

Fig. 7. (Color online) Design approach for realizing perfect waveguide crossing by means of a DC. The waveguide crossing is designed to perfectly, i.e., no cross-talk, cross two waveguides transmitting signals at the wavelengths $\lambda_1 = 1400$ nm and $\lambda_2 = 1600$ nm respectively. The length of the parallel section (L_p) is calculated using Eq. 13, and the number of beatings in the DC at the two wavelengths are calculated using Eq. 9 and Eq. 10. At the specified wavelengths the optimum DC parameters are $S_0 = 793$ nm and $L_\mathrm{p} = 68.9$ μm.

separation dependency of L_p one find the dependency of B_1 and B_2 on S_0 as above [Fig. 7], and it is evident that choosing $B_1 = 9$ results in as short a device as possible. The waveguide crossing design parameters for perfect crossing of two waveguides at $\lambda_1 = 1400$ nm and $\lambda_2 = 1600$ nm, respectively, is thus $S_0 = 793$ nm and $L_\mathrm{p} = 68.9$ μm, resulting in a total device length of $L_\mathrm{d} = 88.9$ μm. This quite long device length is excessive for many applications and in addition very specific, as only two distinct wavelengths can be crossed without cross-talk, and thus another design approach, slightly compromising the cross-talk, but decreasing the propagation losses, is considered in the following.

The task is thus to design a waveguide crossing which is short and with low cross-talk over a wide band of wavelengths. In the following design approach the telecommunication wavelength band of $\lambda = 1400$ nm-1600 nm is considered, and the S-bend parameters $d_0 = 3$ μm and $x_\mathrm{s} = 10$ μm used.

Due to the dispersion of the coupling length with wavelength, cross-talk in a wide band waveguide crossing is unavoidable, however, it can be minimized by carefully choosing the waveguide separation and device length. The shortest possible waveguide crossing which can be achieved with a DC is found by assuming that the wavelength band in each channel is identical, i.e., $\lambda_1 = \lambda_2$, and by setting the total number of beatings equal to one, indicating one shift of energy from the straight channel to the cross channel or visa versa

$$1 = \frac{L_\mathrm{p}}{L_\mathrm{c}} + \frac{2\Delta\phi_\mathrm{s}}{\pi}. \tag{14}$$

From this, an expression for L_p can be found as

$$L_\mathrm{p} = \left(1 - \frac{2\Delta\phi_\mathrm{s}}{\pi}\right) L_\mathrm{c}. \tag{15}$$

Due to the exponential decrease of $\Delta\phi_\mathrm{s}$ with S_0 and the exponential increase of L_c with S_0, L_p increases exponentially with waveguide separation, but decreases with wavelength [Fig. 8]. With regard to device length it is obviously preferable

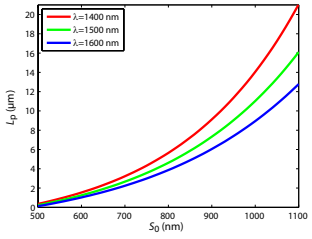

Fig. 8. (Color online) Length of parallel section in waveguide crossing of two channels with identical wavelength bands calculated by application of the EIM and Eq. 15. L_p is plotted versus center-to-center separation at the parallel section S_0 for the three wavelengths $\lambda = 1400$ nm, $\lambda = 1500$ nm, and $\lambda = 1600$ nm.

to have as small separation as possible, and it is interesting to observe that this is also the case with regard to cross-talk, as the difference in L_p for different wavelengths increases rapidly with increasing S_0. This means that it is unambiguously an advantage to keep S_0 as small as possible. To exemplify this, a waveguide crossing is designed for $\lambda = 1500$ nm, which is the center of the wavelength band $\lambda = 1400$ nm-1600 nm, by calculating L_p using Eq. 15 for the two waveguide separations $S_0 = 500$ nm, i.e., no gap, and $S_0 = 1100$ nm. At $S_0 = 500$ nm the length of the parallel section is calculated to be $L_\mathrm{p} = 0.23$ μm, and at $S_0 = 1100$ nm the length of the parallel section is calculated to be $L_\mathrm{p} = 16.1$ μm, yielding device lengths of $L_\mathrm{d} = 20.2$ μm and $L_\mathrm{d} = 36.1$ μm respectively. The normalized mode power transmission, i.e., ignoring propagation and bend losses, in the straight and cross arm respectively, with incident signal in the straight arm only, is calculated using

$$T_{\mathrm{s,c}}(\lambda) = \begin{cases} \cos^2\left[\Delta\phi_\mathrm{tot}(\lambda)/2\right], \\ \sin^2\left[\Delta\phi_\mathrm{tot}(\lambda)/2\right]. \end{cases} \tag{16}$$

As the design was performed for $\lambda = 1500$ nm, the mode will be transmitted without cross-talk in the cross arm at that wavelength, for both choices of S_0, whereas the cross-talk increases with increasing shift of wavelength [Fig. 9]. Due to

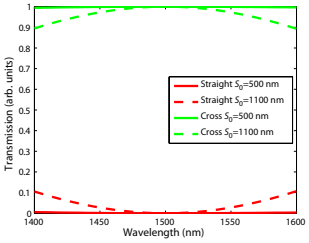

Fig. 9. (Color online) EIM calculated transmission in the straight and cross arm respectively of a waveguide crossing designed for crossing two waveguides at $\lambda = 1500$ nm, with incident signal in the straight arm only. The transmission is plotted for two different S_0 values. For $S_0 = 500$ nm the maximum cross-talk is $= -22.3$ dB, and for $S_0 = 1100$ nm the maximum cross-talk is $= -9.29$ dB, both at $\lambda = 1400$ nm.

the very low dispersion in L_p with wavelength at $S_0 = 500$ nm (see Fig. 8), the cross-talk is very low in this design, reaching a maximum at $\lambda = 1400$ nm of $= -22.3$ dB, indicating very good performance of the device. In contrast the $S_0 = 1100$ nm design has much higher cross-talk, reaching a maximum of $= -9.29$ dB at $\lambda = 1400$ nm, illustrating the importance of keeping the separation as small as possible for this type of device. This design example shows that the realization of low cross-talk and short (less than half of the mode propagation length) waveguide crossings is possible by careful choice of waveguide separation and length of parallel section.

V. Conclusions

Compact directional couplers based on dielectric-loaded plasmonic waveguides has been analyzed using the EIM, and the dependencies on wavelength, in- and out-coupling S-bends, waveguide separation, and length of interaction region has been established in the telecommunication range. The validity of the EIM in the analysis of DLSPPW based DCs has been verified by comparison with near-field optical images of fabricated DCs, obtained by application of a SNOM. A very good correspondence between obtained near-field images and EIM simulated results has been found, and the near-field images furthermore exemplifies the need for careful design of DCs in order to achieve, e.g., wavelength selection. Utilizing the EIM a design approach for realizing wavelength selective plasmonic components, where physical separation of two signals with different wavelengths has been achieved by means of a DC. Based on the DLSPPW technology a wavelength selective DC separating the wavelengths $\lambda = 1400$ nm and $\lambda = 1600$ nm has been designed. With a center-to-center waveguide separation of $S_0 = 819$ nm, total device length of $L_\mathrm{d} = 52.3$ μm (comparable to the DLSPPW mode propagation length) and very low cross-talk, this is a rather compact and practical wavelength selective component. Using a similar approach the design of a low cross-talk waveguide crossing has been demonstrated, and it has been found that by keeping the waveguide separation in the interaction region small, short and close to wavelength invariant crossings can be realized. A design example shows that a crossing of two DLSPPW channels with signals covering a 200 nm large wavelength band can be realized with a maximum cross-talk of -22.3 dB, and a total device length of 20.2 μm. These results show that a diversity of applications are offered by plasmonic components based on DCs, thus confirming it to be a very promising research area.

Acknowledgment

The authors thank Thomas Søndergaard for help in developing a multilayer waveguide program used in this work.

References

[1] V. M. Agranovich and D. L. Mills, *Surface Polaritons - Electromagnetic Waves at Surfaces and Interfaces*, 1st ed. North-Holland Publishing Group, Amsterdam, 1982.

[2] H. Raether, *Surface Plasmons on Smooth and Rough Surfaces and on Gratings*, 1st ed. Springer-Verlag, Berlin, 1988.

[3] W. L. Barnes, A. Dereux, and T. W. Ebbesen, "Surface plasmon subwavelength optics," *Nature (London)*, vol. 424, pp. 824–830, 2003.

[4] I. V. Novikov and A. A. Maradudin, "Channel polaritons," *Phys. Rev. B*, vol. 66, p. 035403, 2002.

[5] S. I. Bozhevolnyi, V. S. Volkov, E. Devaux, J.-Y. Laluet, and T. W. Ebbesen, "Channel plasmon subwavelength waveguide components including interferometers and ring resonators," *Nature (London)*, vol. 440, pp. 508–511, 2006.

[6] S. H. Chang, T. C. Chiu, and C.-Y. Tai, "Propagation characteristics of the supermode based on two coupled semi-infinite rib plasmonic waveguides," *Opt. Express*, vol. 15, pp. 1755–1761, 2007.

[7] P. Berini, "Plasmon-polariton waves guided by thin lossy metal films of finite width: Bound modes of symmetric structures," *Phys. Rev. B*, vol. 61, p. 10484, 2000.

[8] T. Nikolajsen, K. Leosson, I. Salakhutdinov, and S. I. Bozhevolnyi, "Polymer-based surface-plasmon-polariton stripe waveguides at telecommunication wavelengths," *Appl. Phys. Lett.*, vol. 82, pp. 668–670, 2003.

[9] M. Quinten, A. Leitner, J. R. Krenn, and F. R. Aussenegg, "Electromagnetic energy transport via linear chains of silver nanoparticles," *Opt. Lett.*, vol. 23, p. 1331, 1998.

[10] S. A. Maier, P. G. Kik, H. A. Atwater, S. Meltzer, E. Harel, B. E. Koel, and A. A. G. Requicha, "Local detection of electromagnetic energy transport below the diffraction limit in metal nanoparticle plasmon waveguides," *Nat. Mat.*, vol. 2, pp. 229–232, 2003.

[11] T. Nikolajsen, K. Leosson, and S. I. Bozhevolnyi, "Surface plasmon polariton based modulators and switches operating at telecom wavelengths," *Appl. Phys. Lett.*, vol. 85, pp. 5833–5835, 2004.

[12] L. Liu, Z. Han, and S. He, "Novel surface plasmon waveguide for high integration," *Opt. Express*, vol. 13, pp. 6645–6650, 2005.

[13] A. Boltasseva, T. Nikolajsen, K. Leosson, K. Kjaer, M. S. Larsen, and S. I. Bozhevolnyi, "Integrated optical components utilizing long-range surface plasmon polaritons," *J. Lightwave Technol.*, vol. 23, p. 413, 2005.

[14] F. Liu, Y. Rao, Y. Huang, W. Zhang, and J. Peng, "Vertical coupling of long-range surface plasmon polaritons," *Appl. Phys. Lett.*, vol. 88, p. 011110, 2006.

[15] R. Charbonneau, C. Scales, I. Breukelaar, S. Fafard, N. Lahoud, G. Mattiussi, and P. Berini, "Passive integrated optics elements based on long-range surface plasmon polaritons," *J. Lightwave Technol.*, vol. 24, pp. 477–494, 2006.

[16] F. Liu, Y. Rao, Y. Huang, W. Zhang, and J. Peng, "Coupling between long range surface plasmon polariton mode and dielectric waveguide mode," *Appl. Phys. Lett.*, vol. 90, p. 141101, 2007.

[17] G. Veronis and S. Fan, "Crosstalk between three-dimensional plasmonic slot waveguides," *Opt. Express*, vol. 16, pp. 2129–2140, 2008.

[18] D. K. Gramotnev, K. C. Vernon, and D. F. P. Pile, "Directional coupler using gap plasmon waveguides," *Appl. Phys. B*, vol. 93, pp. 99–106, 2008.

[19] A. Degiron, S.-Y. Cho, T. Tyler, N. M. Jokerst, and D. R. Smith, "Directional coupling between dielectric and long-range plasmon waveguides," *New J. Phys.*, vol. 11, p. 015002, 2009.

[20] C. Reinhardt, S. Passinger, B. N. Chichkov, C. Marquart, I. P. Radko, and S. I. Bozhevolnyi, "Laser-fabricated dielectric optical components for surface plasmon polaritons," *Opt. Lett.*, vol. 31, pp. 1307–1309, 2006.

[21] B. Steinberger, A. Hohenau, H. Ditlbacher, A. L. Stepanov, A. Drezet, F. R. Aussenegg, A. Leitner, and J. R. Krenn, "Dielectric stripes on gold as surface plasmon waveguides," *Appl. Phys. Lett.*, vol. 88, p. 094104, 2006.

[22] T. Holmgaard and S. I. Bozhevolnyi, "Theoretical analysis of dielectric-loaded surface plasmon-polariton waveguides," *Phys. Rev. B*, vol. 75, p. 245405, 2007.

[23] A. V. Krasavin and A. V. Zayats, "Passive photonic elements based on dielectric-loaded surface plasmon polariton waveguides," *Appl. Phys. Lett.*, vol. 90, p. 211101, 2007.

[24] S. Massenot, J. Grandidier, A. Bouhelier, G. C. des Francs, L. Markey, J.-C. Weeber, A. Dereux, J. Renger, M. U. Gonzàlez, and R. Quidant, "Polymer-metal waveguides characterization by fourier plane leakage radiation microscopy," *Appl. Phys. Lett.*, vol. 91, p. 243102, 2007.

[25] A. V. Krasavin and A. V. Zayats, "Three-dimensional numerical modeling of photonic integration with dielectric-loaded spp waveguides," *Phys. Rev. B*, vol. 78, p. 045425, 2008.

[26] T. Holmgaard, S. I. Bozhevolnyi, L. Markey, and A. Dereux, "Dielectric-loaded surface plasmon-polariton waveguides at telecommunication wavelengths: Excitation and characterization," *Appl. Phys. Lett.*, vol. 92, p. 011124, 2008.

[27] T. Holmgaard, S. I. Bozhevolnyi, L. Markey, A. Dereux, A. V. Krasavin, P. Bolger, and A. V. Zayats, "Efficient excitation of dielectric-loaded surface plasmon-polariton waveguide modes at telecommunication wavelengths," *Phys. Rev. B*, vol. 78, p. 165431, 2008.

[28] T. Holmgaard, Z. Chen, S. I. Bozhevolnyi, L. Markey, A. Dereux, A. V. Krasavin, and A. V. Zayats, "Bend- and splitting loss of dielectric-loaded surface plasmon-polariton waveguides," *Opt. Express*, vol. 16, pp. 13 585–13 592, 2008.

[29] T. Holmgaard, Z. Chen, S. I. Bozhevolnyi, L. Markey, A. Dereux, A. V. Krasavin, and A. V. Zayats, "Wavelength selection by dielectric-loaded plasmonic components," *Appl. Phys. Lett.*, vol. 94, p. 051111, 2009.

[30] T. Holmgaard, Z. Chen, S. I. Bozhevolnyi, L. Markey, and A. Dereux, "Dielectric-loaded plasmonic waveguide-ring resonators," *Opt. Express*, vol. 17, pp. 2968–2975, 2009.

[31] B. Steinberger, A. Hohenau, H. Ditlbacher, F. R. Aussenegg, A. Leitner, and J. R. Krenn, "Dielectric stripes on gold as surface plasmon waveguides: Bends and directional couplers," *Appl. Phys. Lett.*, vol. 91, p. 081111, 2007.

[32] Z. Chen, T. Holmgaard, S. I. Bozhevolnyi, A. V. Krasavin, A. V. Zayats, L. Markey, and A. Dereux, "Wavelength-selective directional coupling with dielectric-loaded plasmonic waveguides," *Opt. Lett.*, vol. 34, pp. 310–312, 2009.

[33] A. B. Buckman, *Guided-Wave Photonics*, 1st ed. Saunders College Publishing, 1992.

[34] E. D. Palik, *Handbook of Optical Constants of Solids*, 1st ed. Academic, New York, 1985.

Tobias Holmgaard received the B.Sc. in electrical engineering, control engineering degree from the Department of Electronic Systems and the M.Sc. in engineering, applied physics degree from the Department of Physics and Nanotechnology at Aalborg University, Denmark, in 2004 and 2006, respectively. The masters project concerned modeling of plasmonic waveguides and was entitled "Plasmon polaritons in metallic waveguides". Since 2006 he has been working as a Ph.D. student at the Department of Physics and Nanotechnology at Aalborg University, where he is working with near-field characterization and theoretical modeling of surface plasmon polariton waveguides. The PhD project is part of the specific targeted research project "Polymer-based nanoplasmonic components and devices".

Zhuo Chen received the M.Sc. degree in materials physics from Nanjing University, Nanjing, P. R. China, in 2003, and the Ph. D. degree in electromagnetic materials from University of Exeter, Exeter, UK, in 2008. He is currently an associate professor at the Department of Physics and National Laboratory of Solid State Microstructures, Nanjing University after working as a Postdoctoral Fellow at the Department of Physics and Nanotechnology, University of Aalborg, Denmark. His research focuses on surface plasmon polaritons, nano-optics, and photonic bandgap materials.

Sergey I. Bozhevolnyi received the M.Sc. degree in physics and the Ph.D. degree in quantum electronics from the Moscow Institute of Physics and Technology (Russia) in 1978 and 1981, respectively, and the Dr.Sc. degree from Århus University (Denmark) in 1998. From 1981 to 1990, he was an Associate Professor with the Yaroslavl Technical University (Russia). In 1991, he started research on near-field optics at the Institute of Physics, Aalborg University (Denmark), where he has been a Professor since 2003. In 2001-2004, he was the CTO of Micro Managed Photons A/S set up to commercialize the photonic technology utilizing long-range surface plasmon polaritons. His research interests include linear and nonlinear nano-optics, surface plasmon polaritons and nano-plasmonic circuits, multiple light scattering, including photonic band gap and light localization phenomena, and integrated and fiber optics. Since 2008, he is a Professor at the Institute of Sensors, Signals and Electrotechnics (SENSE), University of Southern Denmark.

Laurent Markey received the M.Sc. degree in Chemical engineering and Physical engineering from the Graduate School of Chemistry and Physics of Bordeaux, France in 1994 and the Ph.D degree in Materials Science from University of Lille, France in 1998 where he worked at the Institute of Electronics, Microelectronics and Nanotechnology. In 1999-2001, he was a post-doctoral research fellow in the Polymer Research Centre of the University of Surrey, Guildford, UK. He then worked for the semiconductor company STMicroelectronics, Crolles, France, until 2002 as advanced lithography engineer. He is currently working as a research engineer by CNRS at the University of Burgundy in Dijon, France, specializing in developing nanofabrication and microfabrication processes for various applications and participating in different research projects in the fields of nanophotonics, plasmonics and nanosensors.

Alain Dereux received the PhD in Physics (1991) from the University of Namur (Belgium), was post-doc researcher at the IBM Zrich Research Laboratory (1992). In 1995, he was appointed Professor of Physics at the University of Burgundy (Dijon, France) where he was promoted Full Professor in 2003. From 2004 to 2008, he was coordinator of the FP6 IST Network of Excellence "Plasmo-Nano-Devices" devoted to surface plasmon photonics. In 2007, he organised the 3d International Conference on Surface Plasmon Photonics. His research activities, covering near-field optics and plasmonics, aim at controlling optical processes at the sub-wavelength scale.